10-30-2003

Small And Large Signal Modeling Of MM-Wave MHEMT Devices

William, Clausen
University of South Florida

Small And Large Signal Modeling Of MM-Wave MHEMT Devices

by

William Clausen

A thesis submitted in partial fulfillment
of the requirements for the degree of
Master of Science in Electrical Engineering
Department of Electrical Engineering
College of Engineering
University of South Florida

Co-Major Professor: Lawrence P. Dunleavy , Ph.D.
Co-Major Professor: Rudolf Henning, Ph.D.
Tom Weller, Ph.D.

Date of Approval:
October 30, 2003

Keywords: transistor, hemt, noise, nonlinear, GaAs

TABLE OF CONTENTS

LIST OF TABLES

LIST OF FIGURES

Small and Large Signal Modeling of MM-Wave mHEMT Devices

William Clausen

ABSTRACT

This research effort advances millimeter-wave transistor modeling in a current RF/Microwave circuit simulator (Agilent's Advanced Design System-ADS) for small-signal noise and large signal simulations. The device modeled is a metamorphic High Electron Mobility Transistor (mHEMT) supplied by Raytheon RF components. Because of their structure, these new low noise devices are used in this work to test the abilities to accurately model in the sub 0.5dB noise figure territory and to study model prediction into W-band (75-110 GHz).

New modeling issues discussed in this thesis involve the effects of noise modeling in relation to the small-signal model parameters. The noise modeling identifies two methods of extraction and how to determine good noise data. Other modeling topics addressed are the use of an advanced nonlinear model, and the ability to optimize for gain compression in the nonlinear model.

Several measurement systems were used in the extraction and validation of this modeling effort. They consist of the ATN NP5 noise system, Maury Automated Tuner System, Agilent's IC-CAP, and Gateway's Special. The concept behind using these systems was to construct a complete modeling reference for a transistor and validate it against noise parameter and nonlinear measured data. Since the modeling work for this

thesis is built on previous work, one goal has been to bring past USF field-effect transistor (FET) modeling efforts up to date and refine them for future use.

The noise measurements were compared to results from Raytheon to validate the USF ATN noise parameter measurement system. Also the IC-CAP modeling system has been validated in measuring the test devices using the Maury load-pull system. Small-signal and noise modeling were accomplished using techniques standardized from several technical papers and prior USF Ph.D. work relative to the model extraction. The IC-CAP modeling software also provided a straightforward platform for large-signal model extraction that is documented in this thesis. Using optimization in ADS, a final nonlinear was created.

Measured DC, S-parameter, noise parameters, harmonic power, TOI, load-pull, and efficiency measurements were shown to compare well with model data simulated in ADS. Temperature scaling was also executed using a linear approximation of model values over measured temperatures in the noise model. The results presented show that the models developed illustrate good fitting of the behavior of the mHEMT device.

CHAPTER 1

INTRODUCTION

In recent years computing power and memory have been growing at a substantial rate and the ability to simulate a transistor or other non-linear device is becoming easier and more economical for companies than to invest in expensive test equipment for designing microwave circuits. Required microwave measurement equipment can be extremely expensive for experimentally matching a device for optimum noise or power, measure s-parameters, perform load-pull test and perform a databased design. With adequate computer models, engineers can design microwave circuits with minimal equipment cost given that the models are reliable. This is becoming more common with the growth of fabless design facilities. With an initial investment in the required software and computer hardware, a company can design and sell Monolithic Microwave Integrated Circuits, (MMICs), for much less overhead. As stated before, the reliability of the model is the key to how well one can design a circuit for a specified operating goal.

It is the objective of this effort to obtain two models for a 6x12.5 um metamorphic High Electron Mobility Transistor, (mHEMT), supplied by Raytheon RF Components [1]. The first model will be a small-signal noise model that is bias and temperature dependent. The USF table model [2], which is a user-defined model in Libra (a pre-cursor to ADS), was originally planned to be translated to Agilent Technologies Advanced Design System (ADS) version 1.5 [3]. This model was created by Pete Winson

and Steve Lardizabal as part of their PhD dissertations [4,5]. The USF table model was to provide the background for this work. Since the scope of this work was to study noise and large-signal modeling, time spent for encoding a new model was secondary in purpose. Direct translation of the model to ADS was not feasible due to changes in the design of the RF simulation software. The table model could be reconstructed in ADS by a proficient C+ programmer with guidance from a knowledgeable modeling engineer, however, a somewhat different approach was implemented.

Instead, a solution was created based on entering the table model parameters into ADS design templates using pre-existing data accessing and component labeling available in ADS. This method allows the user to set up a table that can be based on both drain current and drain voltage. By setting up a key, the user can enter in the intended bias condition and the simulator will look up those values in the corresponding list. Equations used in variable blocks in the design schematic allow for interpolation between selected data in the table.

The second model will be a large-signal HEMT model developed using IC-CAP 5.3 modeling software from Agilent. This software package contains a model specific for HEMT devices that can be easily translated to ADS for simulation. This particular model was chosen because of its ability to match measured data by a pragmatic analytical procedure using several concepts from previous nonlinear modeling efforts that include Statz, Curtice, Canfield, and Golio [6,7,8,9]. It includes features such as self-heating correction, dispersion characteristics, extrapolation outside measurement range, and a drain current model that adapts to many different processes.

Since previous USF work has outlined the modeling process for FET devices [4,5], the modeling approach for mHEMT devices will be similar except that several challenges, discovered during the course of this work, will be addressed. These issues came in the form of calibration problems above 40 GHz, low-noise modeling, noise measurement tolerances, effects of equivalent circuit parameters (ECPs) on the noise extraction, and low voltage breakdown. Extractions of the model parameters were derived from measurement data taken from the ATN NP5 noise parameter measurement system and the UNIX based IC-CAP program. The model will be verified with measurements on the ATN NP5 noise measurement system [10] and the Maury Microwave load-pull system [11] at USF.

1.1 Thesis Contributions and Methods

For the small-signal noise model, a main requirement was to achieve good agreement up to mm-wave frequencies for both S-parameter data and noise parameter data. Accurate modeling of the frequency dependent parameters were necessary for extrapolating to frequency ranges up to 110 GHz. The number of biases used for this modeling effort was also larger than previous efforts accounting for a broad range of available parameters from near pinch-off to ½ Idss. The drain-to-source voltage range extended from the knee to the region just before breakdown.

Noise measurements were made on two different systems to account for measurement errors for low noise figure data. Where previous temperature dependent modeling included ranges above room temperature, the temperature dependence of this model ranges from –55^{o}C to 85^{o}C. Because of the result the low noise figure performance had on modeling the mHEMT at –55^{o}C, a separate study was later conducted on the

consequence of the small-signal parameters on the noise modeling in regards to setting the gate noise coefficients to ambient temperature.

The nonlinear modeling effort involved using the Agilent EEHEMT, which yielded features that, allowed improved fitting of the voltage dependent capacitances and accurate IV fitting. Model development required a more rigorous extraction than previous nonlinear models because of the complexity of fitting elements available in the model. Because of the multifaceted approach to the drain current equations and capacitance functions, the EEHEMT model provides better prediction of nonlinear elements along the entire IV plane. Since the model is derived from many sets of data taken over the IV plane, the S-parameter fitting, likewise, is improved over the complete range of biases.

Using Agilent's IC-CAP, the extraction procedures were well defined and required the user to simply enter test conditions for the measurements. Although the system allows an easier approach to HEMT modeling, the user still needs to be proficient in modeling techniques and have some knowledge of the device under test. Utilizing the new Maury load-pull system at the University of South Florida, the developed EEHEMT model for the Raytheon mHEMT was measured for maximum output power, gain, and efficiency at several output impedances. The optimum gammas were then compared to the extracted nonlinear model for validation. Along with single tone power measurements, two-tone intermodulation distortion measurements were completed. This thesis will be the first USF project using fully automated modeling and measurements systems for nonlinear model generation.

1.2 Device Technology

Since every increase of signal strength can be utilized for conserving power or limiting the size of the antenna, low noise amplifiers (LNAs) enable smaller transmit and receive modules that require much less power. In space applications, this can affect the amount of battery storage a satellite may need or reduce the size of the receive dish. This in turn reduces the weight of the payload and helps reduce the cost of sending satellites into orbit. New transistor technologies have contributed to a reduction of cell phone size and an increase in roaming distance. Because of their low power consumption, the new generation of cell phones can operate for many hours on a single charge with a battery ten times smaller than ones ten years ago.

Another consideration for this new design is the need for bandwidth in today's market. As demand grows for communication transfer at rates of Gb/s, the industry must progress to higher frequencies. These higher frequencies demand that the materials of transistors have enough electron velocity to meet required specifications. Silicon (Si), which comprises most of the low frequency market, does not generally possess the unity current gain frequency (f_t) to have reasonable gain or noise performance in the millimeter-wave range. Gallium Arsinide (GaAs) has been the material of choice for high frequency applications because of its superior performance to Si, but unfortunately the cost is also greater. Another material that has expanded millimeter-wave (above 30 GHz) capability further is the doping of GaAs with Indium (In) in the conducting channel of the device. The mobility of a GaInAs channel with In content above 40% can be as great as 12,000 cm^2/Vs as compared to 6,000 for GaAs and 1450 for Si [12]. The greater

mobility of the electrons in these advanced materials allow device operation up to 300 GHz.

In the early 1980's, the design of modulation doped FETs ,usually referred to as HEMTs, resulted from the progress of manufacturing in process techniques and electron beam lithography. A good review of HEMT technology can be found in [13]. HEMT theory involves moving electrons from a high bandgap material to a low bandgap material and trapping the electrons in the heterojunction formed between the materials. This trap forms a quantum well that gives rise to a two dimensional gas or 2DEG. The electron current is passed through this 2DEG with significantly reduced ionization scattering. From this design, the HEMT usually has much higher electron mobility and saturation velocity than conventional GaAs MESFET devices.

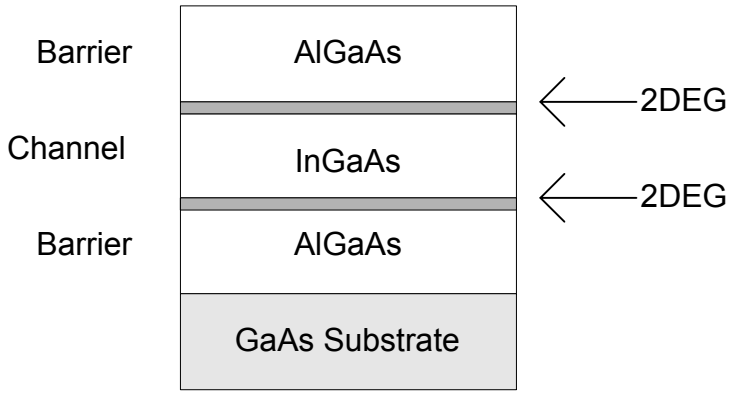

Figure 1.1 GaAs PHEMT Material Structure.

Popular HEMT devices today include use psuedomorphic HEMTs and InP HEMTs. An illustration of a pHEMT is shown in Figure 1.1. With the introduction of In in the GaAs channel, greater high frequency performance can be obtained. The barrier layer of a PHEMT consists of AlGaAs and the channel is InGaAs. In this structure the

electrons move from the AlGaAs to the InGaAs instead of GaAs as in standard HEMTs. The pHEMT can contain a concentration of up to 25% Indium in the channel. Indium Phosphite (InP) HEMTs, however, can have greater concentrations of Indium in the channel due to its lattice match with the InP substrate. The barrier material is InAlAs, compared to AlGaAs in pHEMTs, and can match well with InP. The higher cost of these InP devices (typically made on 2-3" wafers) limits their use to space-based or military applications. As engineers have examined this cost issue, a design goal was to have the cost and manufacturability of 6 inch GaAs substrates with the performance of high Indium content channels. The result was the metamorphic HEMT.

The mHEMT uses a lattice-changing graded buffer layer [14] that helps match the InAlAs barrier material to the GaAs substrate. This helps to reduce the strain-induced imperfections between the two materials. As illustrated in the article by Whelen et Al. [14], the performance of these transistors rival current InP HEMTs in gain, noise, efficiency, and mobility. A comparison between the channel material structures of an InP HEMT and a MHEMT is shown in Figure 1.2.

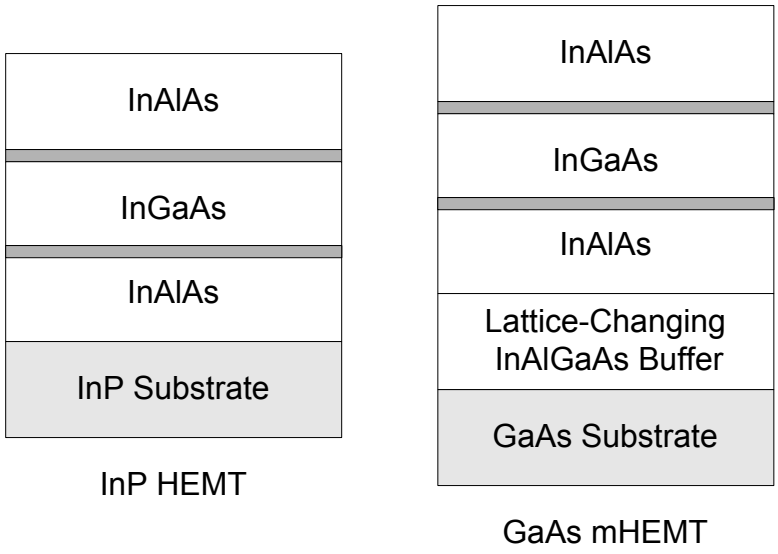

Figure 1.2 Comparison of InP HEMT Material Structure to the GaAs MHEMT Structure [14].

The gate in a FET transistor is usually the most influential geometrical feature on the noise performance and the limiting factor for the frequency of operation. The gate length of the devices under test are 0.15 um which requires electron-beam epitaxy to form the gate fingers. The device supplied by Raytheon for this work is a 75 um gate width mHEMT designed for low noise applications, high gain, and high efficiency. The channel content is 60% In and 40% GaAs and the periphery is 6 x12.5 um. For transistors, the gate width is the deciding factor for the output power and gain of the transistor. Since this is only a 75 um gate width device and typical power dissipation is 250 mW/mm a maximum DC power of 18.75 mW can be expected. This relates to a current of 18.75 mA at a drain voltage of 1 volt or 12.5 mA at 1.5 volts. These current values will be used as the constraints placed on the initial testing for the DC-IV data in the nonlinear model. The device used in this thesis is displayed in Figure 1.3. The gate is on the right and the drain is on the left. The source is identified by the large square region above the transistor that contains a via to the ground plane of the substrate.

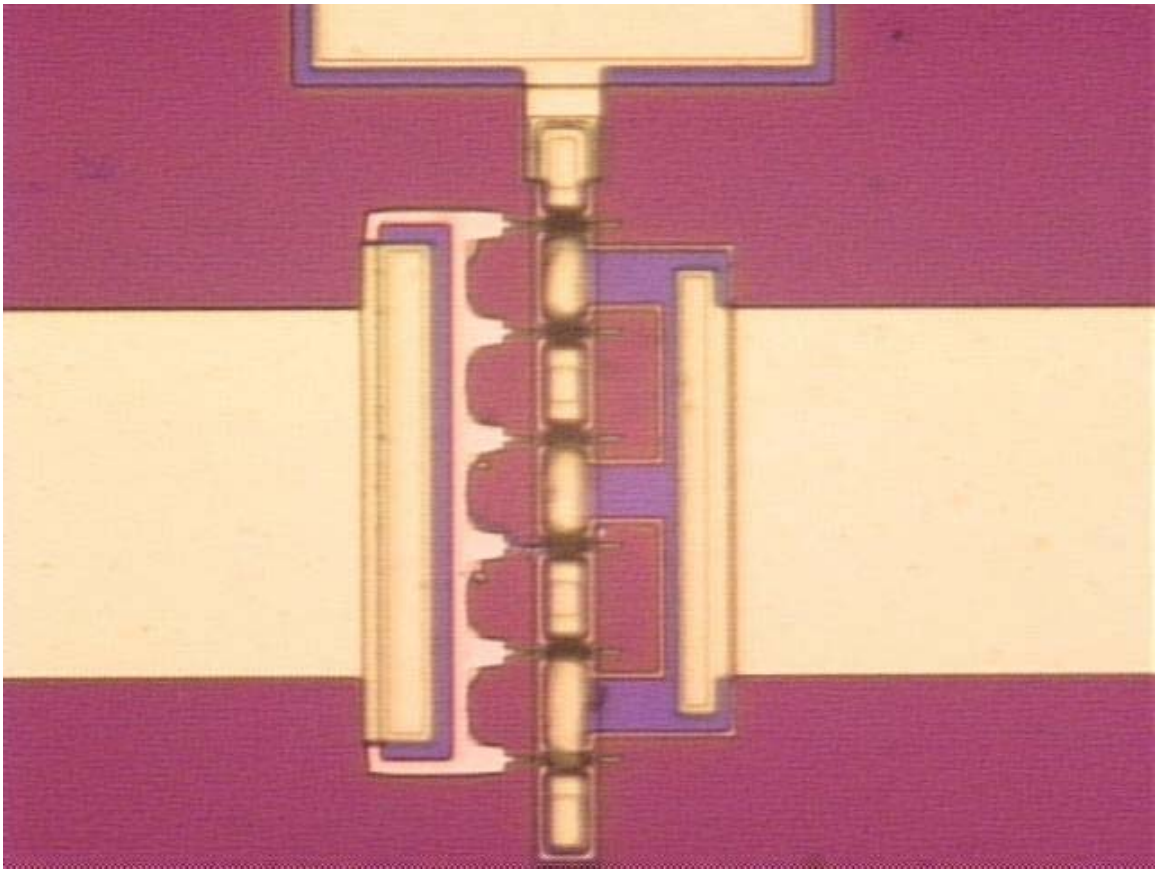

Figure 1.3 Photograph of Raytheon 6x12.5um mHEMT.

1.3 Chapter Summary and Thesis

The work outlined in this thesis demonstrates the contemporary approach of modeling devices and their ability to replicate the characteristics of the mHEMT using selected model topologies and formats. Chapter 2 lays the groundwork for the noise model and comprises the theory behind the small signal model, its parameters, and the two- port noise model incorporated in the small-signal model.

Chapter 3 contains a brief summary of the different nonlinear models available precedes the details of the large-signal model using IC-CAP. The differences in the current and charge equations as compared to other models is shown with added features of the dispersion current, gate forward conduction, and self-heating thermal model. All

the model parameters are defined and the corresponding equations that characterize the DUT are presented for the reader to follow.

Chapter 4 illustrates the measurement procedures and equipment involved to gather the data needed. The software employed in this effort is presented and includes measurement and extraction routines with general considerations and changes made due to inabilities with current solutions. In Chapter 5, the outcome of the modeling effort is exhibited. Plots of s-parameter and noise parameter fitting show the results for the small signal noise model, and DC, gain, compression, efficiency, and load-pull comparisons are made for the nonlinear model. Chapter 6 incorporates the conclusions of this effort with recommendations presented for future work in this area.

CHAPTER 2

SMALL SIGNAL AND NOISE MODELING

2.1 Introduction

One of the primary goals of this work is to provide a temperature and bias dependent noise equivalent circuit model in Agilent Technologies ADS [3]. The USF table-based model, developed by former PhD graduates Pete Winson and Steve Lardizabal, was used as the basis for this effort [2,4,5]. The model consists of a user-defined C program operated in Libra 6.0 that interpolates drain current and drain voltage. The model's input file consists of linear temperature coefficients for equivalent circuit parameters at each measured bias point. Another program named Textract [15] is used to create equivalent circuit parameter (ECP) slopes for temperature dependent data. The Textract program was created by Pete Winson for small-signal equivalent circuit parameters ,ECPs, versus temperature, and later altered by Steve Lardizabal and Mark Weatherspoon for noise. Using a slope equation, the user defines the ambient temperature at which the device is operated and the program starts at an initial value and calculates the ECPs for that particular bias. Noise generators were later added in the form of equivalent gate and drain thermal noise temperatures T_g and T_d into the table. The same interpolation was used for these components as mentioned before.

Initially, this project involved an attempt to translate the USF table model into ADS and create a custom input file for the model to represent the MHEMT devices. Because of translation problems and the fact that the scope of this work was not to only

create a new user defined table model, existing ADS equation tools were used to create a fully functional alternative approach to the table model. The underlying methods behind the setup will be illustrated in this chapter. The measurement methods used are explained in detail in Chapter 4.

2.2 Initial Measurement Data

The program used for the small signal modeling is a product from Gateway Modeling, Inc., called SPECIAL [16]. This program uses direct extraction techniques for determining ECPs from a set of S-parameters in an easy to use format. The extractor determines a unique set of ECPs at each frequency and then averages them so that the final values are frequency independent [17]. Three sets of S-parameters are required for model extraction. The first two sets require a zero drain voltage for MESFETs or HEMTs and the gate voltage is in forward conduction (cold FET) or pinched off (pinched FET). The pinched FET data is used to determine the parasitic capacitance or pad capacitance. The cold FET data is used to extract the extrinsic parameters that include the gate, source, and drain resistance and inductance. The hot FET data, which implies that the drain voltage is non-zero, is used to extract the intrinsic components. The direct extraction of extrinsic and intrinsic FET parameters from cold FET and hot FET bias conditions follows methods that have been reported in the literature [18,19].

Noise parameters and S-parameters were measured from 2 to 26 GHz using the ATN NP5B noise parameter and S-parameter measurement system software [10] and related instrumentation available at USF. Both S-parameters and noise parameters are taken at every bias and placed into a S2P file format. The S2P file format can be seen in Appendix F.

To have better model prediction at higher frequencies, S-parameter measurements were also performed up to 50 GHz. This data is used for the small signal model development and verification while the ATN data would be solely used for noise extraction. For this project, the biases include .5, .75, 1.0, and 1.25 V_{ds} and 1-12 mA for I_{ds}. The variable bias range enables the determination of the actual bias for optimum low noise or gain performance to equip a designer with the ability to meet a specified performance trade-off. As another note, large signal modeling requires measured S-parameters throughout a wide range of biases across the DC-IV measurement plane.

2.3 Small Signal Modeling Theory

The method used for extracting the small signal parameters is well established and has been in use with great success for some time. Dambrine et. al.and beroth bosch [20,19]. In Figure 2.1 the representation of the basic small signal circuit is shown. The premise is to represent the device using Y-parameters. These Y-parameters are for the intrinsic elements with the extrinsic ECP's removed. To begin with, the S-parameters are converted to Y-parameters to allow for the removal of pad capacitances. The Y-parameters are converted to Z-parameters to allow removal of R_g, R_d, R_s, L_g, L_d, and L_s. The final step is to convert back to Y-parameters.

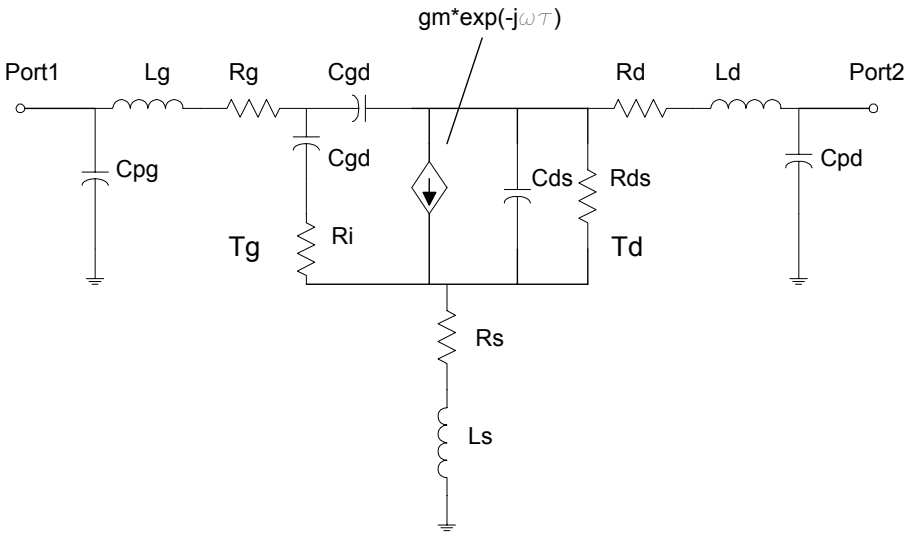

Figure 2.1. Small Signal Equivalent Circuit Model Topology. T_g and T_d are artificial temperatures used for noise modeling.

To measure the pad capacitances, the HEMT is pinched off at V_{ds}=0. This in affect turns the device off or creates an open circuit and the S-parameters are formed from the pad capacitance values. The Smith chart representation should have S_{11} and S_{22} on top of one another and S_{12} and S_{21} should be equal. Figures 2.2 and 2.3 display the measurement of a pinched mHEMT. Literature does suggest that these pad capacitances are often negligible and can be omitted if desired [16,20]. The result if left out, will be that the effects of these pad capacitances will added to C_{gs} and C_{ds}.

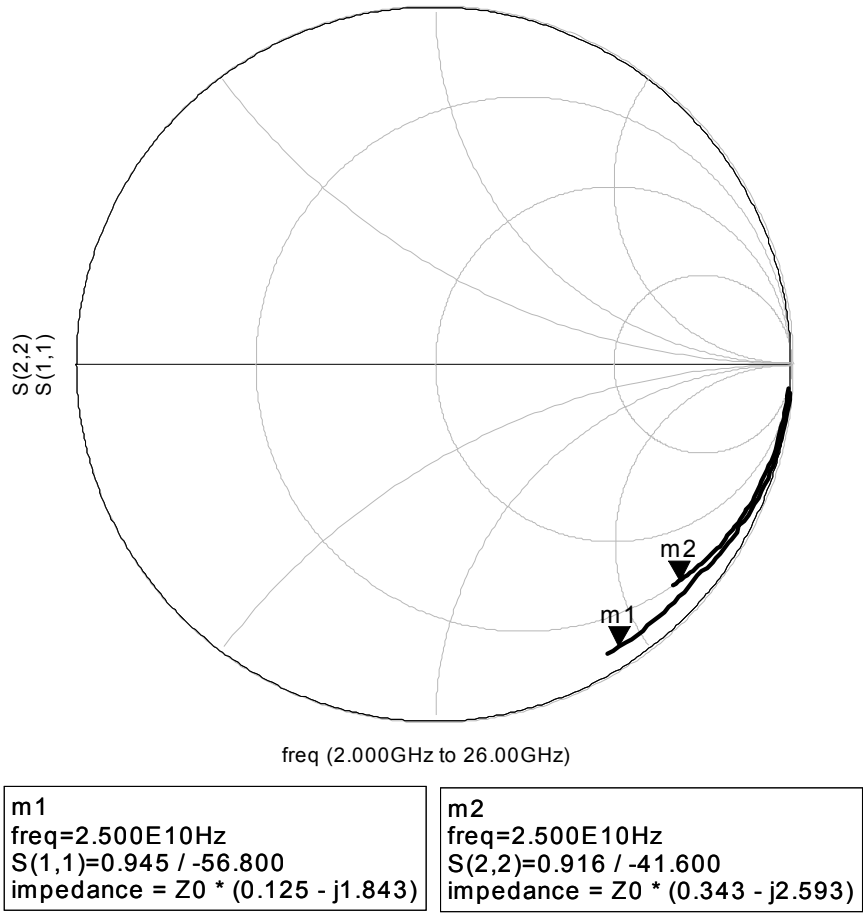

Figure 2.2 Example Pinched FET Measurement of S_{11} and S_{22}. (S_{11}=m1, S_{22}=m2) V_{ds} =0V, V_{gs} =-.9V.

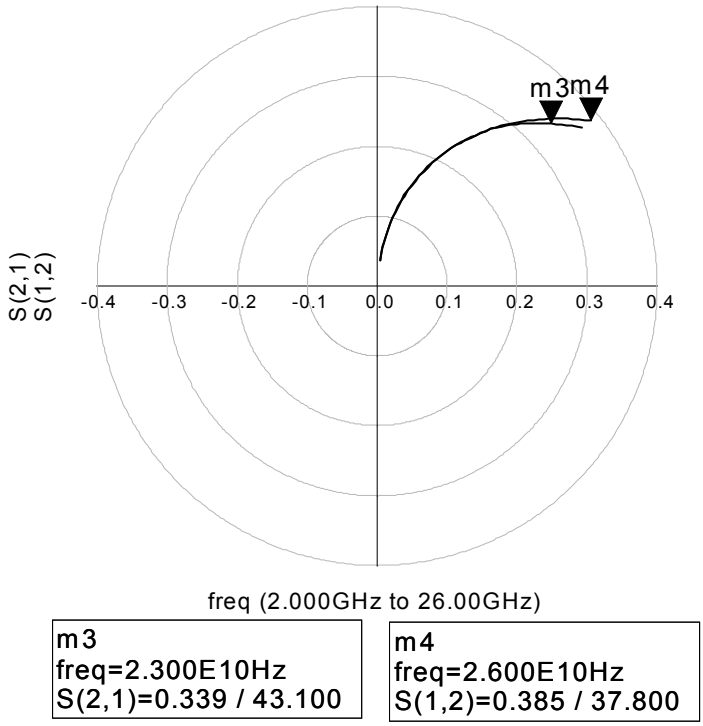

Figure 2.3 Example Pinched FET Measurement of S_{12} and S_{21}. (S_{21}=m3, S_{12}=m4) V_{ds}=0V, V_{gs}=-.9V.

To determine the extrinsic resistance and inductance, the gate diode of the HEMT is placed into forward conduction, with V_{ds}=0. This is known as a Cold FET measurement. In Figure 2.4, S_{11} and S_{22} are both inductive on the upper left quadrant of the Smith chart. For this particular device, the two vias on either side of the HEMT provided a large source inductance in the model. Usually the length of the traces for S_{12} and S_{21} will provide some guidance as to the magnitude of the inductance due to imaginary part of equations (2.1-2.3). The basic concept is that the intrinsic elements approximate a short circuit and the remaining ECP values are determined by Z-parameters converted from the Cold FET S-parameters. This short circuit is due to the gate capacitance term going to zero at a sufficient gate current density. All that is left is

channel resistance, R_{ch}, plus the extrinsic elements. The equations used by SPECIAL to solve for the extrinsic ECPs are given as

$$Z_{11} = R_g + R_s + {R_{ch}}/{3} + {nkT}/{I_g} + j\omega(L_g + L_s) \tag{2.1}$$

$$Z_{12} = Z_{21} = R_s + {R_{ch}}/{2} + j\omega L_s \tag{2.2}$$

$$Z_{22} = R_s + R_d + R_{ch} + j\omega(L_s + L_d) \tag{2.3}$$

Table 2.1 Extrinsic Parameter Definitions.

Parameter	Definition
R_{ch}	Channel Resistance
R_g	Extrinsic Gate Resistance
R_s	Extrinsic Source Resistance
R_d	Extrinsic Drain Resistance
L_g	Extrinsic Gate Inductance
L_s	Extrinsic Source Inductance
L_d	Extrinsic Drain Inductance

For the inductance values, the imaginary part is dependent on frequency. The real part will be dependent on changes in gate voltage. In finding the slope between the real parts of several different forward biased gate voltages, the resistances can be found.

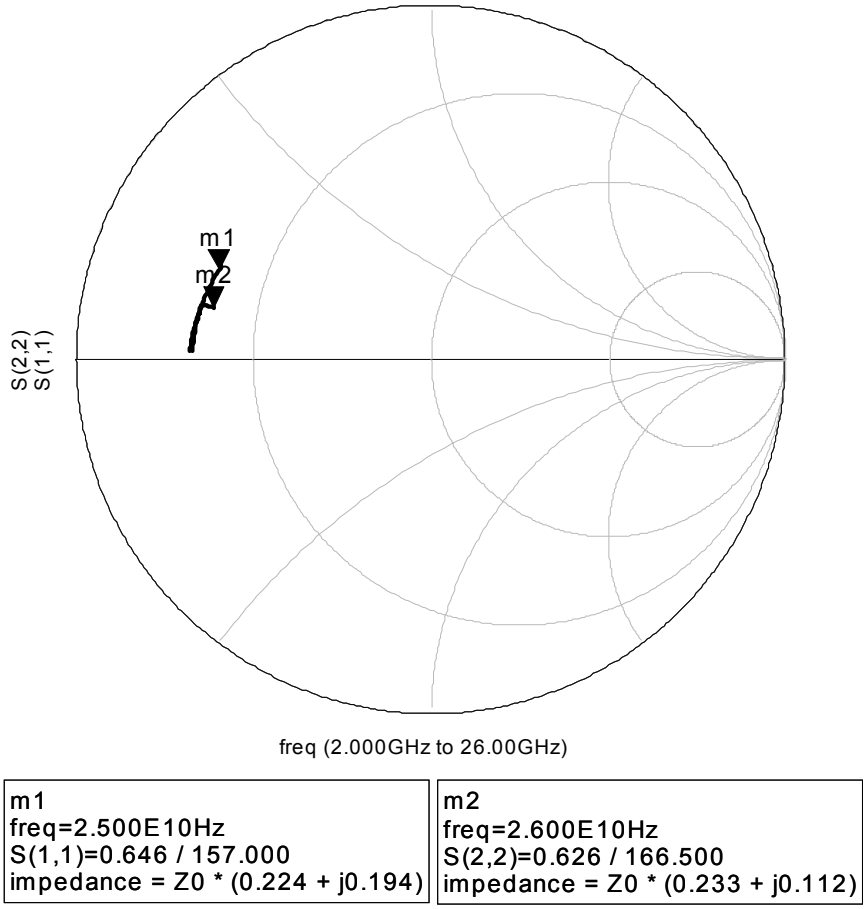

Figure 2.4 Example Cold FET Measurement of S_{11} and S_{22}. (S_{11}=m1, S_{22}=m2). V_{ds}=0V, V_{gs}=.85V.

After removing the extrinsic effects from the Y-parameters, the resulting equations are given for the intrinsic circuit. According to Dambrine, et al. [20], low noise devices characteristically have D=1 at lower frequencies since *Ri* and *Cgs* have small values.

$$Y_{11} = \frac{R_i C_{gs}{}^2 \omega^2}{D} + j\omega\left(\frac{C_{gs}}{D} + C_{gd}\right) \tag{2.4}$$

$$Y_{12} = -j\omega C_{gd} \tag{2.5}$$

$$Y_{21} = \frac{g_m \exp(-j\omega\tau)}{1 + jR_i C_{gs}\omega} - j\omega C_{gd} \tag{2.6}$$

$$Y_{22} = \frac{1}{R_{ds}} + j\omega\left(C_{ds} + C_{gd}\right) \tag{2.7}$$

$$D = 1 + \omega^2 {C_{gs}}^2 {R_i}^2 \tag{2.8}$$

Table 2.2 Intrinsic Parameter Definitions.

Parameter	Definition
C_{gd}	Gate-to-Drain Capacitance
C_{gs}	Gate-to-Source Capacitance
C_{ds}	Drain-to-Source Capacitance
R_i	Gate-to-Source Resistance
g_m	Transconductance
τ	Time Delay
R_{ds}	Drain-to-Source Resistance

The extraction steps are illustrated below as explained by Berroth and Bosch [19]. Using SPECIAL, a set of ECPs can be determined for each frequency measured and averaged for frequency independence

$$C_{gd} = -\frac{\mathrm{Im}\left(Y_{12}\right)}{\omega} \tag{2.9}$$

$$C_{gs} = \frac{\mathrm{Im}\left(Y_{11}\right) - \omega C_{gd}}{\omega}\left(1 + \frac{\left(\mathrm{Re}\left(Y_{11}\right)\right)^2}{\left(\mathrm{Im}\left(Y_{11}\right) - \omega C_{gd}\right)^2}\right) \tag{2.10}$$

$$R_i = \frac{\mathrm{Re}\left(Y_{11}\right)}{\left(\mathrm{Im}\left(Y_{11}\right) - \omega C_{gd}\right)^2 + \left(\mathrm{Re}\left(Y_{11}\right)\right)^2} \tag{2.11}$$

$$g_m = \sqrt{\left(\mathrm{Re}\left(Y_{21}\right)\right)^2 + \left(\mathrm{Im}\left(Y_{21}\right) - \omega C_{gd}\right)^2\left(1 + \omega^2 {C_{gs}}^2 {R_i}^2\right)} \tag{2.12}$$

$$\tau = \frac{1}{\omega}\arcsin\left(\frac{-\omega C_{gd} - \mathrm{Im}\left(Y_{21}\right) - \omega C_{gs} R_i \,\mathrm{Re}\left(Y_{21}\right)}{g_m}\right) \tag{2.13}$$

$$C_{ds} = \frac{\mathrm{Im}\left(Y_{22}\right) - \omega C_{gd}}{\omega} \tag{2.14}$$

$$R_{ds} = {}^{1}\!\Big/\!_{\mathrm{Re}\left(Y_{22}\right)} \tag{2.15}$$

The percentage of error between model and measured S-parameters is typically allowed to three percent. The error is determined between the magnitudes of the real and imaginary parts of the S-parameters for the measured data and model data. The percent error calculation from SPECIAL is shown below and "ReS_{11}" can be substituted for the real or imaginary part of all four s-parameters.

$$Err(\mathrm{Re}\,S_{11}) = \frac{100}{n}\sum_{i=1}^{n}\frac{\left|\mathrm{Re}\,S_{11}\left(\mathrm{meas}\right) - \mathrm{Re}\,S_{11}\left(\mathrm{model}\right)\right|}{\left|S_{11}\left(\mathrm{meas}\right)\right|} \tag{2.16}$$

Since the ability to make a good calibration will affect the accuracy of the extraction results, the 40-50 GHz data was not used because of calibration inconsistencies above 40 GHz in the 50 GHz S-parameter measurements. In using SPECIAL, there was not a problem with getting all fits under the three percent standard with the 40 GHz data sets for all the biases.

2.4 Noise Modeling Theory

Noise modeling can take different forms when placed into the small signal model. All models are composed of a noiseless two-port with noise generators on the input and output [21]. One technique is to use a series voltage and parallel current source on a noiseless two port. The series voltage source is defined as E_n and the parallel current source is defined as I_n. A simple technique outlined by Pospieszalski is to represent R_i and

R_{ds} with certain temperature values that will produce the noise measured for the device [22]. This is based on the fundamental principal that the thermal noise voltage generated by a passive device is given by

$$\left(\left|E_n\right|\right)^2 = 4kR_nT\Delta f \tag{2.17}$$

where k is Bolztman's constant, R_n is the resistance, T is the ambient temperature, and Δf is the bandwidth.

The measurements used for noise modeling in this work include the noise parameters F_{min}, R_n, and Γ_{opt}. F_{min} will give the value of the optimum device noise figure performance at Γ_{opt}. Γ_{opt} is the source reflection coefficient for F_{min} and R_n is the noise resistance. These four parameters plus the Y-parameters of the intrinsic HEMT are used for the modeling process. To test if the noise data is physically real the formula used is [22]

$$1 \le \frac{4R_{opt}g_nT_o}{T_{\min}} \le 2 \tag{2.18}$$

where R_{opt} is the real part of the optimum noise match, g_n is the noise conductance, T_o is ambient temperature, and T_{min} is the minimum noise temperature of the device at the optimum match.

The ATN NP5 noise parameter measurement system outputs a reflection coefficient for Γ_{opt} in the impedance plane of the Smith chart. In order to use the modeling equations, it must be converted to a real and imaginary admittance. This is done easily by using

$$Y_{opt} = \left(Z_0 \cdot \frac{1+\Gamma_{opt}}{1-\Gamma_{opt}} \right)^{-1} \tag{2.19}$$

Figure 2.5 Noiseless Two-Port with Current and Voltage Noise Generators.

The basic representation of a current and voltage noise source in an ABCD matrix is portrayed in Figure 2.5 [23]. To achieve the voltage source E_n and the current source I_n, the parameters F_{min}, R_n, and Y_{opt} must be converted to an arrangement that can best represent Figure 2.5 [24]. Y_c is defined as the correlation admittance between E_n and I_n [24]. It is defined as

$$Y_c = \frac{I_n \cdot \overline{E_n}}{E_n \cdot \overline{E_n}} \tag{2.20}$$

which can be represented by the noise parameters as

$$Y_c = \left[\frac{(nf-1)}{2R_n} \right] - Y_{opt} \tag{2.21}$$

where

$$nf = 10^{\left(\frac{F_{\min}}{10}\right)} \tag{2.22}$$

The term related to the uncorrelated part of

$$I_n - Y_c E_n \tag{2.23}$$

is known as g_n or the noise conductance which is defined by

$$g_n = \frac{\left(\left|I_n - Y_c E_n\right|\right)^2}{4kT\Delta f} \tag{2.24}$$

By using equation 2.21, 2.22, and 2.23, the measured noise parameters can be set up to represent g_n as

$$g_n = \left(nf - 1\right)\left[\mathrm{Re}\left(Y_{opt}\right) - \frac{\left(nf - 1\right)}{4R_n}\right] \tag{2.25}$$

The noise parameter R_n is related to the power of E_n. Also the voltage source E_n is related to I_n and the input impedance of the noiseless network:

$$R_n = \frac{\left|E_n\right|^2}{4kTB} \tag{2.26}$$

$$E_n = \frac{-1}{Y_{11}} I_n \tag{2.27}$$

The final form of E_n and I_n can be expressed as

$$\left|E_n\right|^2 = \frac{4kTB\left[g_n + R_n\left|Y_{11} - Y_c\right|^2\right]}{\left|Y_{11}\right|^2} \tag{2.28}$$

$$\left|I_n\right|^2 = 4kTB\left|\frac{Y_{21}}{Y_{11}}\right|^2\left[g_n + R_n\left|Y_c\right|^2\right] \tag{2.29}$$

The terms Y_{11} and Y_{21} can be determined in two different ways. The first approach involves taking the measured S-parameters and subtracting the values of the extrinsic components. This is accomplished by converting to Z-parameters to subtract inductances

and resistance, then converting to Y-parameters to subtract the capacitances. The network is now converted to the intrinsic Y-parameters shown in equations 2.4-2.7. The second method is to use equations 2.4 and 2.6 to represent the intrinsic parameters from the already developed small signal model ECPs. In the modeling work for this thesis, both methods were used in the extraction template created for ADS. The template for both methods can be viewed in Appendix D.

The inclusion of the nondimensional noise coefficients *P, R*, and *C* comes from the work outlined by A. Van der Ziel [23]. P and R are both aspects of the device geometry and biasing condition while C is defined as the cross correlation between P and R. These coefficients are inserted into equations 2.27 and 2.28 to form

$$\overline{E_n^{\,2}} = 4kTB\frac{R}{g_m} \tag{2.30}$$

$$\overline{I_n^{\,2}} = 4kTBPg_m \tag{2.31}$$

In substituting 2.27 and 2.28 into 2.29 and 2.30, the following expressions are found:

$$R = g_m \frac{\left[g_n + R_n \left| Y_{11} - Y_c \right|^2 \right]}{Y_{11}^{\,2}} \tag{2.32}$$

$$P = \frac{1}{g_m}\left[\left| \frac{Y_{21}}{Y_{11}} \right|^2 \left(g_n + R_n \left| Y_c \right|^2 \right) \right] \tag{2.33}$$

To get the noise generators into a form that is dependent on the frequency and temperature of the circuit, the resistors R_i and R_{ds} in the equivalent circuit model are given a calculated temperature that generates the predicted noise performance of the device. This approach was first suggested by Pospieszalski [22]. Referring back to Eq. 2.16, the noise power is dependent on both bandwidth and ambient temperature. The

values for the temperatures for R_i and R_{ds} are defined as T_g and T_d. T_g is attributed to the temperature of R_i and T_d is associated with R_{ds} (see Figure 2.1). The resulting formulas used are given in 2.34 and 2.35.

$$T_g = R\frac{T_o}{R_i g_m} \tag{2.34}$$

$$T_d = P \cdot T_o g_m R_{ds} \tag{2.35}$$

From the results of the mHEMT modeling, the values for T_g were low. When modeling data taken at –55°C, the value for T_g could be as low as 20°K while T_d could be as high as 5000°K. An alternative approach, implied by Pospieszalski [22] could be to set T_g to ambient temperature. If this is done, the balance of the noise model fitting job would fall upon T_d. To fit the model to T_d by setting T_g to the ambient temperature or 25°C, the equation given for the parameter R_n in Pospieszalski [22] is used for the extraction. Equation 2.36 is set to 2.37 since T_g is equal to the ambient temperature, T_o, and 2.38 is the solution when solving for T_d.

$$R_n = \frac{T_g}{T_o}R_i + \frac{T_d}{T_o g_m{}^2 R_{ds}}\left[1+\left(\omega C_{gs}R_i\right)^2\right] \tag{2.36}$$

$$R_n = R_i + \frac{T_d}{T_o g_m{}^2 R_{ds}}\left[1+\left(\omega C_{gs}R_i\right)^2\right] \tag{2.37}$$

$$T_d = T_o g_m{}^2 R_{ds}\left[\frac{R_n - R_i}{1+\left(\omega C_{gs}R_i\right)^2}\right] \tag{2.38}$$

After placing the results of 2.38 into ADS, it was found that the match to Γ_{opt} was not as good as the values determined by the earlier approach. This is due to the fact that the equations 2.31 and 2.32 take the input Y-parameters of the circuit into consideration, while 2.37 is based completely on R_n and the computed ECP's from the small-signal

model. Even though the methods for calculating T_g and T_d independently yielded non-ambient results for T_g, the fits to F_{min} and Γ_{opt} were more acceptable. Though the user could adjust the values of R_i to achieve a higher T_g, this would change the matching to Γ_{opt} and ultimately void the usefulness of the work for a designer. A study of the effects of R_i on the noise model is discussed in detail in Chapter 5.

2.5 Chapter Summary

This chapter provides an explanation of some of the processes involved with modeling a device meant for low noise or small signal design. Using the small-signal model extraction approach by Dambrine and Cappy [20] and entering data into Special [16] versus bias, the results were satisfactory. All the ECPs generated in Special were entered into a table format which is shown in Appendix C. This table also includes the equivalent noise temperatures T_g and T_d.

Both of the noise modeling methods discussed in this chapter were used in an effort to obtain the best model. The results and conclusions of the model's ability to match the measured data will be discussed in Chapter 5. The two methods for extracting noise temperatures used in this project are evaluated in Chapter 4.

CHAPTER 3

LARGE SIGNAL MODELING THEORY

3.1 Introduction

In addition to small-signal and noise modeling, the second goal to this work is to establish a nonlinear, or large-signal, model for the 6x12.5 um mHEMT in ADS. The primary tool used for this effort is IC-CAP Modeling Software from Agilent [25]. The basic premise behind the system is to take S-parameter and DC-IV measurements and use the built in model algorithms to extract model parameters from that data. This chapter will outline the theory used in the HEMT nonlinear model and also differentiate between other existing models.

It was decided early on to choose a model that would best fit the properties of these new mHEMT devices rather than try to match a pre-determined model. Given that the mHEMT DC-IV curves differ from common MESFETs, it was concluded that a newer procedure appropriate for HEMTs might be needed for this work. There are many models developed for GaAs FETs and HEMTs. The EEHEMT model available in ADS and IC-CAP was chosen because of its versatile nature and also for the reason that this would help broaden the understanding of complex models outside of the widely used Curtice, Curtice-Ettenburg, and Statz models [26,6,7]. These models have already been the study of previous work at USF [27,28].

3.2 Basic Large Signal Model Theory

In the previous chapter, the small signal noise model was demonstrated as being an equivalent circuit model with elements that are bias and temperature dependent, but not frequency or power dependent. The values given for the ECPs are constant with frequency and power at a given DC bias condition. When the bias or temperature changes, so do each of the ECPs in the model. For the large-signal model, prediction should extend to gain compression, harmonic distortion, and power load circles. The large-signal simulation relies on the use of a harmonic balance simulator, whereby the linear circuit is simulated in the frequency domain, the nonlinear circuit is simulated in the time domain [26]. The time domain analyses comes from voltage controlled current sources placed into the small signal equivalent circuit model in the form of equations defining I_{ds}, I_{dg}, and I_{gs} as seen in Figure 3.2.

In all large-signal FET models, a main requirement is to have an equation to predict I_{ds}. This current equation can be modeled by measuring I_{ds} at several values of V_{gs} while sweeping V_{ds} and fitting an appropriate equation to the data. Two other important parameters to characterize are the charge capacitance models. These allow for the change in C_{gs} and C_{gd} at different bias conditions. The drain current of a JFET is described by Sze [29] as

$$I_{ds} = I_p \left[1 - 3\left(\frac{V_g + V_{bi}}{V_p} \right) + 2\left(\frac{V_g + V_{bi}}{V_p} \right)^{3/2} \right] \tag{3.1}$$

for a uniformly doped n-type region. I_p and V_p are defined as the pinch-off current and voltage. V_g is the gate voltage and V_{bi} is the built in potential between the pn junction. A second formula, which is for an arbitrary doping distribution, is given by [29]:

$$I_{ds} = I_p \left[1 - \left(\frac{V_g + V_{bi}}{V_p} \right) \right]^2 \tag{3.2}$$

with certain approximations made to simplify (3.1). Several variations of (3.2) have been reported that extend the applicability to microwave devices.

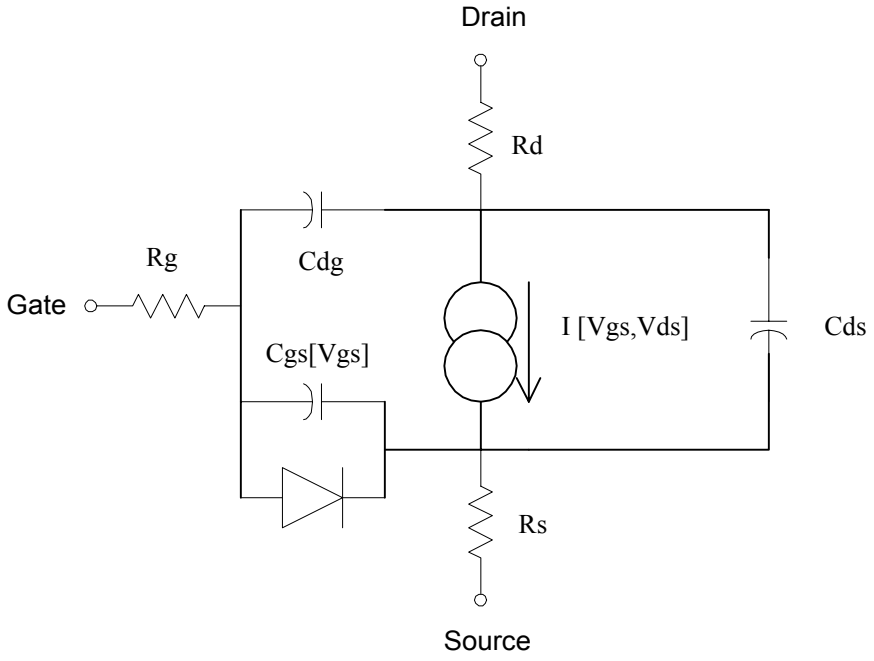

Figure 3.1 Curtice Large Signal Initial Model Representation.

Since the development of the drain current and charge capacitance fitting equations, continual improvement have been made to better calculate various aspects of the device performance. This is evident by the number of available models today. One of the more popular models is the Curtice model which is depicted in Figure 3.1 [7] and a more advanced Curtice Cubic or Curtice-Ettenberg in Figure 3.2 [26]. Shown below is the equation for I_{ds} with the commonly seen hyperbolic tangent function, which provides

a better prediction of values below the saturation current [7]. A list of definitions for the terms in the proceeding equations is shown in Table 3.1.

$$I_{ds} = \beta\left(V_{gs} + V_T\right)^2 \left(1 + \lambda V_{ds}\right) \tanh \alpha V_{ds} \tag{3.3}$$

Table 3.1 Nonlinear Model Parameter Definitions

Parameter	Definition
β	$I_p / V_p^{\,2}$
V_t	Threshold voltage ($V_p + V_{bi}$)
α	Saturation voltage parameter
λ	Channel length modulation parameter

The junction capacitance in the channel can be shown to be

$$C = {dQ(h)}/{dV} \tag{3.4}$$

which when used to define C_{gs} and C_{gd} can be expressed as

$$C_{gs} = {\partial Q_g}/{\partial V_{gs}} \tag{3.5}$$

$$C_{gd} = {\partial Q_g}/{\partial V_{gd}} \tag{3.6}$$

Curtice et al.[26] applies (3.5) and (3.6) to the model for an ideal metal-insulator-semiconductor diode to form (3.7) and (3.8).

$$C_{gs} = \frac{C_{gso}}{\sqrt{1 - \frac{V_{gs}}{V_b}}} \tag{3.7}$$

$$C_{gd} = \frac{C_{gso}}{\sqrt{1 - \frac{V_{gd}}{V_b}}} \tag{3.8}$$

Later, Statz et al. reformed (3.3) into (3.9) [6]. Also the equations for C_{ds} and C_{gd} were changed which include a smoothing function for the symmetry of both gate charges.

$$I_{ds} = \beta \frac{\left(V_{gs} - V_T\right)^2}{1 + B\left(V_{gs} - V_T\right)} \left[1 - \left(1 - \frac{\alpha V_{ds}}{3}\right)^3\right] \left(1 + \lambda V_{ds}\right) \tag{3.9}$$

$$C_{gs} = \frac{C_{gso}}{2\sqrt{1 - \frac{V_{eff}}{V_b}}} \left(\frac{1 + C}{2}\right) + C_{gdo} \left(\frac{1 - C}{2}\right) \tag{3.10}$$

$$C_{gd} = \frac{C_{gso}}{2\sqrt{1 - \frac{V_{eff}}{V_b}}} \left(\frac{1 - C}{2}\right) + C_{gdo} \left(\frac{1 + C}{2}\right) \tag{3.11}$$

$$C = \frac{V_{gs} - V_{gd}}{\sqrt{\left(V_{gs} - V_{gd}\right)^2 - \Delta^2}}$$

$$V_{eff} = \frac{1}{2}\left\{V_{gs} + V_{gd} + \sqrt{\left(V_{gs} - V_{gd}\right)^2 - \Delta^2}\right\}$$

Materka and Kacprzak [30] model the voltage controlled current source shown in (3.12).

$$I_{ds} = I_{dss}\left(1 - V_g \Big/ V_{po} + \gamma V_{ds}\right)^2 \tanh\left(\frac{\alpha V_{ds}}{V_g - V_{po} + \gamma V_{ds}}\right) \tag{3.12}$$

The model often used for USF nonlinear work [27,28], has been the Curtice Cubic or Curtice-Ettenberg model. The earlier nonlinear analysis was meant for the prediction of silicon based devices, but new approaches were needed to simulate the performance of GaAs [26]. The Curtice Cubic expands on the Materka model by measuring avalanche breakdown voltage and uses second and third harmonic voltages for analyzing the transistor. In the paper they have replaced the square-law relation to a cubic relation of I_{ds} and V_{gs} [26].

$$I_{ds} = \left(A_1 + 2A_2 V_x + 3A_3 V_x^2 \right) \tanh \gamma V_{ds} \tag{3.13}$$

where

$$V_x = V_{gs} \left(1 + \beta \left(V_{dso} - V_{ds} \right) \right) \tag{3.14}$$

For large V_{ds} values, the drain currents could override the pinchoff voltages. The pinchoff voltage being the gate voltage which closes the channel and restricts the drain-to-source current flow. This is due to an avalanche gate current caused by punch-thru which is a significant drain-to-source voltage that forces current through a pinched channel. It is noted that this occurrence limits the RF current and output power [26]. This drain-gate avalanche breakdown is defined as I_{dg}. Forward conduction in the gate is modeled by I_{gs}. Two other parameters that are affected by V_{gs} and V_{ds} are R_{ds} and g_m. R_{ds} can also be denoted as the inverse of g_{ds}. The equation for g_{ds} is obtained by differentiating the drain current by V_{ds} and g_m is the drain current differentiated by V_{gs}. The representative circuit for the Curtice Cubic model is given in Figure 3.2.

$$I_{dg} = \begin{cases} \dfrac{V_{dg}(t) - V_B}{R_1}, & V_{dg} > V_B \\ 0, & V_{dg} < V_B \end{cases} \tag{3.15}$$

$$V_B = V_{bo} + R_2 I_{ds}$$

$$I_{gs} = \begin{cases} \dfrac{V_{gs}(t) - V_{bi}}{R_F}, & V_{gs}(t) \geq V_{bi} \\ 0, & V_{gs}(t) \leq V_{bi} \end{cases} \tag{3.16}$$

$$g_{ds} = \frac{1}{R_{ds}} - \beta V_{gs} \left(A_1 + 2A_2 V_x + 3A_3 V_x^2 \right) \tanh \gamma V_{ds} + \frac{\gamma I_{ds} \operatorname{sech}\left(\gamma V_{ds} \right)}{\tanh\left(\gamma V_{ds} \right)} \tag{3.17}$$

$$g_m = \left(A_1 + 2A_2V_x + 3A_3V_x^2\right)\tanh\gamma V_{ds}\left[1+\beta\left(V_{ds0}-V_{ds}\right)\right] \tag{3.18}$$

Both g_{ds} and g_m are defined and measured using DC-IV data by the differentiation of the drain current to either the drain voltage or gate voltage.

$$\frac{\partial I_{ds}}{\partial V_{ds}} = g_{ds} \tag{3.19}$$

$$\frac{\partial I_{ds}}{\partial V_{gs}} = g_m \tag{3.20}$$

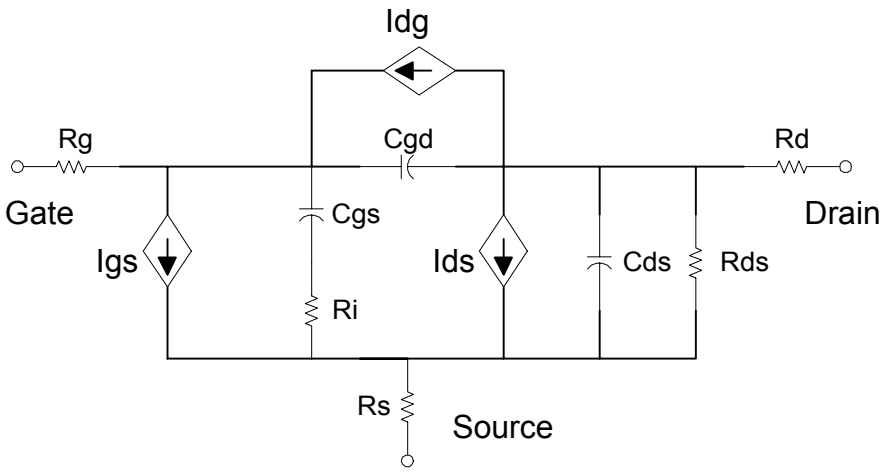

Figure 3.2 Equivalent Circuit Model for Curtic-Ettenburg Model.

With the introduction of newer devices that include InP HEMTs or InGaAs pHEMTs with sub-micron gate lengths, updated models have been proposed to account for the accurate prediction of not only the current and voltage characteristics but the derivatives as well [31]. Angelov et al.[31]has proposed a simple method that includes the hyperbolic tangent gate voltage function in the drain current equation to the voltage dependent capacitance. The theory is that the capacitance changes more before the knee voltage than after, similar to the characteristic of the drain current. If the derivatives of

the drain current equation are not accurate, harmonic predictions such as intermodulation distortion could be invalid [32]. Another aspect considered is the transconductance peak versus gate voltage that is particularly important for HEMTs [31].

As illustrated in the previous models, the form for I_{ds} is best expressed as

$$I_{ds}\left[V_{gs}, V_{ds}\right] = I_{dA}\left[V_{gs}\right] I_{dB}\left[V_{ds}\right] \tag{3.21}$$

which shows the dependent portions of I_{ds} on V_{gs} alone and V_{ds} alone. The Angelov model uses the same notation to describe the V_{ds} dependence as the Curtice model (3.3) but also uses the hyperbolic tangent to describe the V_{gs} dependence because of its "bell-shaped" derivatives that are already available in today's simulators [31]. The denoted expression for I_{ds} is shown below.

$$I_{ds} = I_{pk}\left(1+\tanh\psi\right)\left(1+\lambda V_{ds}\right)\tanh\alpha V_{ds} \tag{3.22}$$

$$\psi = \sum_{i=1}^{n} p_i \left(V_g - V_p + \gamma V_{ds}\right)^i \tag{3.23}$$

I_{pk} is the drain current minus the output conductance. The term Ψ, is a general power series function focused on the gate voltage where maximum transconductance occurs [31]. Because of the familiar responses of $I_d[V_g, V_d]$ and $C_{gs}[V_g, V_d]$ in terms of dependence on gate and drain voltage, the same functions for modeling (1+tanhΨ), were used C_{gs} and C_{gd} [31]. The abbreviated forms are given for these capacitance terms [16]:

$$C_{gs} = C_{gso}\left(1+\tanh\Psi_g\right)\left(1+\tanh\Psi_d\right) \tag{3.24}$$

$$\Psi_g = P_{10} + P_{11}V_g + P_{12}V_g^{\,2} + P_{13}V_g^{\,3} \tag{3.25}$$

$$\Psi_d = P_{20} + P_{21}V_d + P_{22}V_d^{\,2} + P_{23}V_d^{\,3} \tag{3.26}$$

$$C_{gd} = C_{gdp} + C_{gdo}\left(1 + \tanh \Psi_g\right)\left(1 - P_{400} \tanh \Psi_{gd}\right) \tag{3.27}$$

$$\Psi_g = P_{30} + P_{31} V_g + P_{32} V_g^{\,2} \tag{3.28}$$

$$\Psi_{gd} = P_{40} + P_{41} V_{gd} \tag{3.29}$$

P is defined above as

$$\frac{g_{ms}}{I_{pks}} \tag{3.30}$$

in which both the transconductance and drain current are measured in the saturation region of operation.

3.3 IC-CAP EEHEMT Model

The model chosen for this work is Agilent's EEHEMT model in ADS, an empirical model that analyzes the measured characteristics for best fitting of GaAs FETs and HEMTs [25]. The features that are highlighted by the model are

1. Isothermal I_{ds} model that incorporates many process variations
2. A correction for heating in the I_{ds} model
3. Dispersion parameters that fit both high frequency and DC effects
4. A model for I_{gs} that is dependent on both V_{gs} and V_{ds}
5. Ability to predict beyond the measurement limits of the device in the extraction
6. A more accurate charge model

A key feature for this model is the use of the parameter V_{dso}. At this voltage, the equations simplify, allowing easier extraction of certain parameters. Care must be taken in the selection of this voltage which is an important factor for many aspects including the drain current. It is set as an operating point in the saturation region. Before continuing

with the theory behind the model, an explanation needs to be given for each of the parameters in the model. Tables 3.1 through 3.5 given definitions for each term in the proceding equations for a given section.

3.3.1 Drain-Source Current Parameters

The drain-source parameters not only are defined for I_{ds} but also depend upon g_{ds} and g_m. The equations for these parameters are evaluated in four different sections, given the value of V_{gs}. One condition is below the threshold, and all values are set to zero. Another condition is the linear slope of g_m between maximum transconductance and the threshold voltage. The section after maximum transconductance and the point where gm compressions are the two remaining areas. Figure 3.3. displays the transconductance versus V_{gs} and highlights different regions where I_{ds}, g_{ds}, and g_m are defined. A table in Appendix C gives the default values in comparison to those extracted for the 75 um mHEMT.

Table 3.2 Agilent EEHEMT Model Drain-Source Current Parameters [25].

Parameter	Description
V_{to}	Zero-bias threshold
γ	Vds-dependent threshold parameter
V_{go}	Gate-source voltage where gm is maximum
V_{delt}	Controls linearization point for gm characteristic
V_{ch}	Gate-source voltage where gamma no longer effects the IV curve.
gm_{max}	Peak transconductance
V_{dso}	Drain voltage where Vds dependency disappears from equations.
V_{sat}	Ids saturation parameter
κ	Output conductance
P_{eff}	Channel-to-backside self-heating for DC.
V_{tso}	Subthreshold onset voltage

The explanation given in this chapter will be for I_{ds} only (Appendix D contains the complete process for all the extractions). The first examination of the drain current will be in the region where V_{gs} is less than or equal to V_g as defined below.

$$V_{gs} \geq V_g$$

$$V_g = \frac{V_{go} - V_{ch}}{1 + \gamma\left(V_{dso} - V_{ds}\right)} + V_{ch} \tag{3.31}$$

$$I_{ds} = gm_{\max}\left\{V_x - \frac{V_{go} + V_{to}}{2} + V_{ch}\right\} \tag{3.32}$$

$$V_x = \left(V_{gs} - V_{ch}\right)\left(1 + \gamma\left(V_{dso} - V_{ds}\right)\right) \tag{3.33}$$

From equation (3.31), if V_{ds} equals V_{dso} then $V_g = V_{go}$. Also (3.32) will reduce to a simple form that yields (3.34).

$$I_{ds} = gm_{\max}\left(V_{gs} - \frac{V_{go} + V_{to}}{2}\right) \tag{3.34}$$

A second area or condition is when V_{gs} is less than or equal to V_t. In (3.35), V_t is defined as being at or near the zero bias threshold voltage V_{to} depending on the value of V_{dso}. Defining the region below V_t will take into account the dependence on the threshold due to the amount of drain-to-source voltage applied. I_{ds} will be zero in this range.

$$V_t = \frac{V_{to} - V_{ch}}{1 + \gamma\left(V_{dso} - V_{ds}\right)} + V_{ch} \tag{3.35}$$

For $V_t < V_{gs} < V_g$ the current equations becomes (3.36).

$$I_{ds} = \frac{gm_{\max}}{2}\left[\frac{V_{to} - V_{go}}{\pi}\sin\left(\pi\frac{V_x - \left(V_{go} - V_{ch}\right)}{V_{to} - V_{go}}\right) + V_x - \left(V_{to} - V_{ch}\right)\right] \tag{3.36}$$

3.3.2 EEHEMT Gm Compression Parameters

The compression terms for the model are separated into different regions of gate voltage denoted by the terms V_c, V_b, and V_a (3.37-3.39). As before, each section will have its own equation to help model that particular area of the compression side of g_m versus V_{gs}, as shown in Figure 3.3. The corresponding compression parameters and those represented in Figure 3.3 can be seen in Table 3.2.

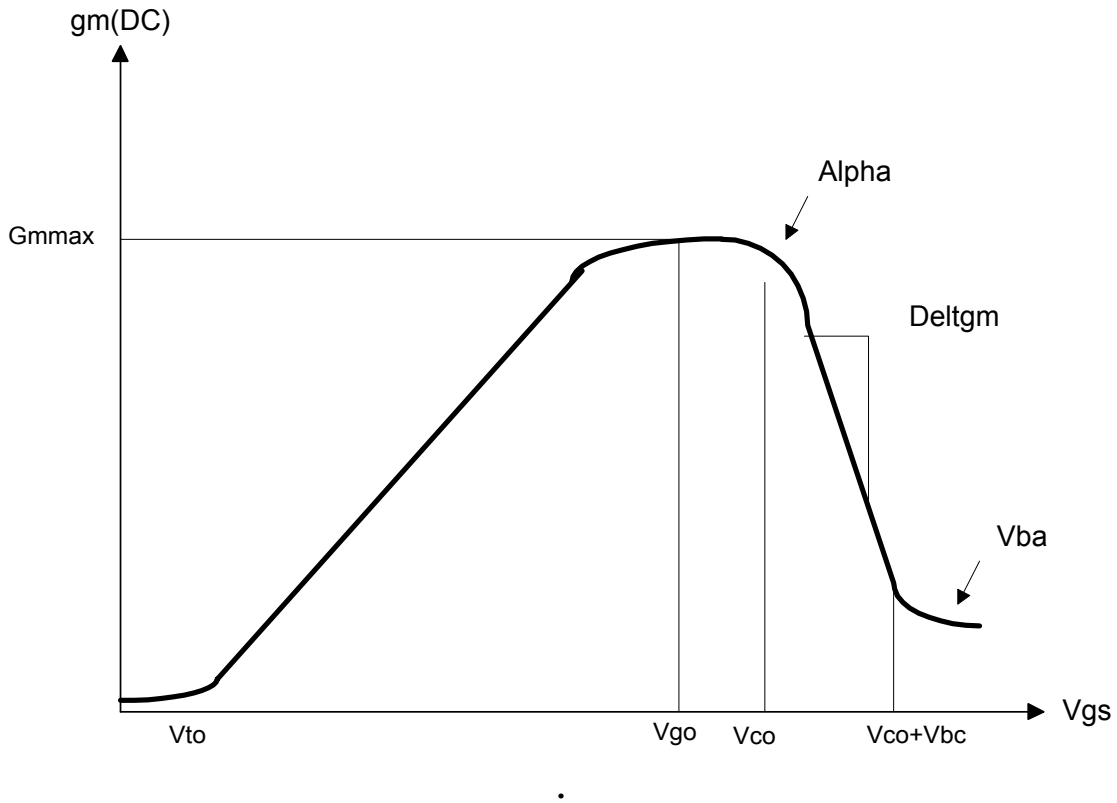

Figure 3.3 Typical Gm Versus Vgs plot with Corresponding Model Parameters Displayed.

Table 3.3 Agilent EEHEMT Model Drain-Source Current Parameters [25].

V_{co}	Voltage where gm compression begins.
μ	Adds Vds dependence to gm compression onset.
V_{BA}	Gm compression "tail-off".
V_{BC}	Gm roll-off to tail-off transition voltage.
Δgm	Slope of gm com`pression.
α	Gm saturation to compression transition.

The regions of the chart in Figure 3.3 from V_{co} onward will be defined as V_c, V_b, and V_a. All compression equations are at V_{gs} greater than V_{co}. The term $\mu(V_{dso}-V_{ds})$ adds a dependence on the transconductance which may shift the compression of the device versus gate voltage. Each of these sections is defined by a change in the slope of g_m.

$$V_c = V_{co} + \mu\left(V_{dso} - V_{ds}\right) \tag{3.37}$$

$$V_b = V_{bc} + V_{co} + \mu\left(V_{dso} - V_{ds}\right) \tag{3.38}$$

$$V_a = \left(V_{bc} - V_{ba}\right) + V_{co} + \mu\left(V_{dso} - V_{ds}\right) \tag{3.39}$$

For $V_{gs} < V_b$ the drain current is

$$I_{ds}^{\ comp} = I_{ds} - I_{dsv} \tag{3.40}$$

$$I_{dsv} = \Delta gm\left(\frac{1}{2}\left(\left(V_{gs} - V_c\right)D + \alpha^2 \log\left[\frac{\left(V_{gs} - V_c\right) + D}{\alpha}\right]\right) - \alpha\left(V_{gs} - V_c\right)\right) \tag{3.41}$$

$$D = \sqrt{\alpha^2 + \left(V_b - V_c\right)^2} \tag{3.42}$$

For Vgs $\geq$ Vb, then I_{ds} becomes (3.43).

$$I_{dso}^{\ comp} = I_{dso} - \frac{a}{b+1}\left[\left(V_{gs} - V_a\right)^{b+1} - V_{BA}^{\ b+1}\right] - g_{mo}\left(V_{gs} - V_b\right) - I_{dsv} \tag{3.43}$$

$$a = \frac{\Delta gm\left[\sqrt{\alpha^2 + \left(V_b - V_c\right)^2} - \alpha\right] - g_{mo}}{V_{BA}^{\ b}} \tag{3.44}$$

$$b = \frac{S_{vb} \square V_{BA}}{\Delta gm\left[\sqrt{\alpha^2 + \left(V_b - V_c\right)^2} - \alpha\right] - g_{mo}} \tag{3.45}$$

$$S_{vb} = \Delta gm \frac{V_{BC}}{\left(\sqrt{\alpha^2 + V_{BC}^{\ 2}}\right)} \tag{3.46}$$

To ensure that g_m does not approach negative values at high gate voltages, a constraint is placed in (3.47):

$$\Delta gm < \frac{g_{mo}}{\sqrt{\alpha^2 + V_{BC}{}^2} - \alpha} \tag{3.47}$$

The preceding formulas for compressed I_{ds} can be entered into a form that is comparable to (3.3), which is the standard Curtice nonlinear model equation:

$$I_{ds} = I_{ds}{}^{comp}\left(1 + \lambda V_{ds}\right)\tanh\left(\frac{3V_{ds}}{V_{sat}}\right) \tag{3.48}$$

The approaches outlined so far provide accurate fitting to static IV data but does not correct for self-heating. A thermal model that explains this self-heating in the IV curves as a negative resistance is adopted from Canfield [8]. Using the thermal fitting parameter P_{eff}, the temperature dependence of I_{ds}, g_m and g_{ds} are shown:

$$I_{ds} = \frac{I_{ds}}{1 + \frac{I_{ds}V_{ds}}{P_{eff}}} \tag{3.49}$$

$$g_m = \frac{g_m}{\left[1 + \frac{I_{ds}V_{ds}}{P_{eff}}\right]^2} \tag{3.50}$$

$$g_{ds} = \frac{g_{ds} - \frac{I_{ds}{}^2}{P_{eff}}}{\left[1 + \frac{I_{ds}V_{ds}}{P_{eff}}\right]^2} \tag{3.51}$$

3.3.3 Dispersion Current Parameters

Now that the issues of DC operation in terms of V_{ds} and V_{gs}, compression, and self-heating effects have been discussed, dispersion effects can be presented. Dispersion is a change in the DC properties of a device from high frequency stimulation. Dispersion effects can be attributed to thermal and electron trapping [12]. Although silicon devices have minimal thermal dispersion, GaAs devices exhibit greater thermal resistance and experience large changes in junction temperature [12]. This thermal dispersion can be seen by a downward slope in the DC-IV plot at higher biases and drain voltages. Pulsed IV measurements are needed to eliminate dispersion effects in DC data as compared to a standard static IV measurement.

Another problem encountered at high frequencies is electron charge trapping. Trapping can cause dispersion in the output admittance or transconductance of a FET or HEMT. When electrons are transferred between the conduction band and the energy levels of the bandgap or interface traps, the efficiency at high frequencies is restricted by the device free charge-transfer [29]. The rate at which the electrons are emitted into the channel compared to the rate in which they are trapped will determine the transition frequency at which dispersion will begin. At high frequencies the traps cannot keep up with the brisk signal oscillations and an output conductance that is different from that determined by static measurements results [33]. The model parameters for dispersion effects are given in Table 3.3.

Table 3.4 Agilent EEHEMT Model Dispersion Parameters [25].

R_{db}	Dispersion output impedance.
C_{bs}	Dispersion capacitance.
G_{dbm}	Additional branch conductance at Vds=Vdsm.
K_{db}	Controls Vds dependence on Gdbm.
V_{dsm}	Voltage where Gdbm becomes constant.
Gm_{maxac}	Peak transconductance (AC).
V_{eltac}	Controls linearization point for gm (AC).
V_{toac}	Threshold voltage (AC).
$Gamma_{ac}$	Vds-dependent threshold (AC).
$Kappa_{ac}$	Output conductance (AC).
P_{effac}	Self-heating parameter (AC).

Above the transition frequency, or the frequency where AC dispersion effects begin, I_{ds} will be defined by two drain current expressions, the DC and AC models. The attempt to apply values to R_{db} and C_{bs} will involve linearizing the output Y-parameters between zero frequency and infinity. The AC dispersion parameters follow a time constant defined by a frequency midway between DC and infinity.

$$I_{ds} = I_{ds}\left(DC\right) + I_{db} \tag{3.52}$$

$$Y_{21} = \frac{\partial I_{ds}}{\partial V_{gs}} + \frac{\partial I_{db}}{\partial V_{gs}}\left(1 - \frac{1}{1 + j\omega C_{bs} R_{db}}\right) \tag{3.53}$$

$$Y_{22} = \frac{\partial I_{ds}}{\partial V_{ds}} + \left(\frac{\partial I_{db}}{\partial V_{ds}} + \frac{1}{R_{db}}\right)\left(1 - \frac{1}{1 + j\omega C_{bs} R_{db}}\right) \tag{3.54}$$

Evaluating these expressions at the two frequency limits defined above will yield the equations (3.55)-(3.58). Also shown is the time constant at operating frequency f_0.

$$\omega = 0$$

$$\mathrm{Re}\left(Y_{21}\right) = \frac{\partial I_{ds}}{\partial V_{gs}} \tag{3.55}$$

$$\mathrm{Re}\left(Y_{22}\right) = \frac{\partial I_{ds}}{\partial V_{ds}} \tag{3.56}$$

$$\omega = \infty$$

$$\mathrm{Re}\left(Y_{21}\right) = \frac{\partial I_{ds}}{\partial V_{gs}} + \frac{\partial I_{db}}{\partial V_{gs}} \tag{3.57}$$

$$\mathrm{Re}\left(Y_{22}\right) = \frac{\partial I_{ds}}{\partial V_{ds}} + \frac{\partial I_{db}}{\partial V_{ds}} + \frac{1}{R_{db}} \tag{3.58}$$

$$f_0 = \frac{1}{2\pi R_{db} C_{bs}} \tag{3.59}$$

The difference of the AC and DC drain currents plus a term dependent on drain voltage will establish a value for I_{db}. If the eight AC dispersion parameters are the same as the DC parameters, then the dispersion relies completely on I_{dbp}. If the user wants to eliminate the dispersion model then G_{dbm} would be set to zero.

$$I_{db} = I_{ds}(AC) - I_{ds}(DC) + I_{dbp} \tag{3.60}$$

$$I_{dbp} = \sqrt{\frac{G_{dbm}}{K_{db}}} \tan^{-1}\left(\left(V_{ds} - V_{dsm}\right)\sqrt{K_{db} G_{dbm}}\right) + G_{dbm} V_{dsm} \tag{3.61}$$

3.3.4 Charge Parameters

The charge model for the EEHEMT model is based on two ports of the device, the gate and the drain. The gate charge model consists of two gate capacitances measured from the Y-parameters (see equations (3.5) and (3.6)). These capacitances are then split between two charges Q_{gc} and Q_{gy}. The output charge model is based on C_{dso}.

Table 3.5 Agilent EEHEMT Model Charge Parameters [25].

C_{11o}	Maximum input capacitance for Vds=Vdso And Vdso>Deltds.
C_{11th}	Minimum input capacitance for Vds=Vdso
V_{infl}	Inflection point inC11-Vgs characteristic.
$Delt_{gs}$	C11th to C11o transition voltage.
$Delt_{ds}$	Linear region to saturation region transition.
Lambda	C11-Vds slope parameter.
C_{12sat}	Input transcapacitance for Vgs=Vinfl and Vds>Deltds.
C_{gdsat}	Gate-drain capacitance for Vds>Deltds.
R_{is}	Source channel resistance.
R_{id}	Drain channel resistance.
Tau	Source-to-drain charging delay.
C_{dso}	Drain-source capacitance.

The two capacitance terms are defined in (3.62).

$$C_{11} = \frac{\partial Q_g}{\partial V_{gs}} \qquad C_{12} = \frac{\partial Q_g}{\partial V_{ds}} \tag{3.62}$$

The gate charge expression shown in (3.63) is a single variable that can be expressed through its derivatives as C_{11} and C_{12}. Applying (3.62) with (3.63), one obtains an expression for C_{11} as given in (3.67). After C_{11} is defined, C_{12} can be expressed according to (3.68).

$$Q_g = \left[\frac{C_{11o} - C_{11th}}{2} g\left(V_j\right) + C_{11th}\left(V_j - V_{\inf l}\right)\right]\left[1 + \lambda\left(V_o - V_{dso}\right)\right] - C_{12sat} V_o \tag{3.63}$$

$$g\left(V_j\right) = V_j - V_{\inf l} + \frac{\Delta gs}{3} \ln\left(\cosh\left(\frac{3}{\Delta gs}\left(V_j - V_{\inf l}\right)\right)\right) \tag{3.64}$$

$$V_j = \frac{1}{2}\left(2V_{gs} - V_{ds} + V_o\right) \tag{3.65}$$

$$V_o = \sqrt{{V_{ds}}^2 + {\Delta_{ds}}^2} \tag{3.66}$$

$$C_{11} = \left[\frac{C_{11o} - C_{11th}}{2}\left(1 + \tanh\left[\frac{3}{\Delta gs}\left(V_j - V_{\inf l}\right)\right]\right) + C_{11th}\right]\left[1 + \lambda\left(V_o - V_{dso}\right)\right] \tag{3.67}$$

$$C_{12} = \frac{C_{11}}{2}\left[\frac{V_{ds}}{V_o} - 1\right] + \left[\frac{C_{11o} - C_{11th}}{2} g\left(V_j - V_{\inf l}\right)\right]\lambda - C_{12sat}\frac{V_{ds}}{V_o} \tag{3.68}$$

From examination of Figure 3.5 it is seen that the gate charge is split between two variables, Q_{gy} and Q_{gc}. The inclusion of two charges allows the use of two gate resistances that model charge delay from the depletion region to the channel [33]. The next two charge equations fulfill symmetry placed on each gate charge using the respective voltages V_{gc} and V_{gy}.

$$Q_{gy}\left(V_{gc},V_{gy}\right)=\left\{Q_g\left(V_{gc},V_{gc}-V_{gy}\right)-C_{dsat}V_{gc}\right\}f_2+C_{gdsat}V_{gy}f_1 \tag{3.69}$$

$$Q_{gc}\left(V_{gc},V_{gy}\right)=\left\{Q_g\left(V_{gc},V_{gc}-V_{gy}\right)-C_{dsat}V_{gy}\right\}f_1+C_{gdsat}V_{gc}f_2 \tag{3.70}$$

$$f_1=\frac{1}{2}\left[1+\tanh\left(\frac{3}{\Delta ds}\left(V_{gc}-V_{gy}\right)\right)\right] \qquad f_2=\frac{1}{2}\left[1-\tanh\left(\frac{3}{\Delta ds}\left(V_{gc}-V_{gy}\right)\right)\right]$$

Through differentiation of the gate charge with the respective gate charge voltages, an expression of each capacitance is achieved. The branch charge derivatives are shown in (3.73) but are not expanded.

$$C_{ggy}=\frac{\partial Q_g}{\partial V_{gy}}=-C_{12}\left(V_{gc},V_{gc}-V_{gy}\right) \tag{3.71}$$

$$C_{ggc}=\frac{\partial Q_g}{\partial V_{gc}}=C_{11}\left(V_{gc},V_{gc}-V_{gy}\right)+C_{12}\left(V_{gc},V_{gc}-V_{gy}\right) \tag{3.72}$$

$$\frac{\partial Q_{gy}}{\partial V_{gy}} \qquad \frac{\partial Q_{gy}}{\partial V_{gc}} \qquad \frac{\partial Q_{gc}}{\partial V_{gc}} \qquad \frac{\partial Q_{gc}}{\partial V_{gy}} \tag{3.73}$$

When $V_{ds} = V_{dso}$ the capacitance C_{11} is solely dependent on V_{gs} [33]. Figure 3.4 displays this dependence and the parameters associated with modeling C_{11}.

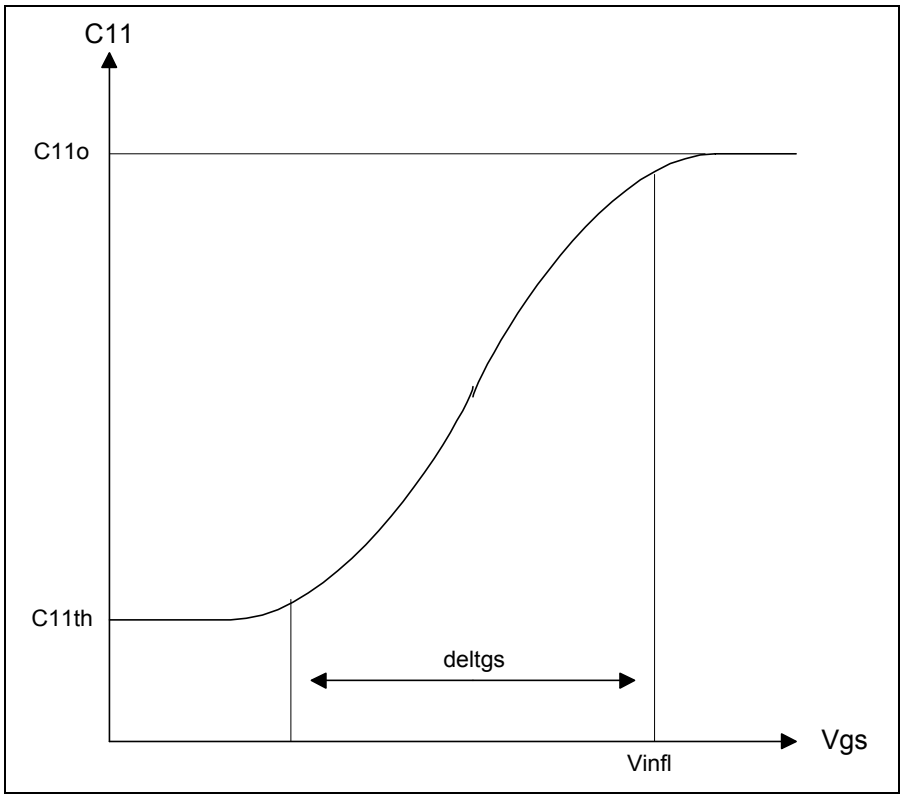

Figure 3.4 C_{11}-V_{gs} Dependency at V_{ds}=V_{dso} Using the Gate Charge Parameters.

The output charge is modeled with a constant capacitance *Cdso*. The output charge changes as a function of V_{ds} only as can be seen in (3.74). The delay seen in the drain current is represented by a time domain function in (3.75). The expression for drain current delay in the frequency domain incorporated, in small signal models, is also shown.

$$Q_{ds} = C_{dso} V_{ds} \tag{3.74}$$

$$I_{ds}(t) = I_{ds}\left(V_{gs}(t - Tau), V_{ds}(t)\right) \tag{3.75}$$

$$gm^{-j\omega Tau} \tag{3.76}$$

3.3.5 Gate Forward Conduction and Breakdown

The forward conduction in the EEHEMT model is characterized by a basic diode expression. The breakdown model incorporates a dependence on both gate-drain and gate-source junctions [33]. For HEMT devices, measuring breakdown voltages usually results in the destruction of the transistor. It is assumed that the user knows V_{br} from the manufacturer and will enter this into the parameter list. Measuring breakdown voltage is highly destructive for GaAs based devices and even more for so InP devices. As such, breakdown characteristics were omitted from the described modeling extraction process. The breakdown voltage can be easily measured, though, with a DC power supply, an accurate current meter, and plenty of devices.

Table 3.6 Agilent EEHEMT Model Forward Conduction and Breakdown Parameters [25].

Is	Gate junction reverse saturation current.
N	Junction ideality factor.
K_{bk}	Breakdown current coefficient at threshold.
V_{br}	Breakdown onset voltage.
I_{dsoc}	Open channel Ids.
N_{br}	Breakdown current exponent parameter.

$$I_{gs}\left(V_{gs}\right) = Is\left[e^{\frac{qV_{gs}}{nKT}} - 1\right] \tag{3.77}$$

$$I_{gd}\left(V_{gd}, V_{gs}\right) = -K_{bk}\left[1 - \frac{I_{ds}\left(V_{gd}, V_{gs}\right)}{I_{dsoc}}\right]\left(-V_{gd} - V_{br}\right)^{N_{br}} \tag{3.78}$$

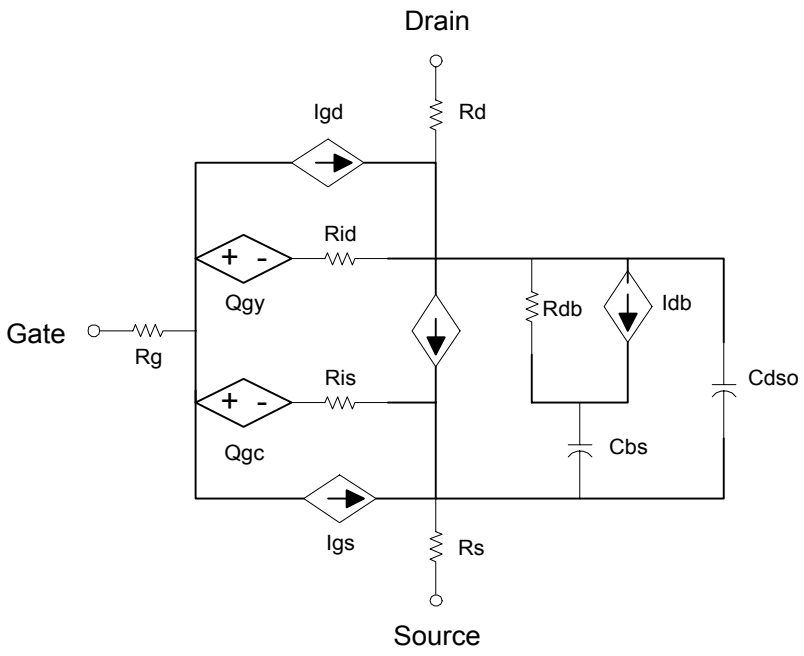

Figure 3.5 Equivalent Circuit Model of the Agilent EEHEMT Model.

3.4 Chapter Summary

Presented in this chapter are the fundamental principles behind nonlinear modeling and how the EEHEMT model is built from previous models. The underlying goal is to help establish an understanding as to how this particular model can simulate certain properties of the supplied mHEMT. The EEHEMT model uses several drain-source current equations to characterize the Ids given different areas of Vgs. This allows for fitting to many different process types. This same approach is taken for both transconductance and Rds. The charge model contains a closed form expression which fits bias with its derivatives separated through node charges and follows similar work from Statz et al. [6] for its smoothing functions [33].

The EEHEMT model also includes a dispersion model for both high frequency conductance and DC attributes. In addition, the transconductance has compression modeling features that can be user modified to match harmonic power and TOI

measurements. Power added efficiency is also tailored from this same function given that the DC model is accurate. Other features include gate forward conduction, breakdown, and scaling of the model. In Chapter 5, the capabilities of this model versus measured data will be presented.

CHAPTER 4

MODEL EXTRACTION AND MEASUREMENT

4.1 Introduction

In Chapters 2 and 3, the modeling methods were described. In this chapter, changes were made to the modeling procedures during the course of this work in order to model the Raytheon mHEMT. These changes were made because of the nature of the device or an inability to measure the device in ranges that would allow accurate extraction. Furthermore, the techniques and equipment will be listed so that the reader may duplicate or validate the methods used for this project.

4.2 Small-Signal Model Extraction

The majority of the small-signal extraction was implemented using the software, SPECIAL [16]. Most of the data used for this model was obtained from the ATN NP5 noise parameter measurement system [10]. The ATN software is operated on a Windows based computer and controls all instruments involved in the measurement through a General Purpose Interface Bus (GPIB) link. The ATN software can output both S-parameters and noise parameters into an "S2p" file that is easily translated into ADS. The S2p file format accommodates a list of s-parameters and noise parameters versus frequency. An example of the S2p file is in Appendix F.

The instrument setup for the noise data is displayed in Figure 4.1. It consists of an HP 8510B VNA, HP 8970B Noise Figure Meter, HP 8971C 26 GHz Noise Test Set, HP 8340A Synthesized Source, HP Bias Supply, ATN NP5 Controller, and a personal

computer. The system at USF uses a single source to provide the signal to the VNA test set for S-parameters and the LO for the 8971C. The NP5 controller uses a switch box to send the signal from the RF source to the needed test set when executing either S-parameter or noise measurements. The controller also regulates the switch in the source tuner module to provide the signal for the VNA test set or the noise source. The source tuner is controlled electronically by a diode based tuning system designed for low power use only. This allows for fast sweeps through many different tuner states, which in turn permits all tuner states to be characterized during the noise calibration.

The noise calibration is broken into two main parts. The first involves finding the noise figure of the receiver, which includes the noise figure meter, noise test set, pre-amplifier, output cable and connections. The second part is to calibrate the noise source to the DUT input reference plane and account for reflections caused by the different tuner states. A thru-reflect-line, TRL, calibration on the GaAs wafer moves the reference planes to the input of the mHEMT [34]. This was a custom calibration procedure using the line lengths and the effective dielectric of the wafer. The delay lines, thru length, and open standards are entered into the TRL calibration setup using the front panel operation of the VNA.

The noise measurement is based on the equation for noise figure of a two-port device (4.1). The four noise parameters are F_{min}, R_n, and Γ_{opt} (Γ_{opt} is complex). When the input reflection presented to the device matches Γ_{opt}, the second term of equation (4.1) goes to zero leaving just F_{min}. This tuner state will provide the data for F_{min} and Γ_{opt}. The noise resistance, R_n, can be derived from the noise figure at 50 Ohms or zero reflection coefficient [35]. The value is obtained from (4.2).

$$F = F_{\min} + \frac{4r_n \left|\Gamma_s - \Gamma_{opt}\right|^2}{\left(1-\left|\Gamma_s\right|^2\right)\left|1+\Gamma_{opt}\right|^2} \tag{4.1}$$

$$R_n = \left(F_{\Gamma s=0} - F_{\min}\right)\frac{\left|1+\Gamma_{opt}\right|^2}{4\left|\Gamma_{opt}\right|^2} \tag{4.2}$$

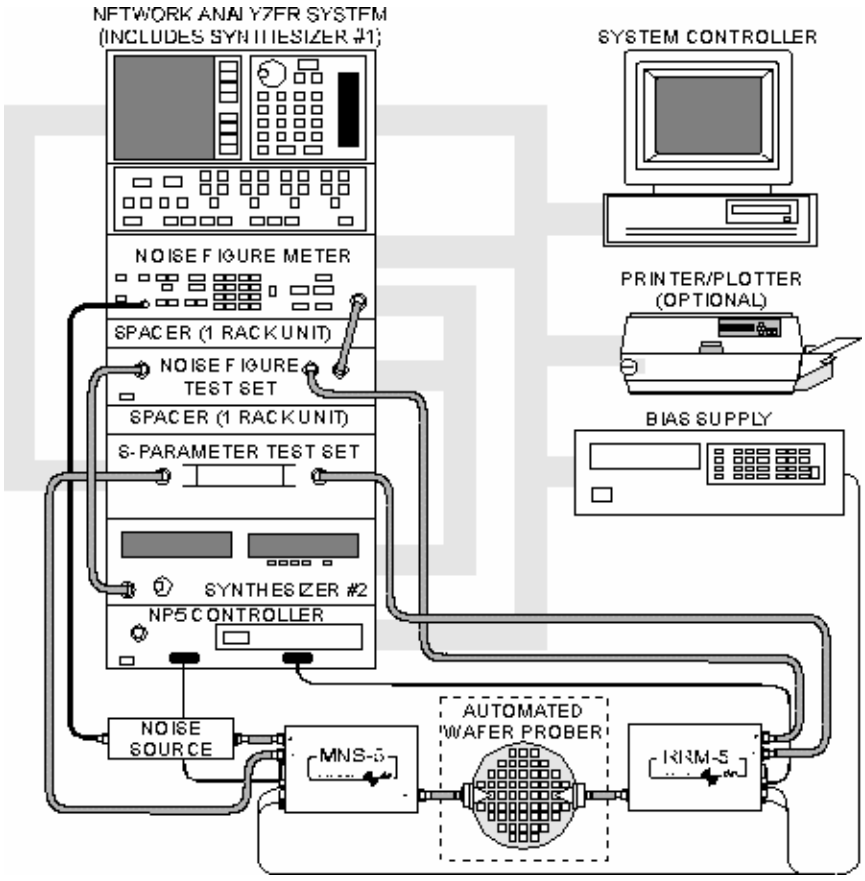

Figure 4.1 ATN Noise Parameter System.

The data file in the s2p format is inserted into SPECIAL and is executed using the hot FET extraction. This process is for the intrinsic Y-parameters only so the extrinsic

parameters must be dealt with first. The first files needed will be for the forward conduction and pinched FET measurements. Both of these measurements are at a drain voltage of zero. S-parameters are taken at a gate voltage past negative pinchoff and at a forward positive voltage, also known as Cold FET. In Figure 4.2, a schematic representing a transistor that is forward biased with zero drain voltage presents the gate capacitance C_g, the channel resistance R_c, and the Schottky barrier equivalent impedance R_{dy}.

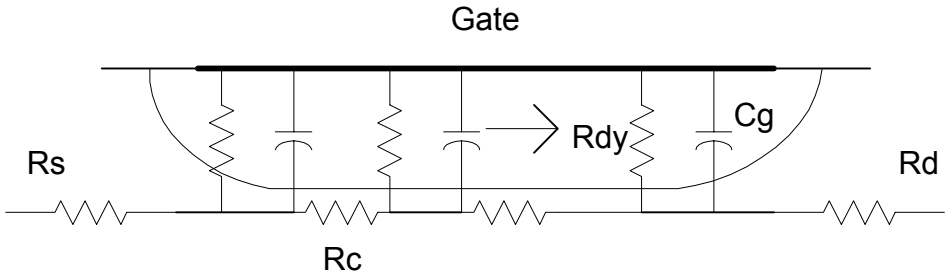

Figure 4.2 Equivalent Circuit Model of a Transistor with V_{ds}=0 [21].

The parasitic inductance values were easily acquired because of the frequency dependence of the imaginary part of equations (2.1)-(2.3). In this effort, the extracted source inductance was large for this size device. Usually the normal value will be below 10 pH but for this mHEMT the value is 53.7 pH. The reason for this is the two large source vias as seen in Figure 1.3. Because the values for the parasitic resistances are extremely small and their dependence on I_g in equation (2.1) is problematic, a new procedure outlined by Yang and Long [36] was used. This procedure uses forward gate biasing at several different currents versus voltage. The differentiation between the current and voltage is equated into resistances.

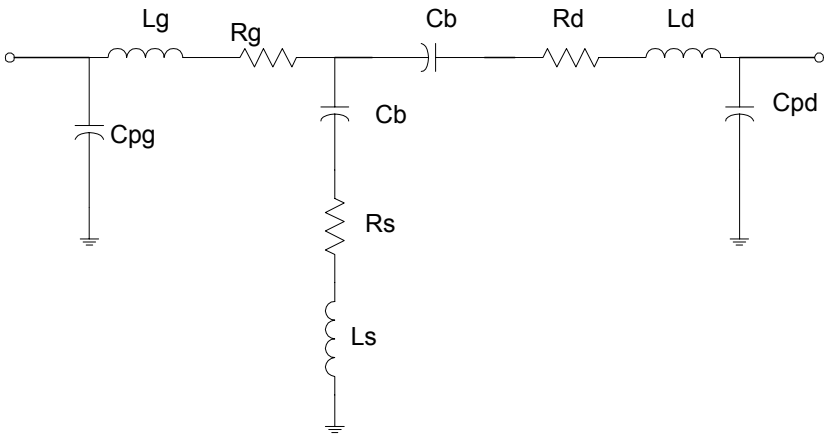

Figure 4.3 Equivalent Circuit for a MESFET at Pinch-Off with V_{ds}=0.

For the pinched FET extraction, the value extracted for the pad capacitance at the gate and drain was 4.91 fF. The equivalent circuit representation of the transistor under the pinch-off condition is displayed in Figure 4.3. The term C_b in the schematic represents the fringing capacitance from the gate due to the depletion layer extending into the channel [55]. These extrinsic capacitances can be omitted depending on the effect they have on the simulation. Usually these values are too small to have any significant effect.

When the user has verified all the extrinsic values entered into SPECIAL, intrinsic extraction can proceed. If the values for the parasitics are not good, the hot FET extraction will give poor results. These extraction results can be inadequate matching of the ECPs to the measured data or extracted values that are not consistent with the device topology. As noted earlier, the problematic extraction of the parasitic resistances resulted with negative values or no solution at all. After the hot FET extraction routine is activated, a display of the frequency dependent properties of the intrinsic capacitances can be viewed. In the display, there is an option to omit frequencies that could provide bad results to the overall averaged value. Also

the values for *Tau* and g_m can be viewed. The final results of a particular extraction can be seen in Figure 4.4.

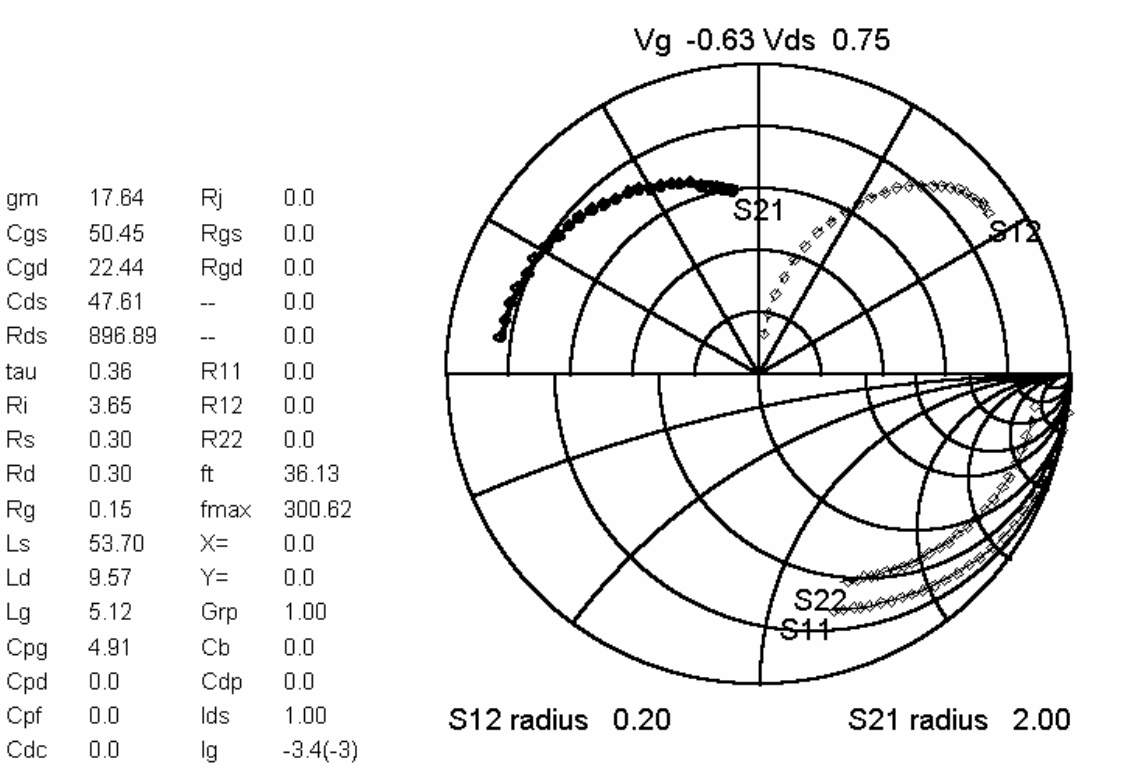

Figure 4.4 Results of an Extraction using SPECIAL. The device is biased at V_{ds} of .75 volts and V_{gs} of -.63 volts. The four s-parameters are displayed along with the % difference between model and measured data in top left corner.

In Figure 4.4, the S-parameters are presented in magnitude and angle format. S_{11} and S_{22} are on the lower half in the Smith Chart and S_{12} and S_{21} are in the upper half of a polar chart. All the ECPs are exhibited on the left including the percentage difference between model and measured data. The user only needs to export the ECPs to a file to enter into ADS.

4.3 Noise Modeling

Since there were no commercial noise modeling products available, the modeling was done by custom "in house" software or calculation. Although the methods described in Chapter 2 sketch out a basic procedure to model noise data, the process requires better understanding of the techniques than just small-signal modeling. SPECIAL performs all the small-signal modeling work with very little input and still achieves good results. In comparison noise modeling requires knowledgeable input from the user.

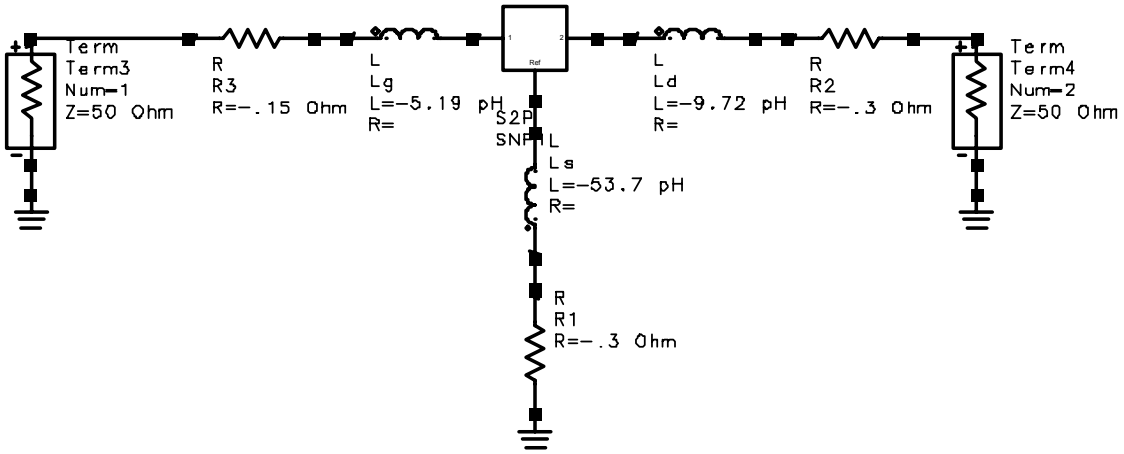

Figure 4.5 Project Schematic for the Two-Port Noise File with Extrinsic Elements Subtracted using Negative Element Values.

Since the model was to be utilized in ADS, the extraction was also designed to be used in this simulator. In Figure 4.5, the schematic for the two-port noise parameter file with negative extrinsic elements is shown. The negative values for parasitic resistances and inductances are subtracted from the S-parameters as a means of de-embedding. C_{pg} is also subtracted from the calculation although it does not affect the results. Calculated values for the gate and drain temperatures are denoted herein as T_g and T_d, respectively. The other procedure is to calculate the Y-parameters from the extracted small-signal model using

equations (2.4) and (2.6). This method is noted as using the lower case of the previous method t_g and t_d. The calculation schematic used for the noise modeling is presented in Appendix E.

In Figures 4.6 and 4.7, sample values for T_d and T_g are calculated by ADS. The user must then decide how to interpret the results given. Raytheon engineers average the values of both T_g and T_d over frequency with some points omitted for better fitting [37]. Once again this relies on the user to determine what values might be acceptable.

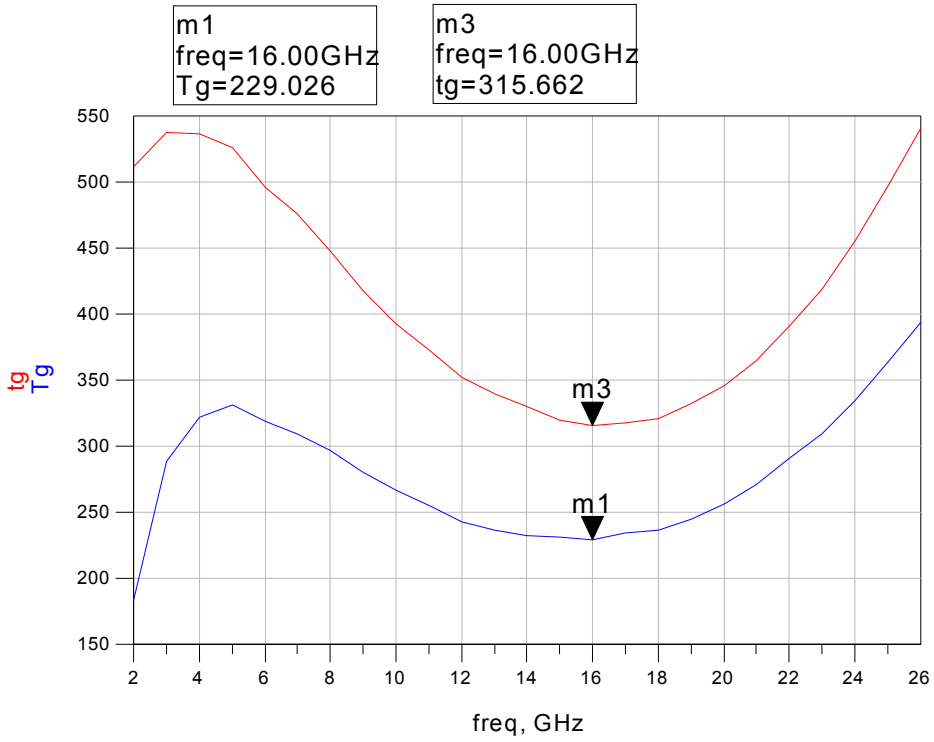

Figure 4.6 Extraction of T_g and t_g Using the Two Pre-described Methods over Frequency.

From Figure 4.6, it is seen that the range of t_g is from 315 to 525 K whereas T_g ranges from 229 to 350 K. Choosing a temperature for T_g is often tricky and does not necessarily

provide a good fit to F_{min} or the optimum noise match. The average value over frequency for one bias point might not work on the next. Careful evaluation of the physically real noise data can shed some light on which frequencies might present problems to the noise model. In the validation graphs for this work, all data exhibited is from the first extraction. In this effort it was found that the method using the S-parameter data with negative extrinsic elements worked the best to provide the intrinsic Y-parameters for noise extraction. From the data as represented in Figure 4.6, the best fitting was generally near the lowest value over frequency.

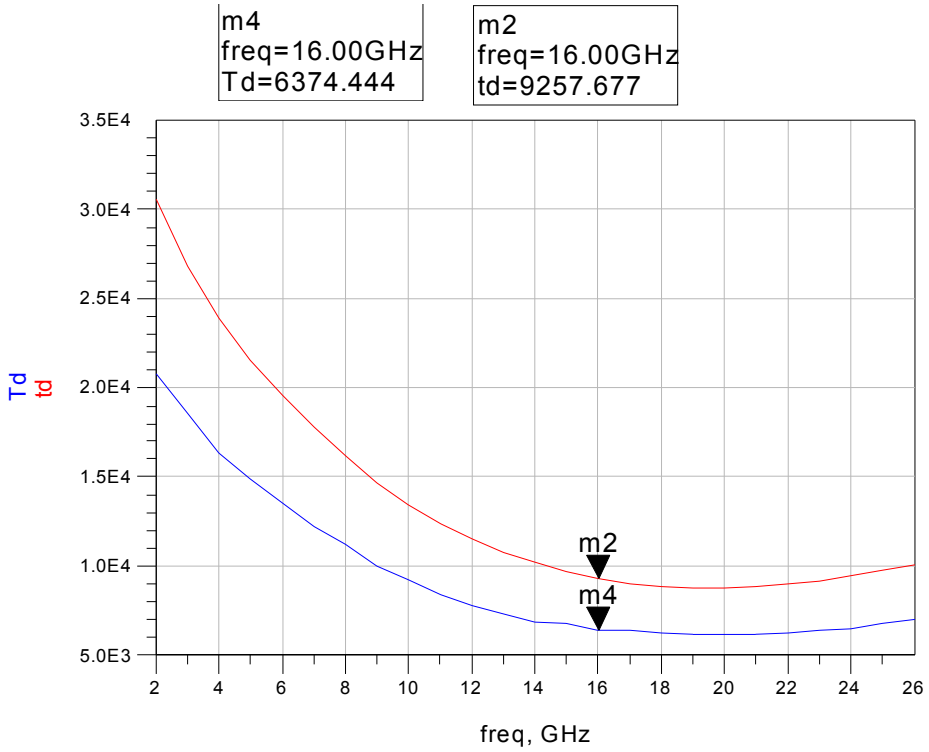

Figure 4.7 Extraction of T_d and t_d Using the Two Pre-described Methods over Frequency.

From the experience gained with these low noise devices, the best range to choose for T_d for the measured mHEMT is from 16 to 26 GHz. The best fitting for the drain temperature was using the same technique as discussed for T_g. There is not enough data though to determine if this is the best fit for T_d and T_g beyond 26 GHz because the actual device range

can go beyond 110 GHz. There is only speculation as to what changes happen in the higher frequencies and if F_{min} is truly linear with frequency, as most conventional models would predict.

The values for T_g have to be considered even more carefully than T_d due to the effect T_g can have upon Γ_{opt}, or the best noise match. It was found that the best match was below the averaged value of T_g over frequency. The slope of F_{min} is also dependent on T_g and T_d with respect to the ECPs of the small-signal model, in particular R_i for T_g and R_{ds} for T_d. Again, the best fitting overall resulted from using T_g below the average value over frequency and using T_d in the flat range of values at the higher frequencies. The file that exhibits extracted values in the ADS model is shown in Appendix C.

4.4 Large-Signal Modeling

The nonlinear modeling process utilized Agilent's IC-CAP software [25]. IC-CAP is designed to meet all nonlinear modeling requirements in one setup. The only instruments needed are a VNA capable of measuring S-parameters through the range of frequencies desired, and a computer controlled bias supply. For this setup, a 50 GHz HP8510C VNA was used in conjunction with a HP 4142 bias supply. The bias tees used in conjunction with the HP 4142 use bias sense and force to allow accurate monitoring of the actual voltage and current as close to the device as possible. All the DC measurements are performed first, followed by AC parameter measurement and extraction.

In the setup used for this project, the DC measurements were executed with 50 Ohm terminations on the RF input ports of the bias tees. This helped to stabilize the DC current and exclude any outside resonating influence or leakage. The RF measurement included a front panel VNA TRL calibration using the supplied GaAs calibration substrate, called

COW4a, and reading the S-parameters using the system software. The COW4a consists of multiple delay lines with 500 um short, open, and 1000 um thru line. The delay lines used were 5820, 3400, 2200, and 1600 um. The substrate is the same GaAs process as the mHEMT wafers and is 4 mils thick. By measuring S-parameters over different biases, the charge parameters in the model can be extracted. All the measurements were conducted from a UNIX station with IC-CAP controlling the HP 8510C and the HP 4142. A representation of the setup used and the equipment involved is shown in Figure 4.8.

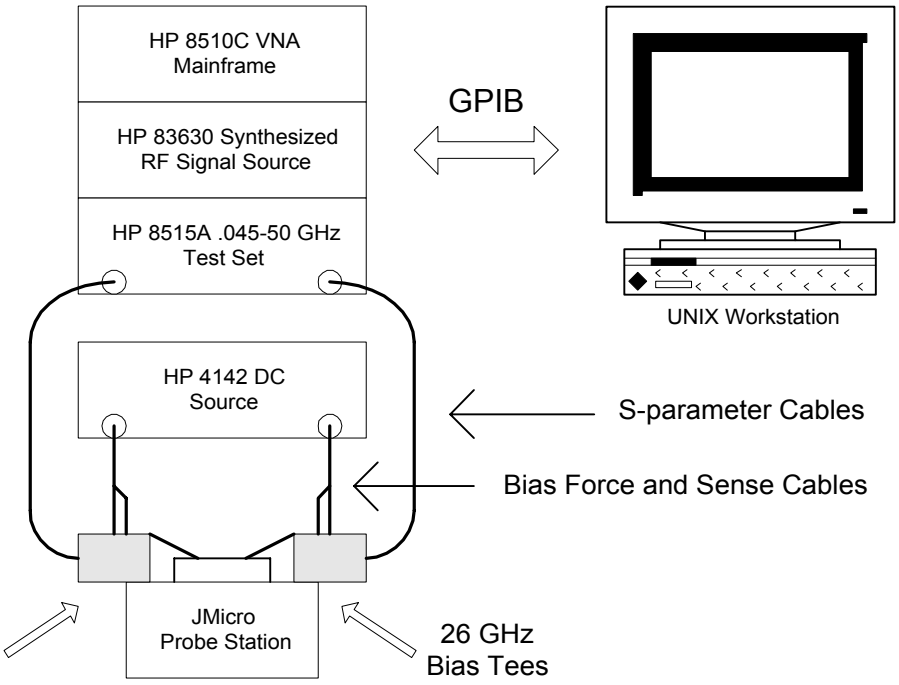

Figure 4.8 IC-CAP Instrument and Computer Setup.

Following each subsection will describe the DC and AC measurements and what is extracted from each session. These sessions come from the example EEHEMT file in IC-CAP, which begins with the default units for all model parameters. After each measurement, the data is first checked and then the simulator is executed to extract model parameter values.

Table 4.1 provides a list of the routines in the EEHEMT measurement and extraction procedure. Each of these routines is discussed in the sections that follow.

Table 4.1 IC-CAP Routines for the EEHEMT Model.

Preview	*ig_vgs* *id_vgs_at_vdso* *id_vds_vgs*
Source_Resistance	*Yang_Long_Preview* *gate_diode* *Yang_Long_Method*
Cold_FET	*rg_rd*
Package	*Arnold_Golio*
DC-IV	*ig_Is_N* *id_vgs_at_vdso* *id_vgs* *id_vds*
AC_at_Vdso	*Meas_Sparameters* *C11_vgs* *ac_gm_gds*
AC_all	*Meas_Sparameters* *Cgd_vgs_vds* *Qg_vds_vgs* *Tau_Ri_Cds* *ac_gm_gds*
Utilities	*File_Validate*

4.4.1 Device Preview

To ensure that the range of bias voltages and currents for the gate and drain are within the limits needed to make an accurate extraction possible, a preview DC measurement is made to determine these estimates. The preview also helps set limits to protect the transistor from damage. Usually one will start with values within a comfortable range and then adjust until the results are satisfactory. The success of the Preview will affect the rest of the DC and AC measurements to come. Because of the destructive nature of measuring the breakdown voltage of GaAs FETs, for this thesis it is assumed that the user already knows this figure and can enter the value manually. Usually, the initial testing of devices at the fabrication facility

will provide these numbers for a given lot of wafers. The default value is set at 8 volts but the breakdown per conversation with Steve Lardizabal at Raytheon RF Components for this lot of devices is 6 volts [37]. Because of the high In content in the transistor, the maximum voltage attainable without severe oscillation or breakdown is 2 volts. This is due to impact ionization in the channel and is common in InP devices.

Along with input from the user, the model global variables will be decided for the Device Preview measurements. For a list of the model global variables the reader is referred to Appendix D.

The *ig_vgs* measurement uses four gate voltages at zero drain current to measure the gate current density. Using the device periphery, *ig_vgs* will set limits to the gate voltages used in upcoming sections based on the amount of power per unit length of gate width. Measuring *id_vgs_at_vdso* will cover operation from sub-threshold voltages to high current regions. In the IC-CAP manual, the importance of choosing *vdso* is crucial to simplifying the equations for GaAs devices. As shown in Chapter 3, V_{dso} is used to simplify the current equations by allowing any V_{ds} reliance to be withdrawn and only V_{gs} being the dependent variable. A typical value for V_{dso} will be at an operating point in the saturated region of the device [33]. It is noted that dispersion parameters are easier to extract if V_{dso} is chosen correctly. The drain current is measured versus gate voltage at a constant voltage V_{dso} to simplify the current equation and extraction.

The last Preview measurement is *id_vds_vgs*, which is measured drain current at different gate voltages while sweeping V_{ds}. This is the most common DC-IV data for all nonlinear models and can be seen in Figure 4.13. The entire region of the device is measured and model variables set include *VDS_MIN, VDS_MAX, IDS_MAX, and GSMAX.* The routine

id_vds_vgs defines the limitations of the model extraction that sets a minimum and maximum drain voltage. The maximum drain current is set along with a predetermined maximum transconductance.

.

4.4.2 Source Resistance

In the small signal model, the parasitic resistances were obtained using the technique by Yang and Long [36]. The measurement in this section determines the source resistance and gate diode effect of the Schottky contact. The *Yang_Long_Preview* will setup current values within the confines specified in the paper. Both I_d *and* I_g will be measured dependent on V_{gs}. These values will be used in the final *Yang_Long_Method* measurement. Two drain currents with minimal separation are driven with swept values of gate current to measure the differences in V_{gs}. The difference in the gate voltage using the two drain currents will be attributed to the common lead resistance [25] or extrinsic source resistance. In the *Gate_Diode* measurement, V_{gs} is swept to measure values for gate current at V_{ds} = 0.The parameters I_s and N are extracted. These two components are necessary for the source resistance extraction to work properly.

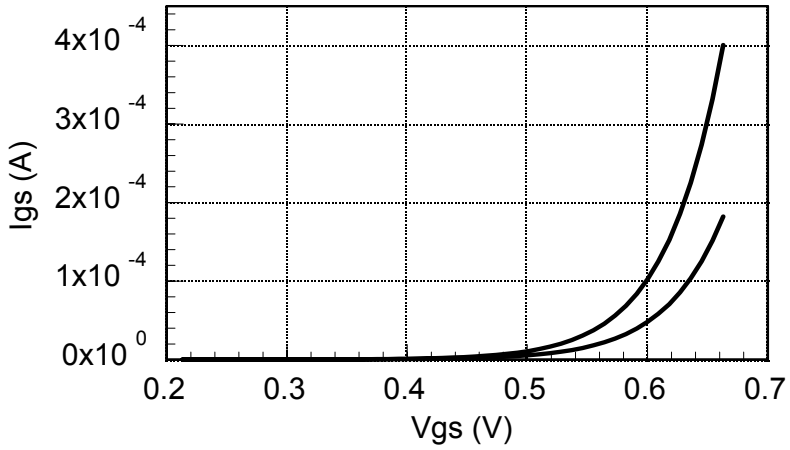

Figure 4.9 *Yang-Long Preview* for I_{gs} to Determine R_g of Raytheon 75 um MHEMT.

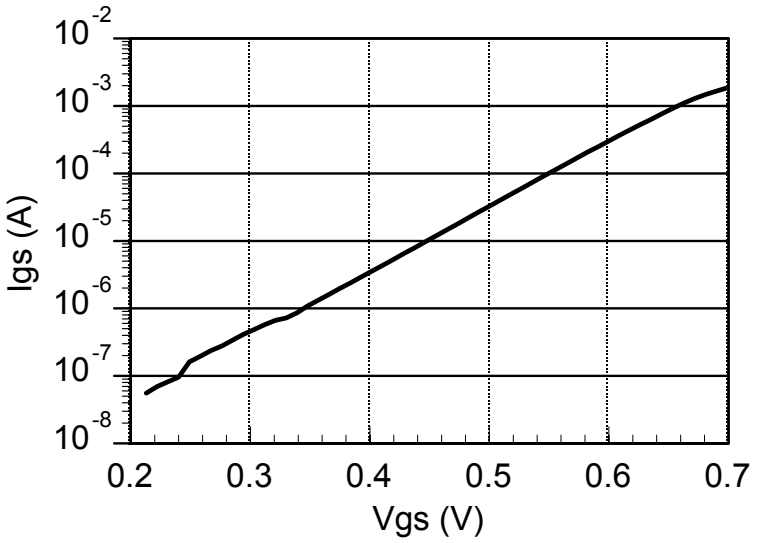

Figure 4.10 *Gate Diode* Measurement of Raytheon 75 um mHEMT.

4.4.3 Parasitics

The rest of the parasitic values are extracted in this set by using cold FET and nominal bias S-parameters. R_g and R_d are extracted from the cold FET S-parameters in the same fashion as in the small signal model but the inductances are formulated by the method illustrated by Arnold and Golio et al [18]. The cold FET *rg_rd* measurement is different than the Curtice method that calls for both V_{ds} and V_{gs} equal to zero. The gate-drain and gate-source zones are effectively forward biased in this case. The extraction for R_s and R_g is similar to that by Dambrine and Cappy [20] but the IC-CAP manual notes that it is not an exact footpath of this work [25].

The inductance values are extracted by RF characterization of the device in its operational range and knowledge of the parasitic resistances. The S-parameters are measured at a nominal V_{ds} at values of V_{gs} that range form pinchoff to I_{dss} in the *Arnold_Golio Package Parasitics* measurement [18]. The large variations of intrinsic values over several gate voltages increase the impression of the parasitics since they are independent of bias and the

intrinsic elements are not. The extrinsic inductances become easy to extract with numerous S-parameter measurements from pinch-off to drain current saturation.

4.4.4 DC Parameters

In the DC-IV parameter measurements, four different procedures are used to obtain enough information to extract all DC parameters. Using the global model variables defined in the Preview and parasitic resistance measurements, the IC-CAP setup for each section is straightforward and can usually be activated immediately without reentering device limits. As in the *gate_diode* measurement, the *Ig_Is_N* measurement measures gate current as a function of gate voltage at zero V_{ds}. At this point it will calculate the final values for the gate diode attributes. An example is shown in Figure 4.10. The *id_vgs_at_vdso* measurement is the same as in the Preview section. V_{to} and initial values for V_{go} and V_{delt} are some of the major extractions in this setup. Figure 4.14 displays a plot of g_m at V_{dso} as a function of swept gate voltage. Figure 4.11 is a measurement of drain current at V_{dso} as a function of gate voltage. Along with the DC parameters the g_m compression characteristics are also modeled. These are attributed to the values of g_m as a function of gate voltage with drain voltage constant at V_{dso}.

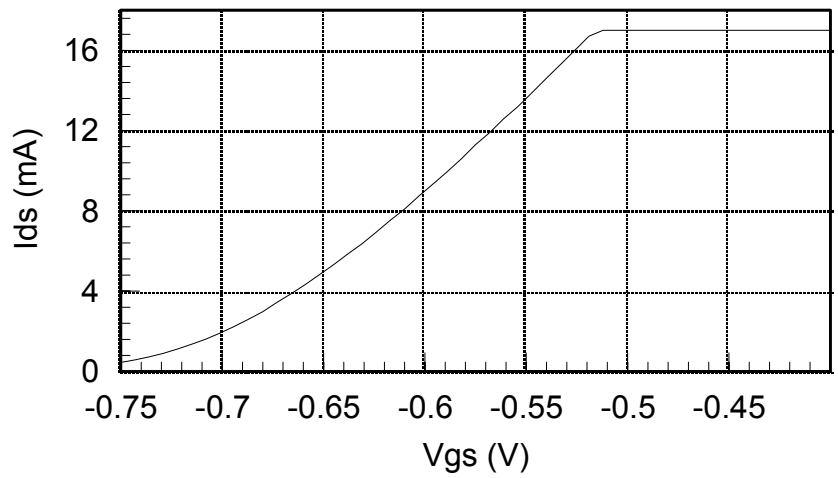

Figure 4.11 *Id_Vgs_at_Vdso* Measurement of Raytheon 75 um mHEMT.

In the *id_vgs* setup, drain current is monitored as a function of gate voltage. This will help initialize an assessment for *gamma,* which controls the threshold parameter as a function of V_{ds}. Figure 4.12 demonstrates how the plots will look at the end. Here V_{gs} is swept instead of V_{ds} as will be seen next. The last measurement is the standard forward DC-IV format as shown in Figure 4.13. This graph displays the result of the subsequent sessions. All the final values are extracted which include *kappa, Vsat, Peff, Vdelt, gamma,* and *Gmmax.*

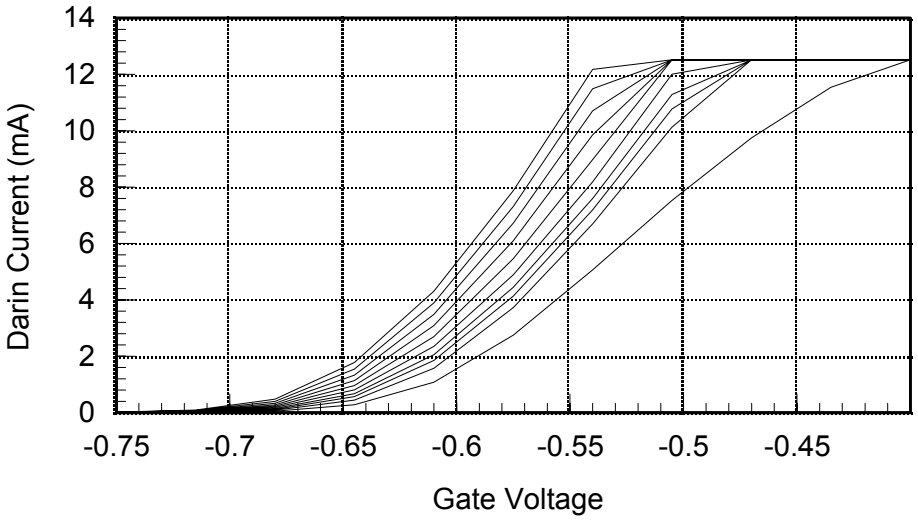

Figure 4.12 *Idvgs* Measurement of Raytheon 75 um mHEMT.

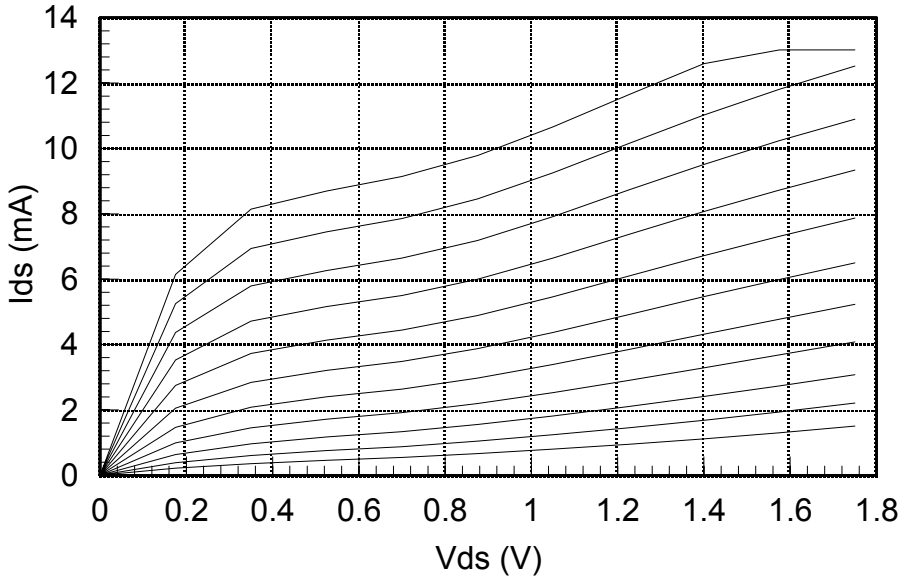

Figure 4.13 DC-IV Measurement of Raytheon 75 um mHEMT.

4.4.5 AC Charge and Dispersion Parameters

Two sets of S-parameter data are needed to complete the AC model. Both sets will be measuring swept I_{ds} at steps of V_{gs} but one set will require only a single drain voltage V_{dso}. The reason for this is the same as before. At V_{dso}, the equations simplify and some of the model parameters will be easier to define in this process. Gate charge parameters, C_{11o}, C_{11th}, V_{infl}, and $Delt_{gs}$ will be extracted first from the V_{dso} biased s-parameters. To see how the extraction takes place the reader is referred to section 3.4. Initial values for the dispersion characteristics *gmmaxac, gammaac, kappaac, peffac,* and *vtoac* are also commenced.

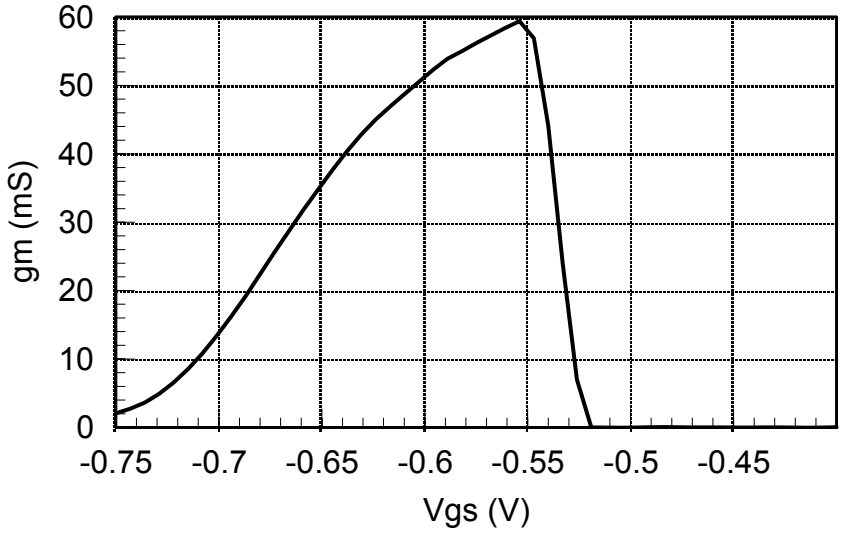

Figure 4.14 g_m Extraction at V_{dso} of Raytheon 75 um mHEMT.

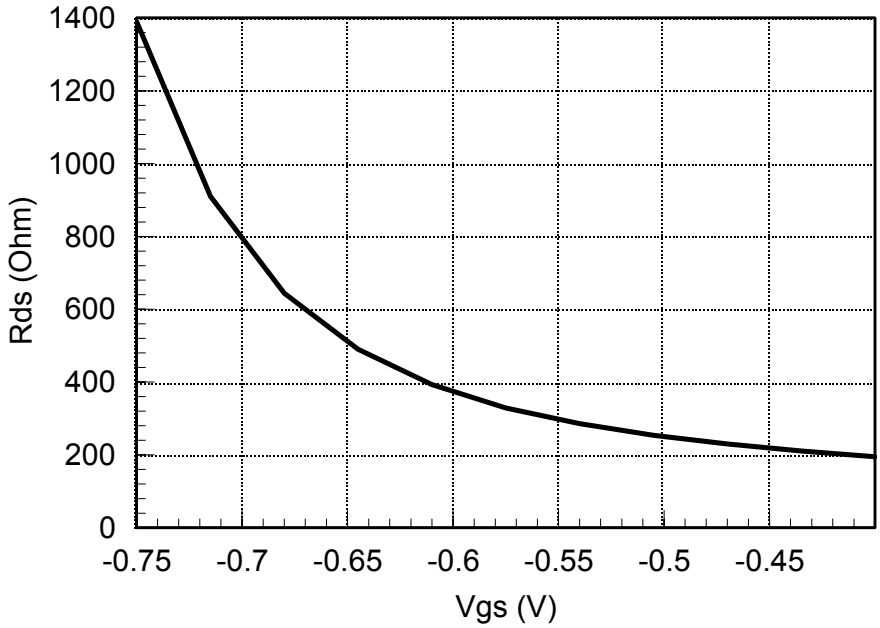

Figure 4.15 R_{ds} Extraction at V_{dso} of Raytheon 75 um mHEMT.

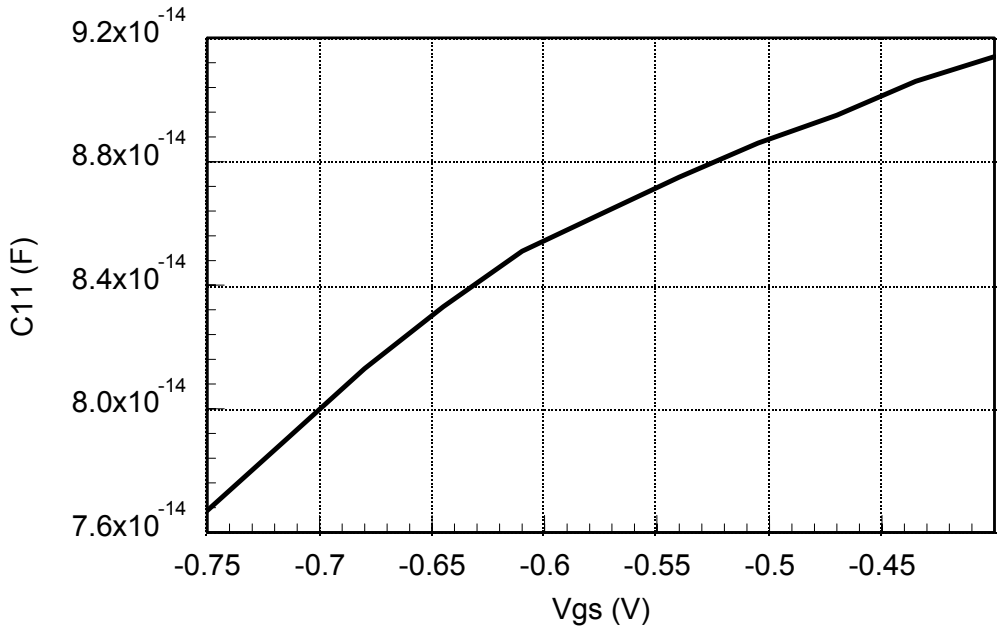

Figure 4.16 C_{11} Measurement at V_{dso} of Raytheon 75 um mHEMT.

For the output charge parameters, C_{21} and C_{22} capacitances are used to fit C_{dso} and *Tau.* The values for $Delt_{ds}$, *Lambda,* and C_{12sat} are also extracted in this procedure. Even though R_i and *Tau* are independent of each other, they are fitted together. R_i is associated with the gate charge while *Tau* is related to the delay of S_{21}. In this model though R_i is split between the channel resistance of gate-source and gate-drain and termed R_{is} and R_{id}. [In Figure 3.6 of the previous chapter, the equivalent circuit of the EEHEMT model is displayed]. Q_{gy} and Q_{gc} are the input charge capacitances and C_{dso} is the output dispersion capacitance.

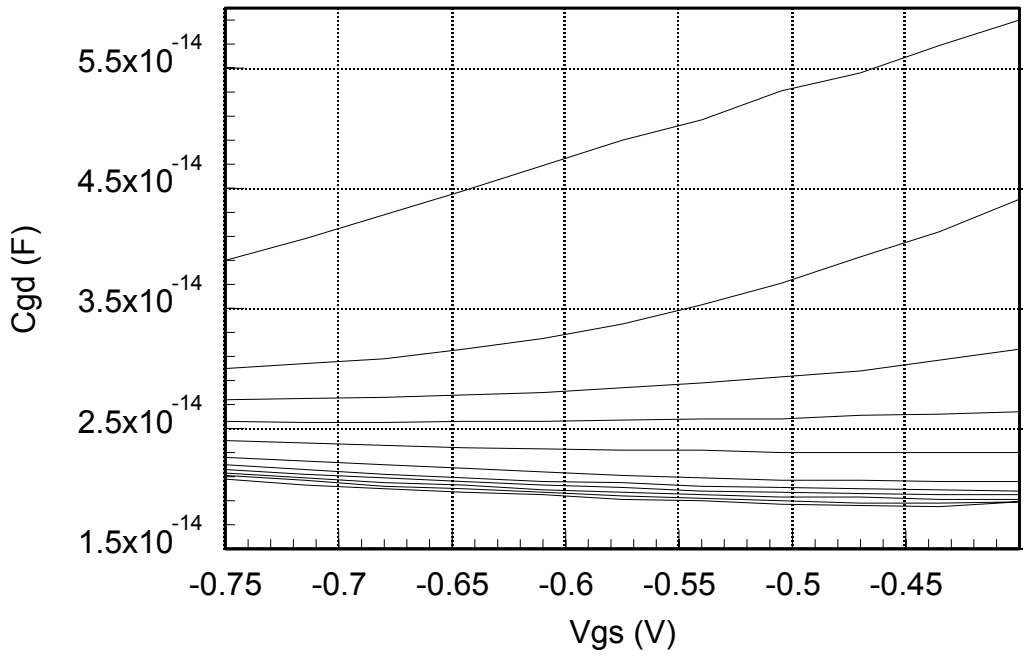

Figure 4.17 C_{gd} Extraction of Raytheon 75 um mHEMT Sweeping V_{gs} Versus Several Drain Voltages.

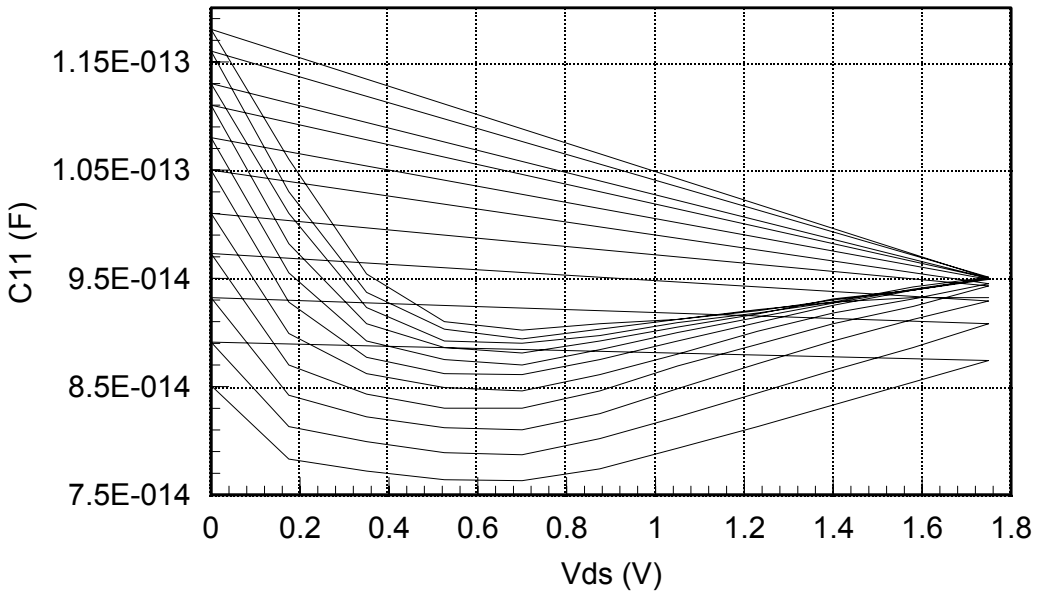

Figure 4.18 C_{11} Measured of Raytheon 75 um mHEMT Sweeping V_{ds} Versus Several Gate Voltages.

.

The causes for dispersion effects illustrated in Chapter 3 due to high frequency products that change g_m and G_{ds} necessitate further extraction of parameters that will

provide better accuracy. In this optimization, G_{ds} is included in the parameter R_{db}. Other values finalized are C_{bs}, *Gmmaxac, Vdeltac, Vtoac, Gammaac,* and *Kappaac.* As a reassurance that the modeling is accurate, a sample measurement is taken at a given bias and compared to the simulation.

4.5 Chapter Summary

In this chapter, the measurement and modeling techniques have been outlined to present the methods for which this project was constructed. The small-signal modeling using SPECIAL provided good results as can be seen in Chapter 5 and was simple to use given a modest learning curve. The noise modeling required great effort on the part of the author to fully understand the theory and extraction involved in generating noise sources in the small-signal model from the noise parameters. Knowledge of the effects of how T_g and T_d alter the slope and magnitude of F_{min}, adjust Γ_{opt}, and change due to ambient temperature are required before initiating the noise modeling. Several technical papers and help from previous work by Steve Lardizabal helped tremendously with this effort.

The nonlinear model measurement and extraction followed the guidelines of Agilent's EEHEMT model procedure in the IC-CAP manuals. After each measurement step the simulated parameters were optimized resulting in a virtually complete model. In Chapter 5, the comparison of the nonlinear model s-parameters versus the small-signal model show the ability of the IC-CAP system versus a bias dependent model extraction.

CHAPTER 5

MODEL VERIFICATION

In previous chapters, the models and extraction techniques for small-signal and noise, as well as large-signal models, were discussed. In this chapter, the ability of these models to accurately predict the performance of the chosen mHEMT device is the focus. For the small signal model, the capability of the table look-up model will be explored. Considering the fact that interpolation is used between bias and temperature data points, measurements will be compared to the model at bias and temperature conditions not previously used for the extraction process. The large-signal model will be compared to several nonlinear measurements that are of value to power amplifier designers.

5.1 Small Signal Model Verification

In this section, the data that will be compared corresponds to a specific bias and temperature that has been used to extract a model. In section 5.3 the interpolation of the model to measured data at temperatures other than those used for the model extraction will be examined. For s-parameters, the fits between measured and model data were generally excellent and required little input from the user to better match the measured data. In most cases the error percentage for the real and imaginary parts of each s-parameter never exceeded three percent. Only in cases of high drain current were there problems with fitting, which were usually related to a negative delay or *Tau.*

To correct this, a value for *Tau* was selected based on the previous extraction at a lower drain current. The extraction was executed again with *Tau* fixed and the necessary change in the other model parameters was negligible.

5.1.1 ECP Trends

The general trend of the intrinsic equivalent circuit parameters (ECPs) is to either rise or descend in relation to bias. For the intrinsic resistance values, the trend is to decrease as bias increases. *Tau*, g_m, and C_{gs} usually increase as bias current climbs. C_{ds} is tends to be relatively constant. The trends of the ECPs in this work are illustrated further in Figures 5.1 through 5.3. These plots were generated using the extraction methods described in Chapter 2. A plot of the parameters R_i and R_{ds} are shown in Figures 5.1 and 5.2 from 0.5 to 1.25 volts V_{ds}. Figure 5.3 plots the transconductance, gm, from 0.5 to 1.25 volts V_{ds}. All values correspond to room temperature operation.

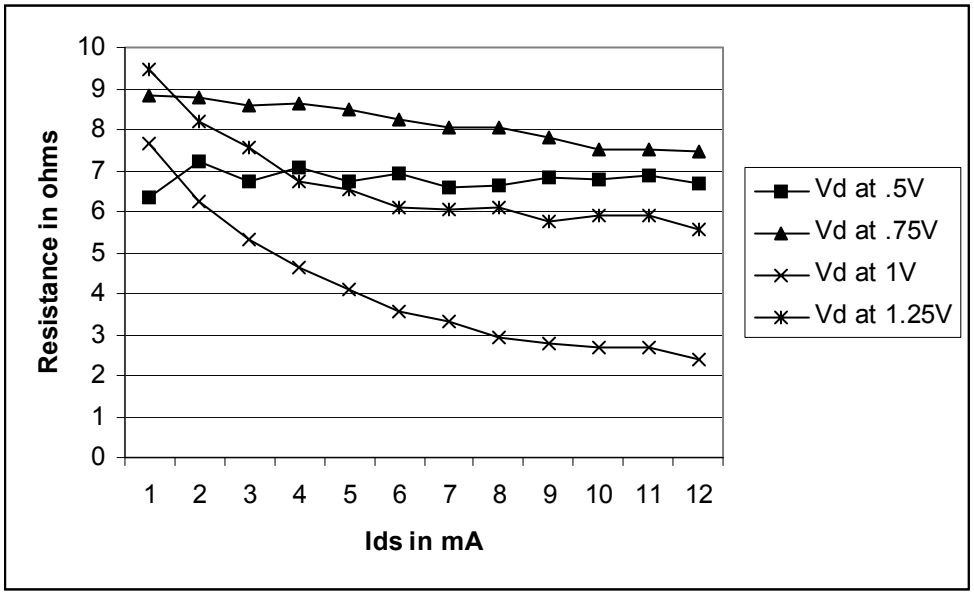

Figure 5.1 Plot of Parameter R_i at 0.5 to 1.25 volts V_{ds} and 1-12 mA I_{ds} for a Raytheon 75 um mHEMT.

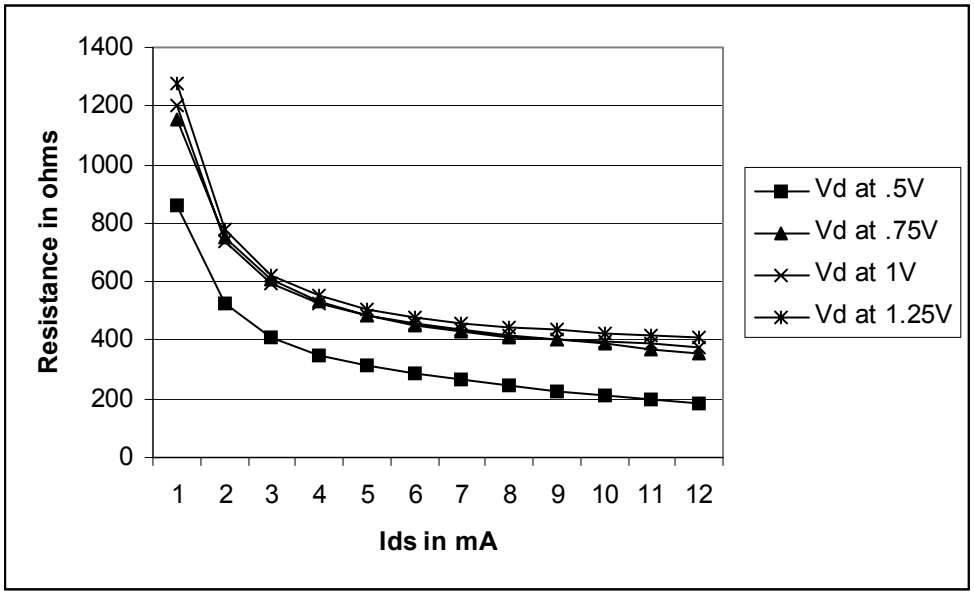

Figure 5.2 Plot of Parameter R_{ds} at 0.5 to 1.25 volts V_{ds} and 1-12 mA I_{ds} for a Raytheon 75 um mHEMT.

In this study, the trend for R_i is a decreasing value as drain current rises. From Figure 5.1, R_i, also known as the gate-to-source resistance R_{gs}, does not necessarily follow a perceived pattern. At V_{ds} equal to 1 volt, the behavior of R_i changes. An explanation for this is that R_i changed due to the extraction of C_{gs} and C_{gd} at the first bias point (or 1ma for 1 volt V_{ds}). Since the parameters were extracted sequentially versus drain current, trends in C_{gs}, C_{gd}, R_i, etc. would continue along a similar path. In Figure 5.2, R_{ds} is shown to deviate noticeably at a drain voltage of 0.5 volts compared to other voltages. This is due to the voltage being near the knee region of the DC-IV curves where R_{ds} becomes very small. In Section 5.21, the effects of the extracted intrinsic resistances R_i and R_{ds} will be discussed with respect to their affect on noise modeling.

Another trend of interest is the behavior of the slope of g_m as drain current rises. Unlike MESFETs, HEMTs show compression in transconductance as V_{gs} approaches

zero. For the small-signal model, the highest value for drain current is 12 mA, which is still in the device's range of normal operation. This drain current was considered sufficiently high for the mHEMT's normal operation for low noise amplifier (LNA) design, which is this model's intended purpose. At 12 mA drain current, the highest value for g_m should be observed, however in the large signal model, the transconductance compression should be modeled and validated. The effect of V_{ds} on the transconductance is minimal. In Figure 5.3, g_m is plotted for all measured values of V_{ds} from 0.5 to 1.25 volts at 0.25 increments.

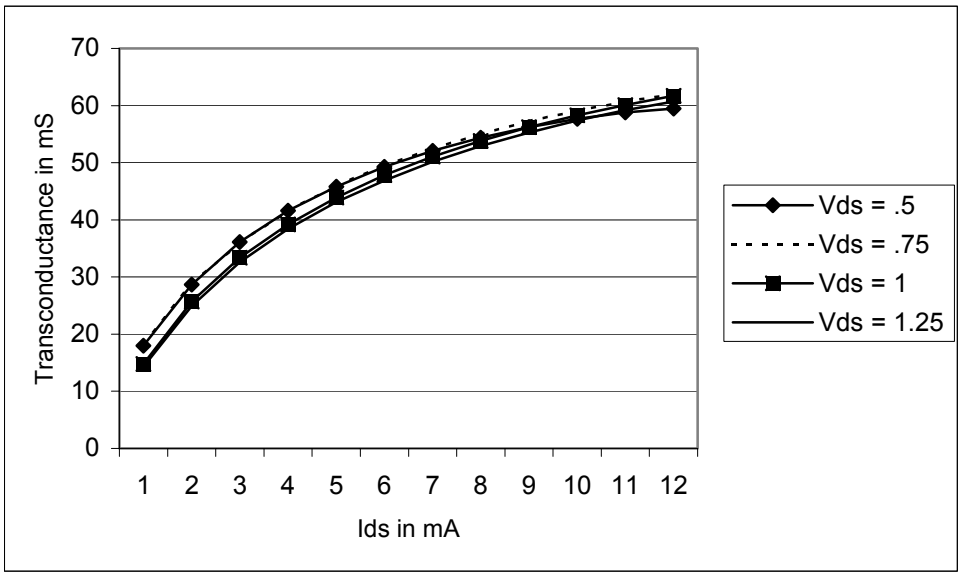

Figure 5.3 Plot of Parameter g_m at 0.5 to 1.25 volts V_{ds} and 1-12 mA I_{ds} for a Raytheon 75 um mHEMT.

In this figure, *gm* is shown not to change much with drain voltage. Thus, a conclusion can be drawn, that the transconductance is dependent primarily on the drain current.

A tabulation of the other extracted parameters for the model at 25 ^{o}C is given in Appendix C.

5.1.2 S-parameter Fits

For this project, the s-parameter fitting required the least labor to achieve a good model. During the fitting process, the methods outlined in Chapter 2 were tested, verified, and improved upon. In the subsequent figures, the measured S-parameters are compared to the modeled s-parameters at bias currents 1, 4, 8 , and 12 ma. These biases were selected to represent the full spectrum of modeling from 1 to 12 mA of drain current.

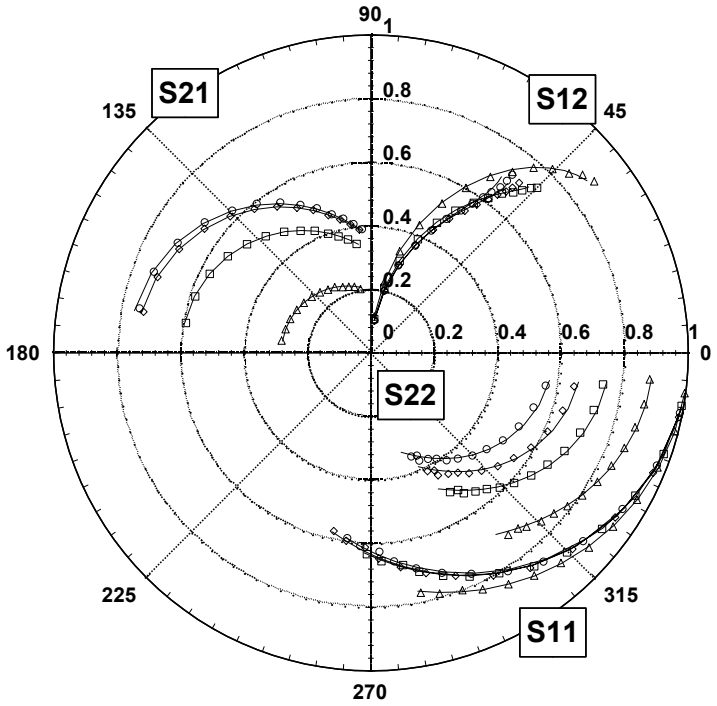

Figure 5.4 Comparison at 25 ^{o}C of Measured and Modeled S-parameters at V_{ds} of .5 Volts. Measured data is at 1ma (triangles), 4ma (squares), 8ma (diamonds), and 12ma (circles). Modeled data are shown as solid lines.

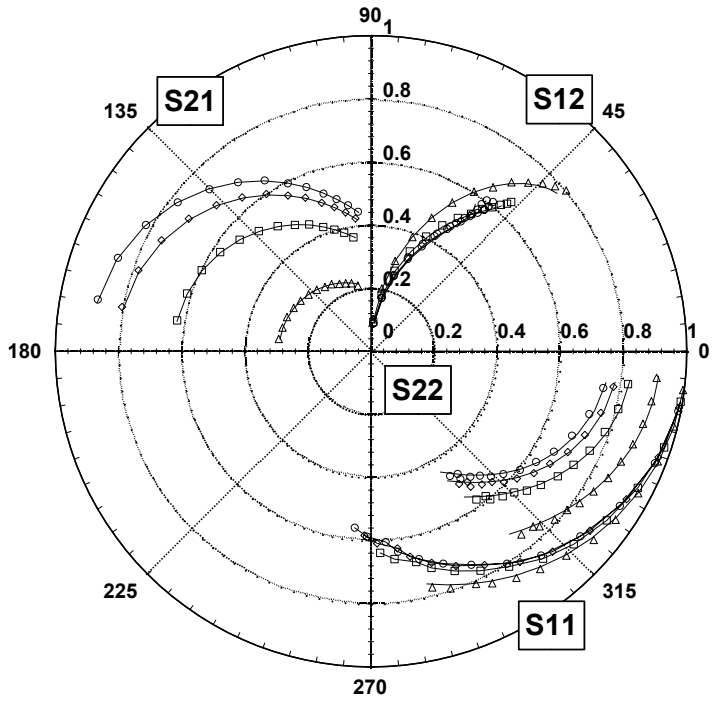

Figure 5.5 Comparison at 25 °C of Measured and Modeled S-parameters at V_{ds} of .75 Volts. Measured data is at 1ma (triangles), 4ma (squares), 8ma (diamonds), and 12ma (circles). Modeled data are shown as solid lines.

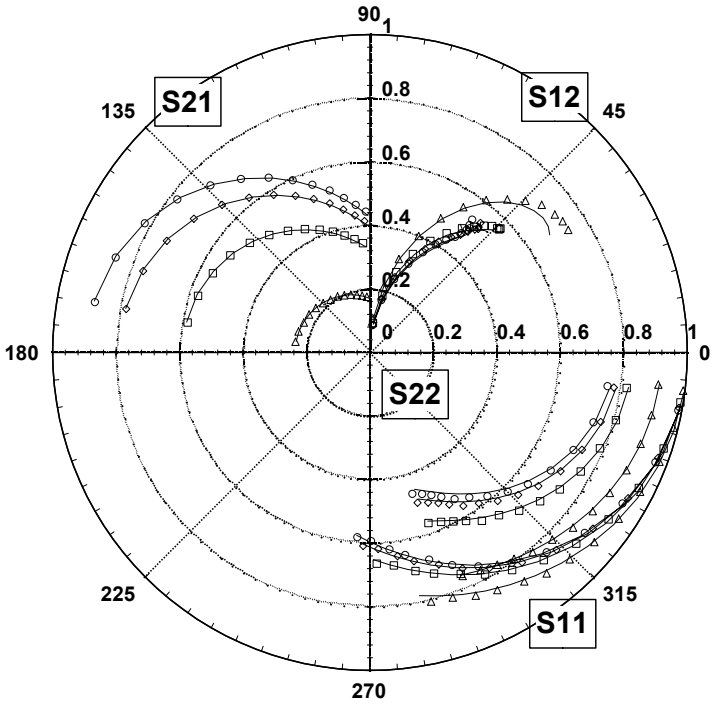

Figure 5.6 Comparison at 25 °C of Measured and Modeled S-parameters at V_{ds} of 1 Volt. Measured data is at 1ma (triangles), 4ma (squares), 8ma (diamonds), and 12ma (circles). Modeled data are shown as solid lines.

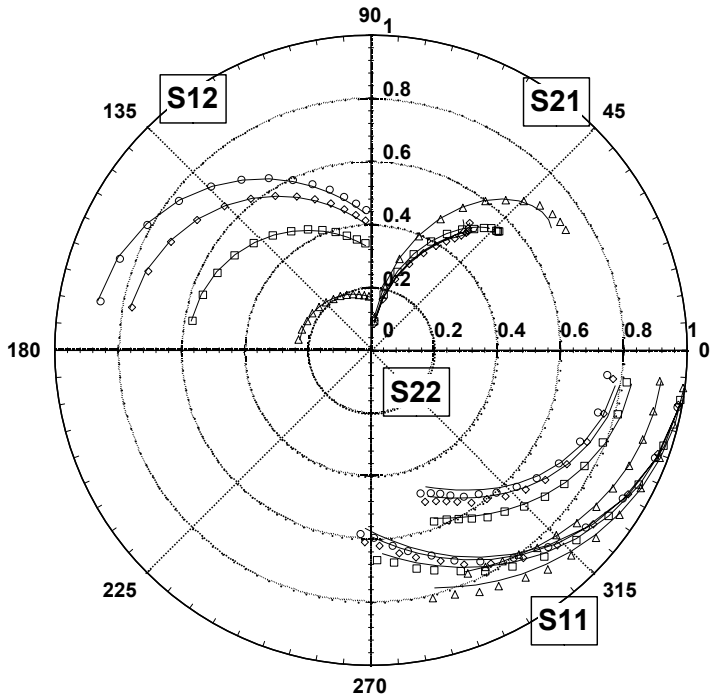

Figure 5.7 Comparison at 25 ^{o}C of Measured and Modeled S-parameters at V_{ds} of 1.25 Volt. Measured data is at 1ma (triangles), 4ma (squares), 8ma (diamonds), and 12ma (circles). Modeled data are shown as solid lines.

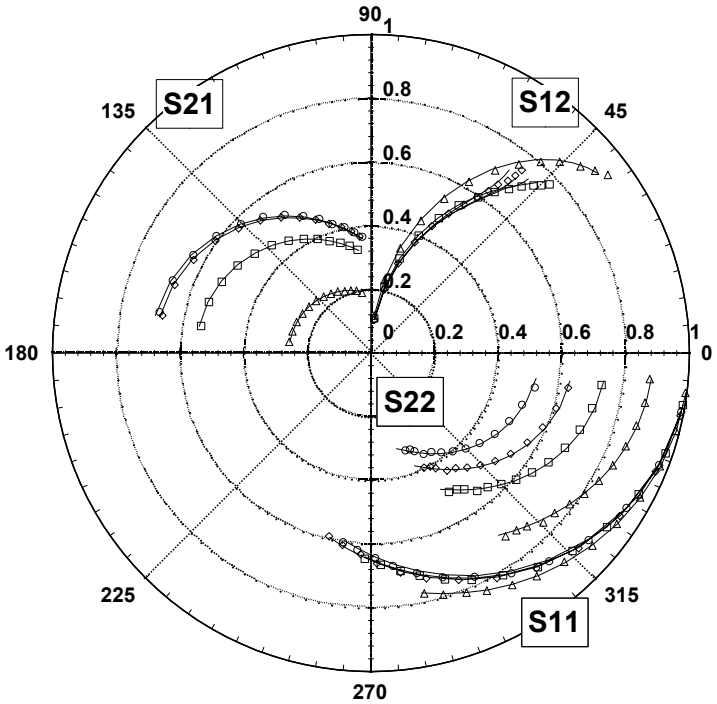

Figure 5.8 Comparison at 85 ^{o}C of Measured and Modeled S-parameters at V_{ds} of .5 Volt. Measured data is at 1ma (triangles), 4ma (squares), 8ma (diamonds), and 12ma (circles). Modeled data are shown as solid lines.

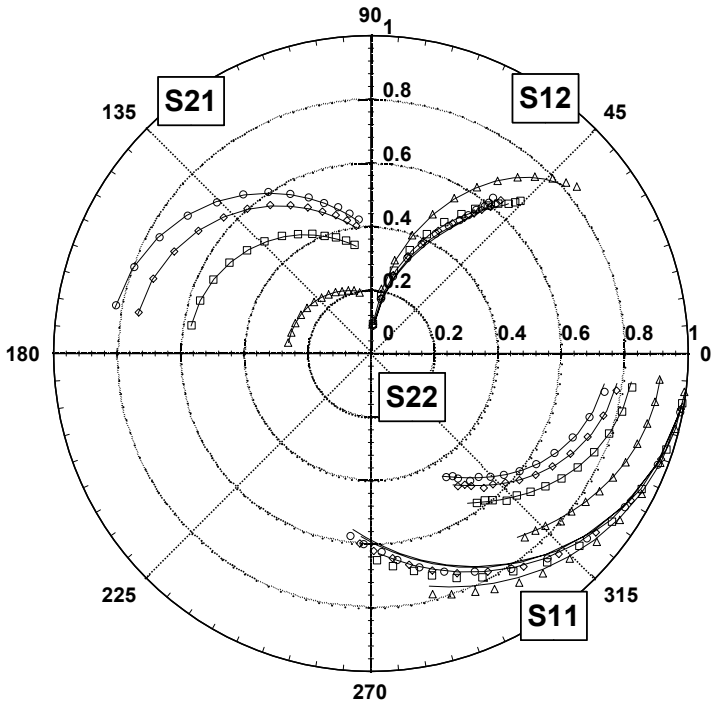

Figure 5.9 Comparison at 85 °C of Measured and Modeled S-parameters at V_{ds} of .75 Volt. Measured data is at 1ma (triangles), 4ma (squares), 8ma (diamonds), and 12ma (circles). Modeled data are shown as solid lines.

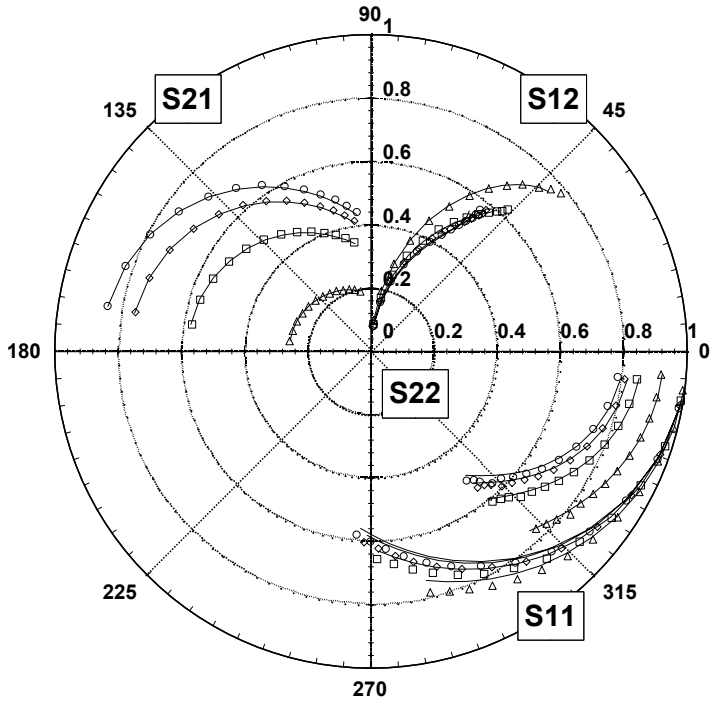

Figure 5.10 Comparison at 85 °C of Measured and Modeled S-parameters at V_{ds} of 1 Volt. Measured data is at 1ma (triangles), 4ma (squares), 8ma (diamonds), and 12ma (circles). Modeled data are shown as solid lines.

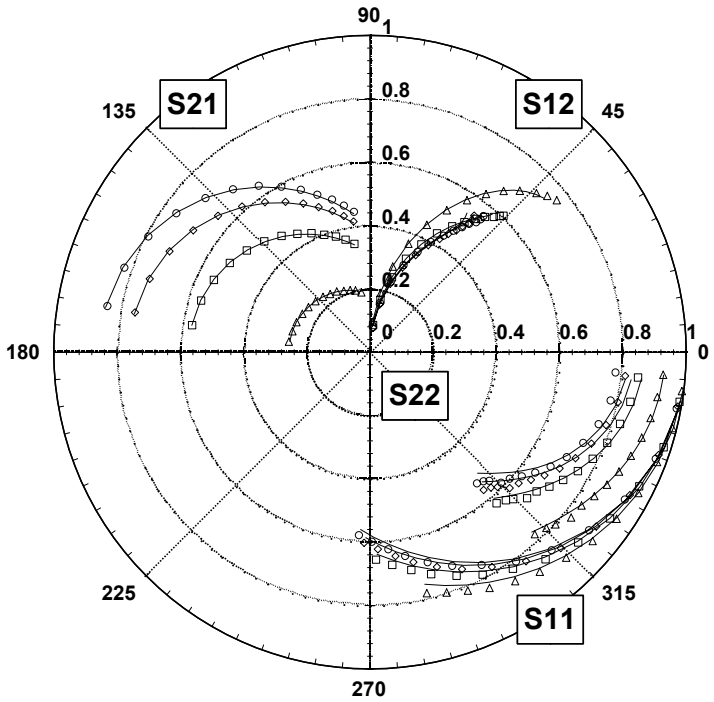

Figure 5.11 Comparison at 85 ^{o}C of Measured and Modeled S-parameters at V_{ds} of 1.25 Volt Measured data is at 1ma (triangles), 4ma (squares), 8ma (diamonds), and 12ma (circles). Modeled data are shown as solid lines.

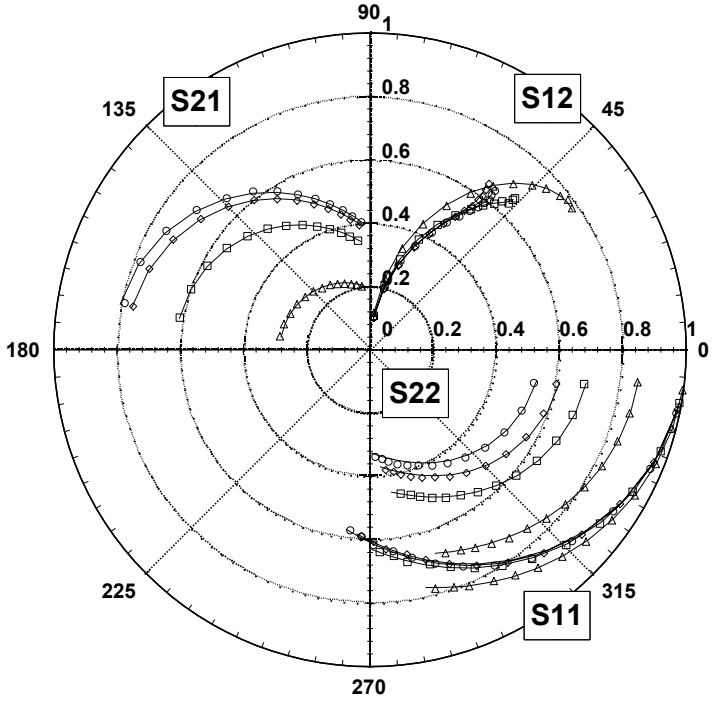

Figure 5.12 Comparison at -55 ^{o}C of Measured and Modeled S-parameters at V_{ds} of .5 Volt. Measured data is at 1ma (triangles), 4ma (squares), 8ma (diamonds), and 12ma (circles). Modeled data are shown as solid lines.

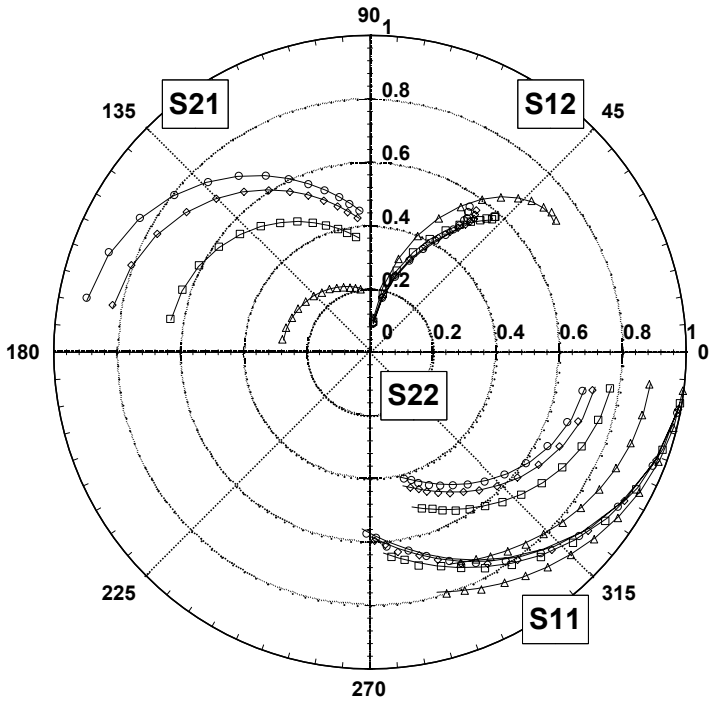

Figure 5.13 Comparison at -55 ^{o}C of Measured and Modeled S-parameters at V_{ds} of .75 Volt. Measured data is at 1ma (triangles), 4ma (squares), 8ma (diamonds), and 12ma (circles). Modeled data are shown as solid lines.

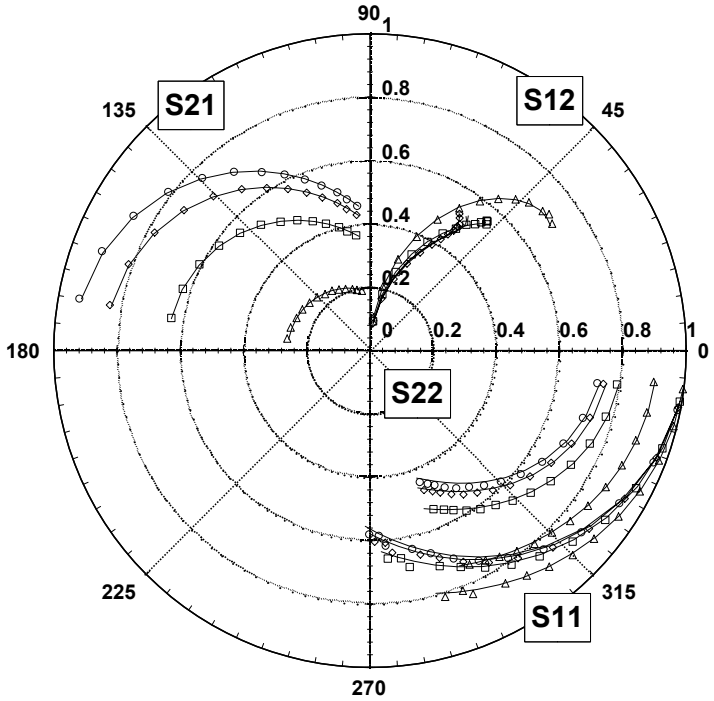

Figure 5.14 Comparison at –55 ^{o}C of Measured and Modeled S-parameters at V_{ds} of 1 Volt. Measured data is at 1ma (triangles), 4ma (squares), 8ma (diamonds), and 12ma (circles). Modeled data are shown as solid lines.

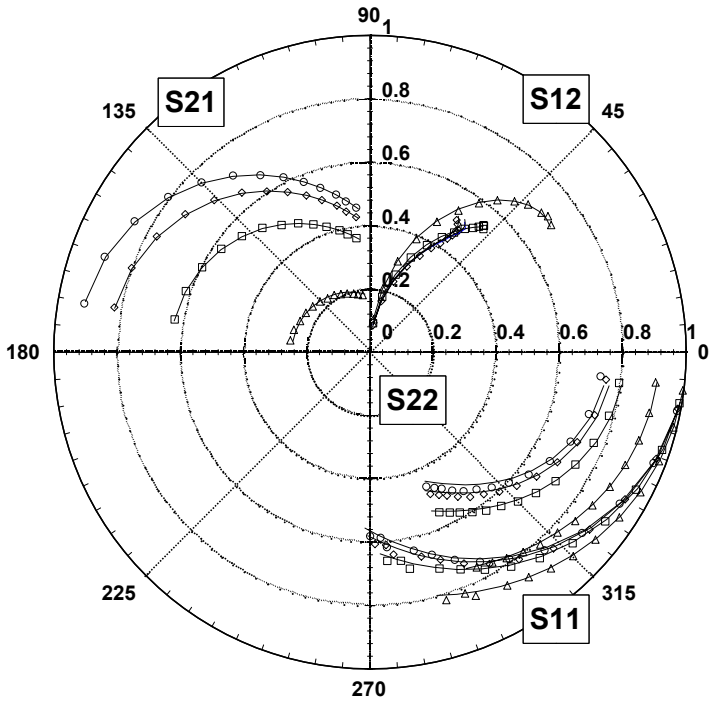

Figure 5.15 Comparison at -55 ^{o}C of Measured and Modeled S-parameters at V_{ds} of 1.25 Volt. Measured data is at 1ma (triangles), 4ma (squares), 8ma (diamonds), and 12ma (circles). Modeled data are shown as solid lines.

5.2 Noise Model Verification

The results for the noise generators, T_g and T_d, seem to deviate from the norm for these particular devices because of the low noise values measured. In most cases, T_g is set at room temperature and T_d is calculated, otherwise, the use of a two-term extraction for both T_g and T_d often leads to a T_g higher than ambient temperature. Particularly with the low noise mHEMT device, the accuracy of the measurement must be carefully considered. If the measured value for F_{min} is 0.15 or 0.25 dB, the user must question the data's reliability when given the minimum instrument accuracy or calibration on the order of +/- .2 dB [38]. If considerable care is not taken, the measurement outcome often shows a negative F_{min}. Smoothing is incorporated into the model to account for measurement variations and to follow the trend of the data over the frequency range.

Half of the data used for modeling was raw noise data, and the other half was smoothed on the order of two polynomials.

In figures 5.16 to 5.27, the noise models are compared to measured data at 1, 4, 8, and 12mA. In this chapter, only one drain voltage is shown at each temperature. The parameter Γ_{opt} has been split into an un-normalized impedance represented by a real (R_{opt}) and imaginary (X_{opt}) value. F_{min} is represented in dB and r_n is the normalized noise resistance.

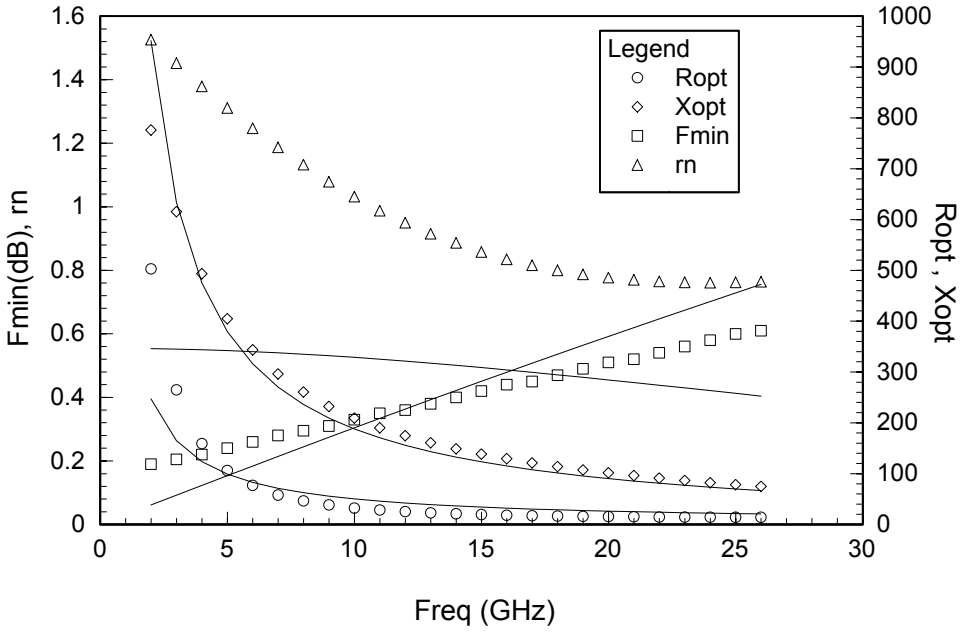

Figure 5.16 Noise Parameter Comparison of Measured versus Modeled at V_{ds}=1, I_{ds}=1ma and 25°C. Measurements are indicated by markers, modeled data are shown as solid lines.

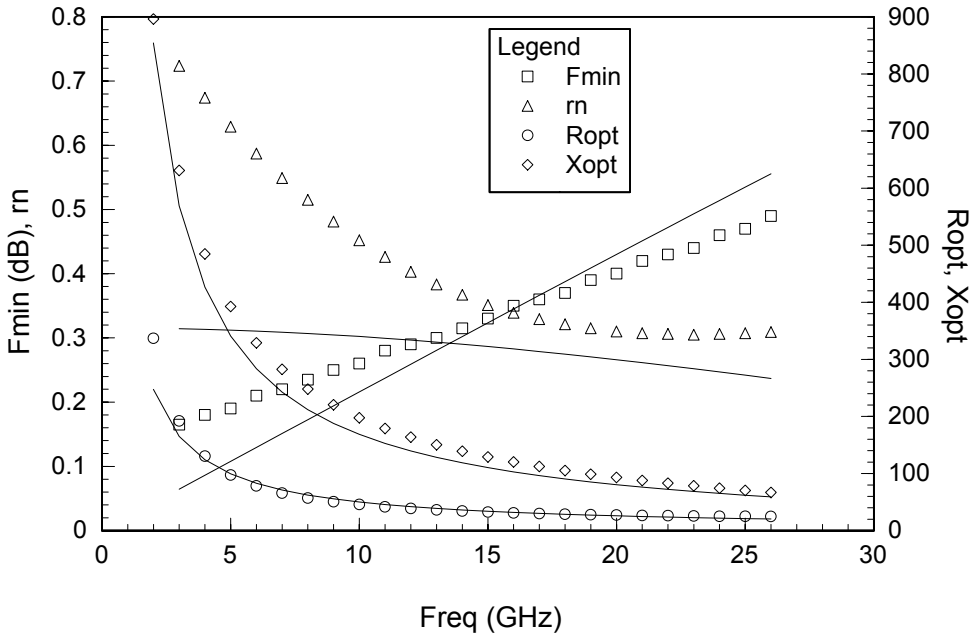

Figure 5.17 Noise Parameter Comparison of Measured versus Modeled at V_{ds} =1, I_{ds} =4ma and 25°C. Measurements are indicated by markers, modeled data are shown as solid lines.

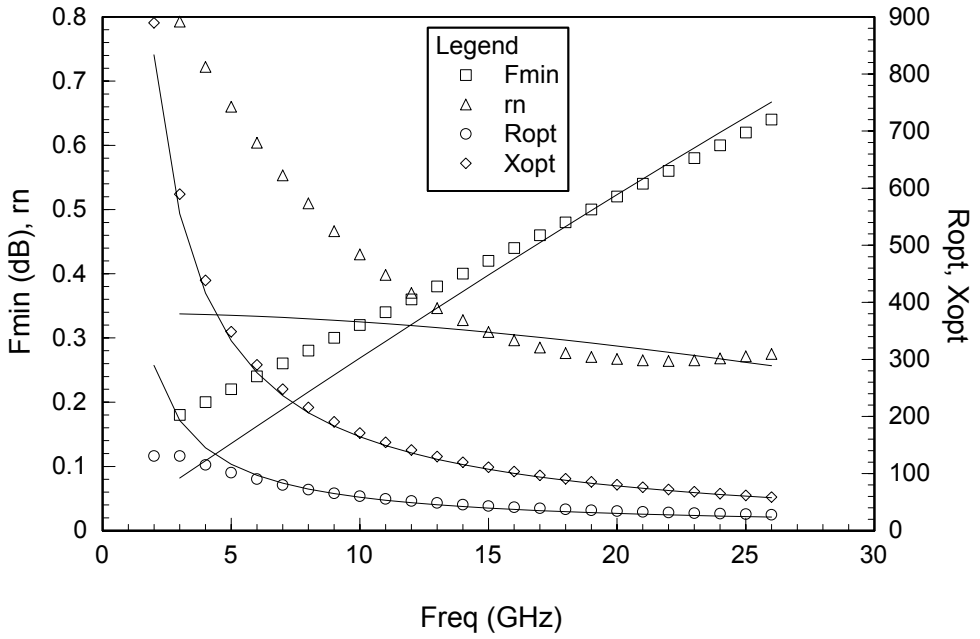

Figure 5.18 Noise Parameter Comparison of Measured versus Modeled at V_{ds} =1, I_{ds} =8ma and 25°C. Measurements are indicated by markers, modeled data are shown as solid lines.

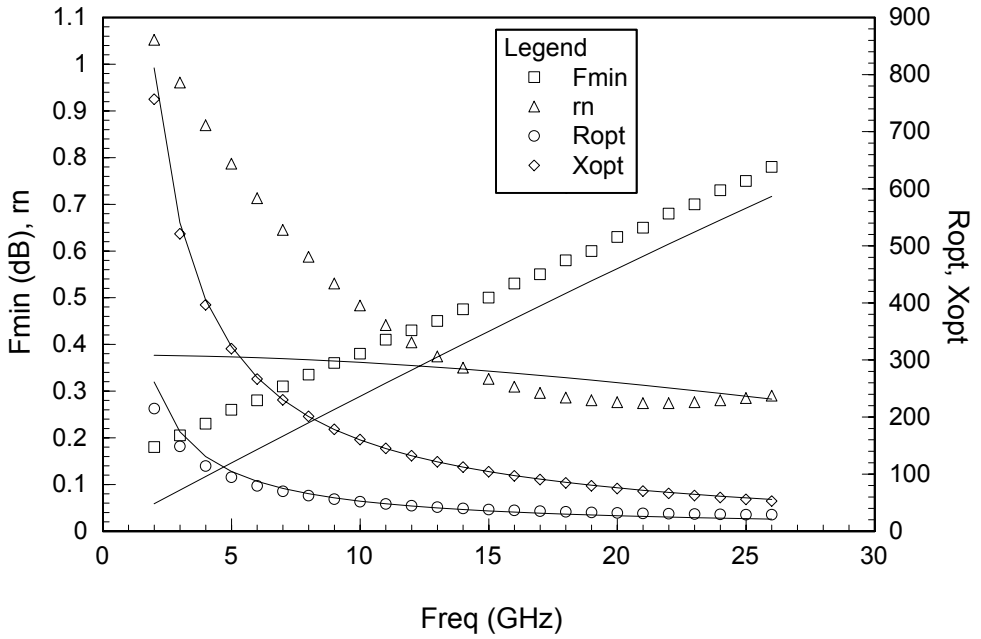

Figure 5.19 Noise Parameter Comparison of Measured versus Modeled at V_{ds} =1, I_{ds} =12ma and 25°C. Measurements are indicated by markers, modeled data are shown as solid lines.

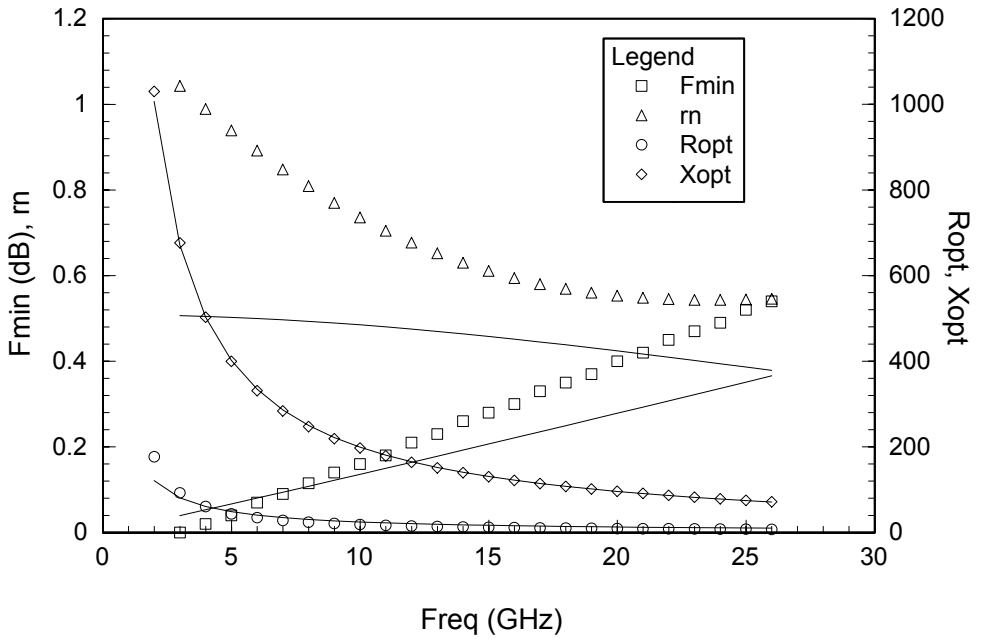

Figure 5.20 Noise Parameter Comparison of Measured versus Modeled at V_{ds} =1, I_{ds} =1ma and -55°C. Measurements are indicated by markers, modeled data are shown as solid lines.

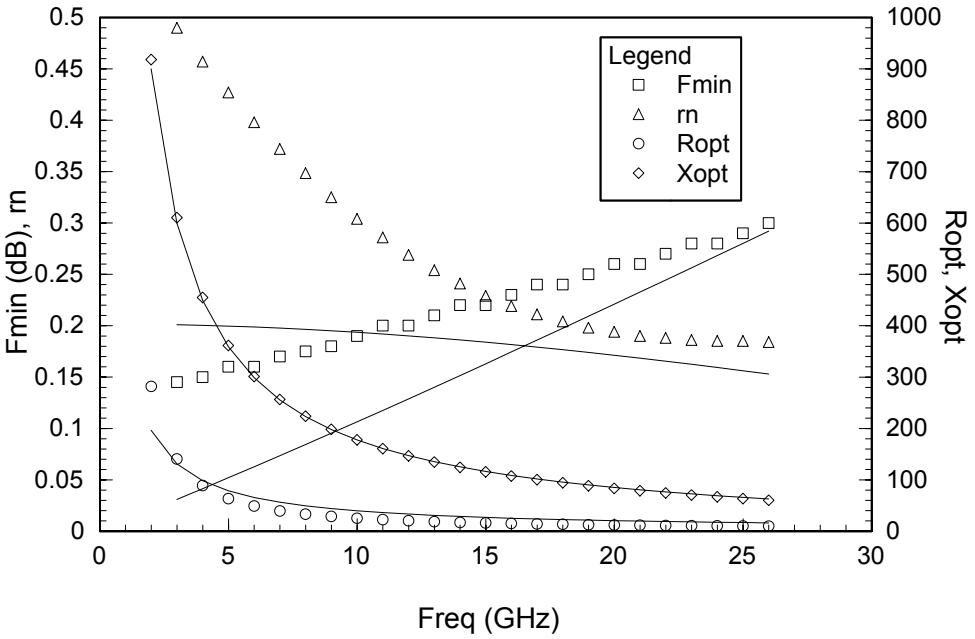

Figure 5.21 Noise Parameter Comparison of Measured versus Modeled at V_{ds} =1, I_{ds} =4ma and -55°C. Measurements are indicated by markers, modeled data are shown as solid lines.

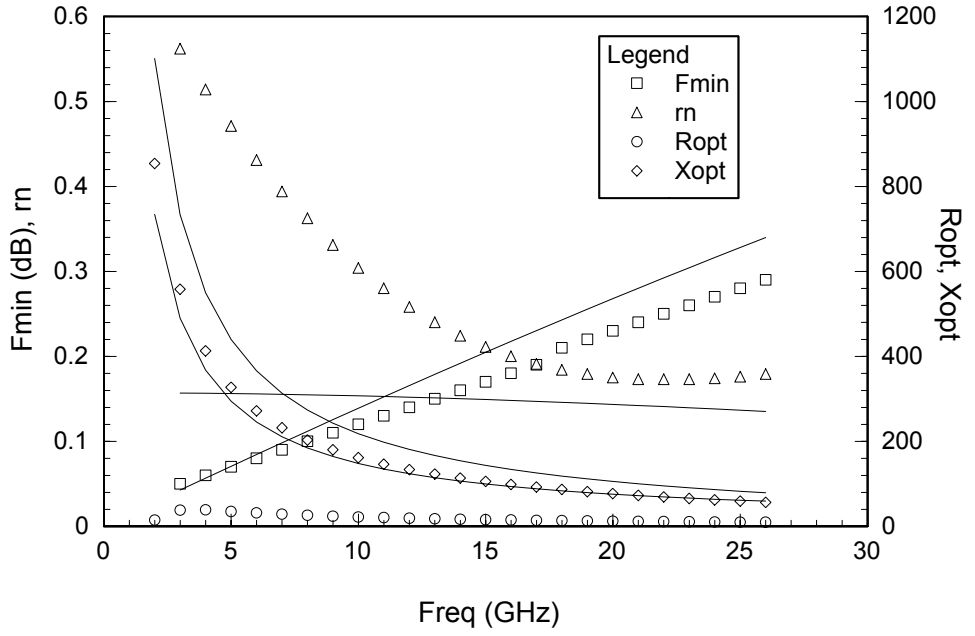

Figure 5.22 Noise Parameter Comparison of Measured versus Modeled at V_{ds} =1, I_{ds} =8ma and -55°C. Measurements indicated by markers, modeled data are shown as solid lines.

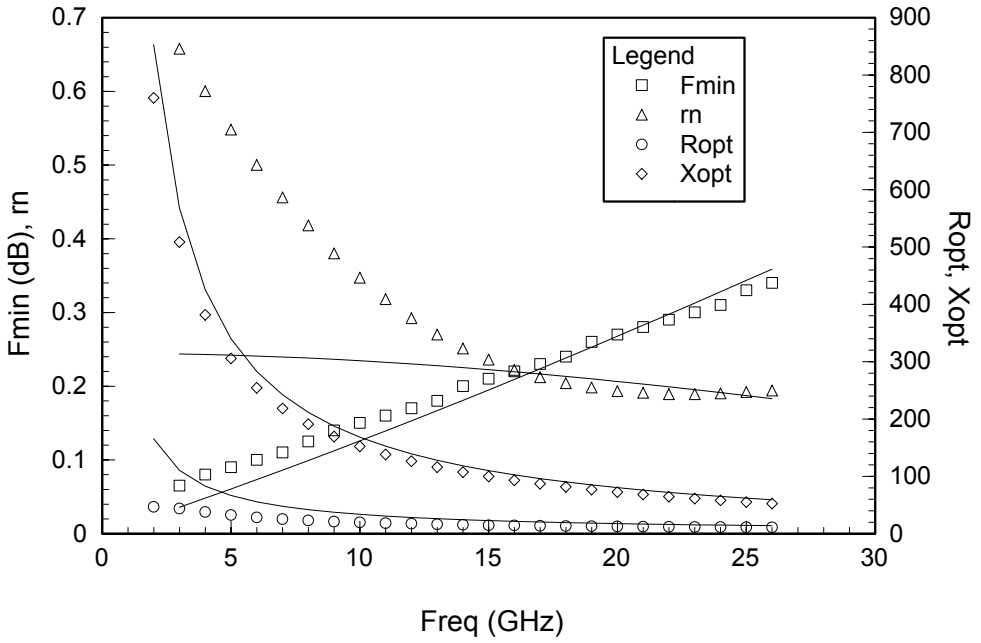

Figure 5.23 Noise Parameter Comparison of Measured versus Modeled at V_{ds} =1, I_{ds} =12ma and -55°C. Measurements are indicated by markers, modeled data are shown as solid lines.

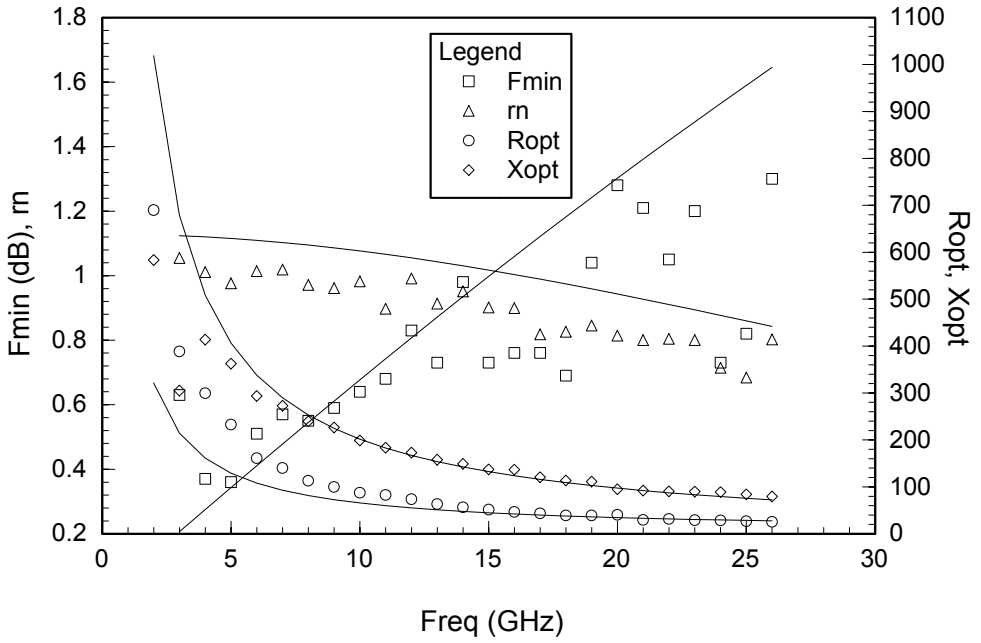

Figure 5.24 Noise Parameter Comparison of Measured versus Modeled at V_{ds} =1, I_{ds} =1ma and 85°C. Measurements are indicated by markers, modeled data are shown as solid lines.

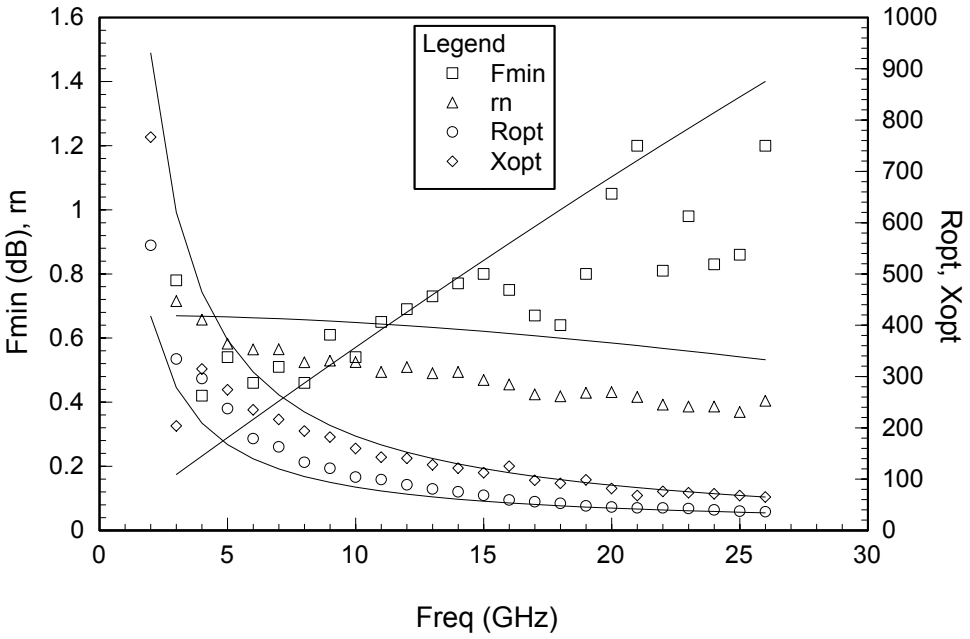

Figure 5.25 Noise Parameter Comparison of Measured versus Modeled at V_{ds} =1, I_{ds} =4ma and 85°C. Measurements are indicated by markers, modeled data are shown as solid lines.

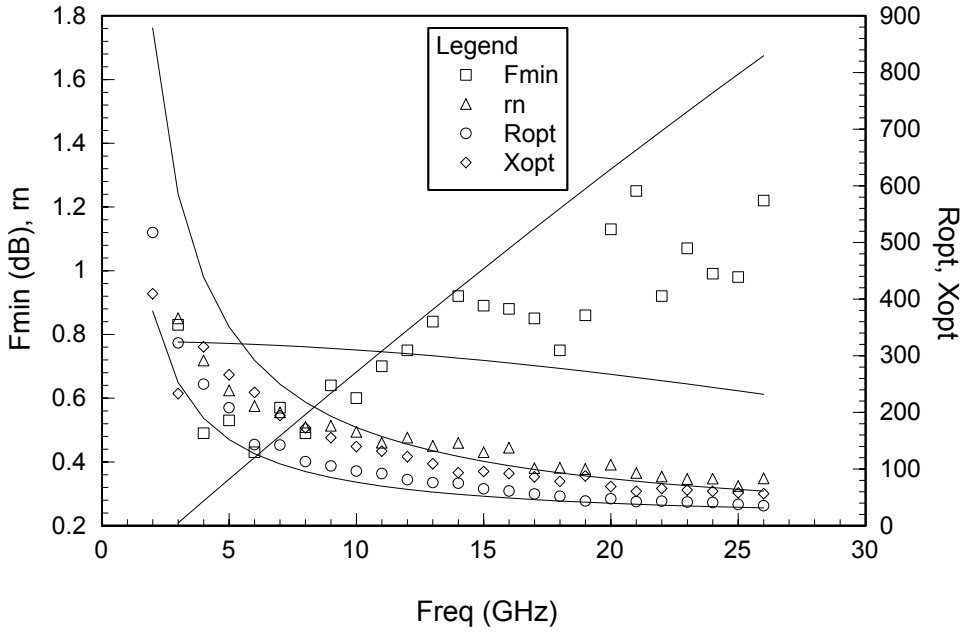

Figure 5.26 Noise Parameter Comparison of Measured versus Modeled at V_{ds} =1, I_{ds} =8ma and 85°C. Measurements are indicated by markers, modeled data are shown as solid lines.

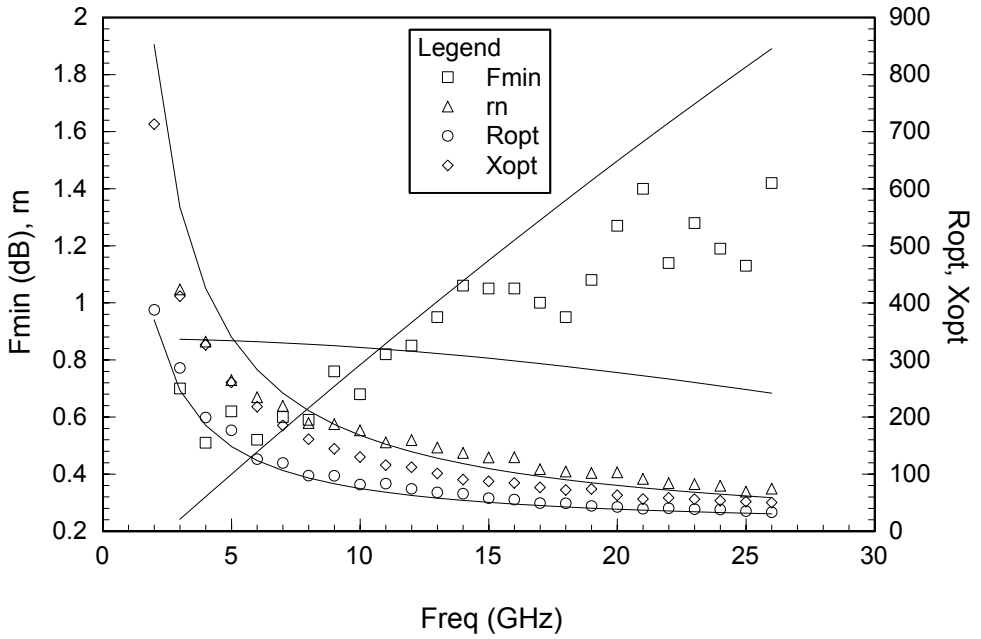

Figure 5.27 Noise Parameter Comparison of Measured versus Modeled at V_{ds} =1, I_{ds} =12ma and 85°C. Measurements are indicated by markers, modeled data are shown as solid lines.

In viewing the preceding graphs, it is evident that there are problems fitting at 1mA for each drain voltage and temperature. This problem should not be of much concern, however, since it is well out of the device's normal operating range. At 1mA, R_{ds} was usually a large value and g_m is low as can be seen in Appendix C. In reference to equations (2.33) and (2.34), g_m, R_{ds}, and R_i play an important role in the determination of T_d and T_g in relation to the non-dimensional coefficients P and R which are based partly on the Y-parameters (see Chapter 2).

Fits to R_{opt}, X_{opt}, and F_{min} were generally good. There is room for adjustment in the noise generators T_g and T_d to fit F_{min} better, but it is noted that too much alteration will change the source match for F_{min}. The most important factor in the modeling should be the source match for noise, since this is the parameter of interest in the design of a low noise amplifier. Difficulty was encountered matching the trend of R_n through frequency and bias. All the extractions were performed using the noise calculation worksheet

created in ADS. The values were determined by an averaging approach of the extracted temperatures, T_g and T_d, over frequency. Better fitting could be accomplished by optimizing, but this would require much more time given the number of biases chosen for this study.

As the temperature of the transistor was lowered to $-55\,^{o}$C, the modeled gate temperature would approach single digit numbers in Kelvin. A study of the parasitic gate resistance extracted from room temperature data is shown to see how much of an effect the change of R_i will alter T_g. An investigation to see the effects of altering R_i and setting T_g to the ambient temperature is shown in the next section.

5.2.1 Investigation of Ri and Gate Temperature

Due to the general trend toward lower noise figures for high electron mobility transistors (HEMTs or MODFETs), the corresponding measurement and modeling has become increasingly difficult. If the design task involves using an LNA in a cold environment to further reduce the noise output, a measurement dilemma is faced. The question arises as to whether the actual measurement of the device is good enough to even model accurately. Given any drift in the calibrated system through the measurement, a device with a noise figure of only 0.05 dB could suddenly be showing 0 or even -0.2 dB. The very issue of noise data being physically real has been elaborated on [39]. This reference is based on the principle that a minimum noise temperature measured at a given input impedance to a two-port is consistent for any lossless embedding. Equation (5.1) shows the necessary condition how T_{min}, R_n, and G_{opt} represent a physically real two-port [22].

$$T_{\min} \le 4R_n G_{opt} T_o \tag{5.1}$$

The plot resulting from application of Eq.(5.2) to noise data in a sample device is shown in Figure 5.28. A value below 1 is not above the fundamental inequality defined in (5.1). A value over 2 exceeds the ability of the noise model extraction procedure outlined by Pospieszalski [22].

$$1 \le \frac{4R_{opt} g_n T_o}{T_{\min}} \le 2 \tag{5.2}$$

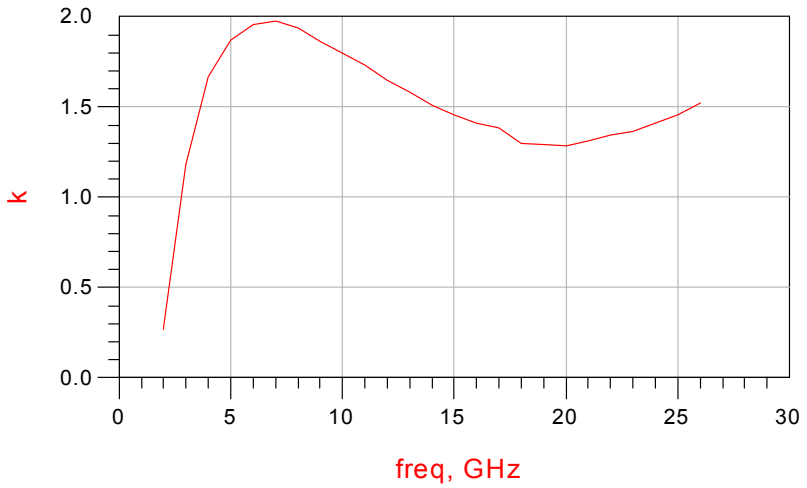

Figure 5.28 Plot of Physically Real Noise at –55 ^{o}C at 1 volt V_{ds} and 8 mA Drain Current.

Since the mHEMT used has such a low noise figure at room temperature, when measured at –55^{o} C, the delicate nature of getting good noise parameters is problematic. From examining figure 5.28, the region for the best noise extraction should be after 10 GHz. Assuming that good data has been retrieved, the task of constructing a model proceeds by extracting an intrinsic S-parameter block by treating extrinsic elements as negative values. Using this approach rather then introducing computed values for Y_{11} and

Y_{21} from the ECPs resulted in the best model fitting. Standard practice was to extract *P,R*, and *C* values and convert to the temperatures T_g and T_d for R_i and R_{ds}, using the techniques from Pospieszalski [22].

Since F_{min} increases linearly with frequency as noted by Hughes [40], the model represents a smoothed slope versus frequency compared to the raw measurement data. The user has the option of using either smoothed or raw data when extracting the noise model. Although modeling using smoothed data is easier, the raw data will give a better outlook as to what frequencies of F_{min} best represent the transistor. Most of the data used in this modeling effort came from smoothed data. (Smoothed data does not give the option of omitting bad data once the s2p file is created). The slope of F_{min} can also vary according to the values of T_g and T_d. If the smoothed data is used, it must be realized that bad data at low or high frequencies can alter the slope, which leads to modeling errors.

From preliminary modeling results, T_g values were in the single digits. In Table 5.1, one set of results is shown (Set 1). The literature indicates that the noise generators for cryogenically cooled devices can be as low as 16 K for T_g and 523 K for T_d [41], but the ambient temperature is 12.5 K. It seemed necessary at this point to examine the effects of the small signal model on T_g and T_d, particularly in reference to R_i. The small signal ECPs provide an excellent fit for the S-parameters but resulted in a T_g that was somewhat lower than expected from prior work. Another issue that drew even more attention, was that T_d is large at 4379 K compared to 6 K for T_g. Schlechtweg et al. and Tasker note in their investigations that the uncertainty of T_d could be as much as 109 K [42, 43], but no mention is made of the uncertainty and validity of T_g.

Garcia et al. [44] noted that at higher drain currents, the two-parameter noise model was favored, whereas lower drain currents, T_g could be set to the ambient temperature. It is also verified in [43] that T_g can be set to ambient if drain currents are small. Another source implies that the only perceived effect of T_g versus drain current is thermal regardless of the bias condition [45]. In this study, it was found that even at high drain currents for this device size, T_g never rose above 20 K.

The values used for the extrinsic resistances were derived from ambient temperature measurements or 25°C. If the same values are used for circuit simulations at –55°C, the noise figure can be so low that the extraction of T_g seems unreal and uncertain. If the value of R_i is large enough, and the value for the extrinsic gate resistance is large enough, T_g can approach zero for extremely low noise figures.

Pospieszalski and Niedzwiecki [45] have concluded that the drain temperature is dependent on the drain current, but the extraction of R_i can cause errors in scattering values of T_g from $T_{ambient}$. If this is the case, then a closer examination of *Ri* is needed during the small signal extraction. This examination will require the user to set constraints on ECPs in order to gain reasonable results.

Three methods were made to achieve a good fit to the measured noise parameter data. The three models comprised the original noise model {Set 1}, a model based on setting R_i to $T_{ambient}$ and refitting T_d {Set 2}, and a model based on a new extraction for T_d with a constraint placed on R_i to 0.5 ohms and set to $T_{ambient}$ {Set 3}. In Table 5.1, the ECPs are listed for the three separate models. In Figure 5.29, the fits for F_{min} for each set seem to provide decent outcomes given the differences in ECP values. When T_g was set to 218 K, T_d had to be lowered significantly to alter the slope of F_{min} but when R_i was

altered, T_d remained constant. In Figure 5.30, the value for R_{opt} is considerably altered if T_g is forced to the ambient temperature. The fit by constraining R_i to a low value seems to match the measured data as well as Set 1. It is evident that the reactance is not affected by T_g since its relation is to C_{gs} and T_d [22]. For Set 2, R_n showed a reduction in that T_d is a quarter of the original value, even though T_g is increased by 40. Set 1 and Set 3 produced similar outcomes for R_n as seen in Figure 5.31.

Table 5.1 Equivalent Circuit Parameters for the Three Different Model Sets.

	g_m	C_{gs}	C_{gd}	C_{ds}	R_{ds}	Tau	R_i	T_g	T_d
Set 1	58.2	67.7	20.0	45.9	360	.011	5.87	6.0	4339
Set 2	58.2	67.7	20.0	45.9	360	.011	5.87	218	1039
Set 3	58.7	69.3	19.5	44.8	336	.115	.5	218	4376

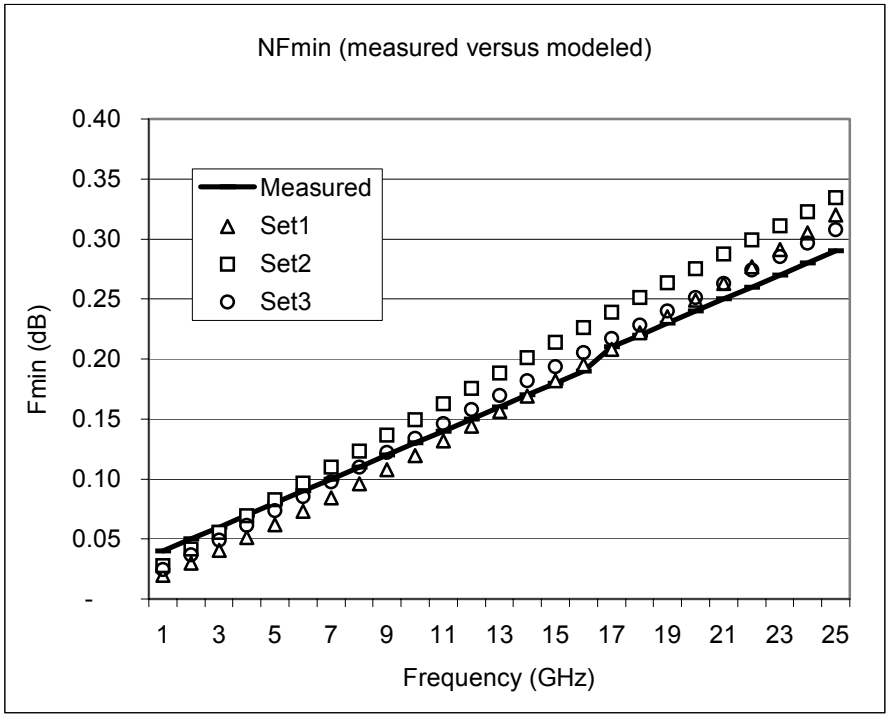

Figure 5.29 NF_{min} of the Measured Data versus the Three Model Sets.

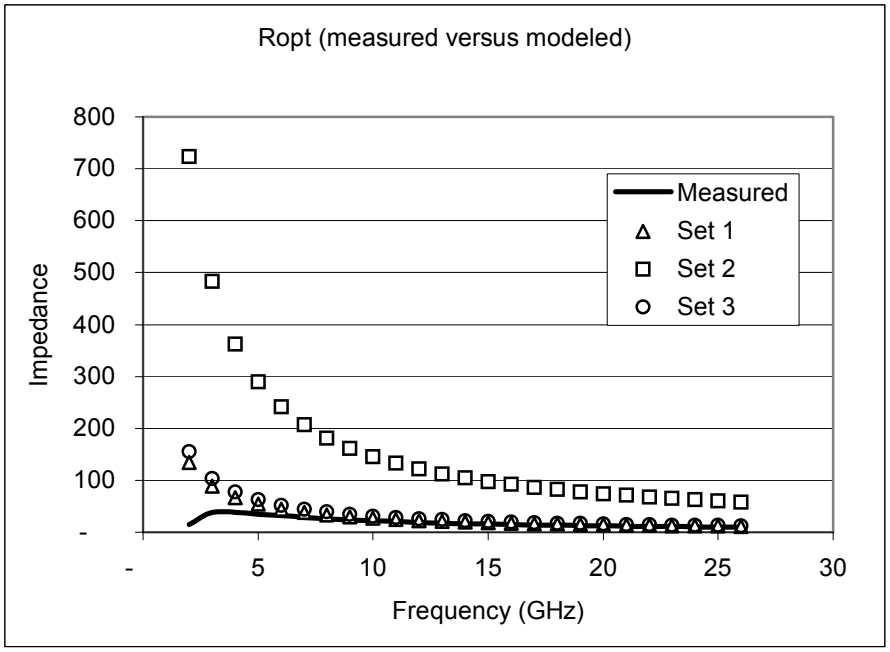

Figure 5.30 R_{opt} of the Measured Data versus the Three Model Sets.

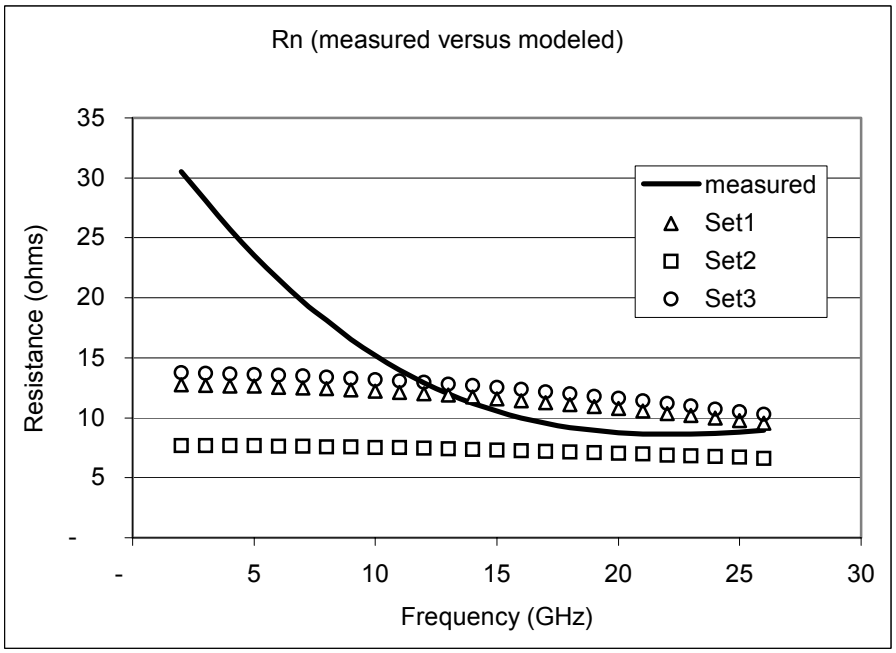

Figure 5.31 Noise Resistance of the Measured Data versus the Three Model Sets.

Upon reviewing the data from the three models, it can be assumed that modeling noise generator T_g may not always have to be related to a physical phenomenon. Given a certain small signal model, a particular solution can be found that will produce good results for noise fitting. For analyses, or in generating a sensible noise model, a constraint will need to be placed on R_i. The method in which this constraint is determined, depends on the device itself.

The resistance R_i, which determines the rate at which the depletion layer capacitance is charged [22], is known to be difficult to model. Shown in (5.2) is the formula derived by Berroth and Bosch that uses the intrinsic y-parameters to find R_i after C_{gd} is extracted from the imaginary part of Y12 [19]. As explained by Pospieszalski [22], the ability of T_g to be used as a real value for the thermal properties of the gate or strictly as a fitting parameter relies on the ability of R_i to be accurately modeled. In altering the value for R_i, it was noticed that the fit to S-parameters was better when R_i was set to 5.87 ohms rather than 0.5 ohms.

$$R_i = \frac{\mathrm{Re}\left(Y_{11}\right)}{\left(\mathrm{Im}\left(Y_{11}\right) - \omega C_{gd}\right)^2 + \left(\mathrm{Re}\left(Y_{11}\right)\right)^2} \tag{5.3}$$

The series combination of R_i and C_{gs} represents an RC charge parameter and it is assumed that the value for R_i is strictly for this purpose when extracting the small-signal model. In this case, the real resistance value is not necessarily represented physically and can be defined with any noise temperature T_g in order to fit measured noise data. Furthermore, the actual value of T_g in regards to the ambient temperature is not dependent or real, and any value that fits the noise data sufficiently is concluded as being the proper fit. All the noise model extraction in this work is based on the author's presumption of this theory.

5.3 Temperature Dependent Verification

The work done in earlier USF table modeling included a temperature dependence based on linear slope equations [4,5]. This approach relies on the premise that the trend of the ECPs are linear versus temperature. For the Raytheon mHEMT model, three temperatures were used for the bias dependent S-parameter sets. One at ambient temperature, or 25°C, and the other temperatures are –55°C and 85°C. Previously, only temperatures above room temperature were used by using a controlled thermal chuck. With the use of a closed air probe station at Raytheon RF Components in Andover, Mass., lower temperatures were available by injecting nitrogen into the enclosure. The wide range of temperatures will test the applicability of the linear trends for ECPs for the target mHEMT devices.

The temperature dependent model will not be accurate if the extractions at each temperature are not correct. A bias of V_{ds}=1 at 10 mA was chosen for temperature validation because of the success of the extraction at this bias. The average change of the ECP values over each degree above and below 25°C is calculated and then used to assign a value to each parameter that is used in a slope equation in ADS. The extracted values at 25°C are used as y-intercept point. The ambient temperature plus or minus 25°C is multiplied by the slope value and either raises or lowers the ECP value.

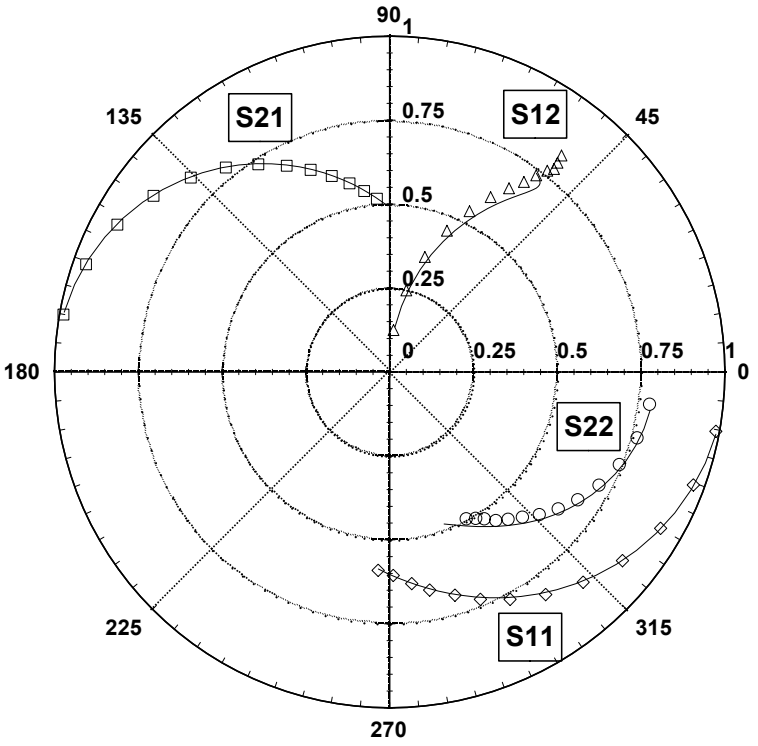

Figure 5.32 Comparison at 55 ^{o}C of Measured and Modeled S-parameters at V_{ds} of 1 Volt. Measurements are indicated by markers. Modeled data are shown as solid lines.

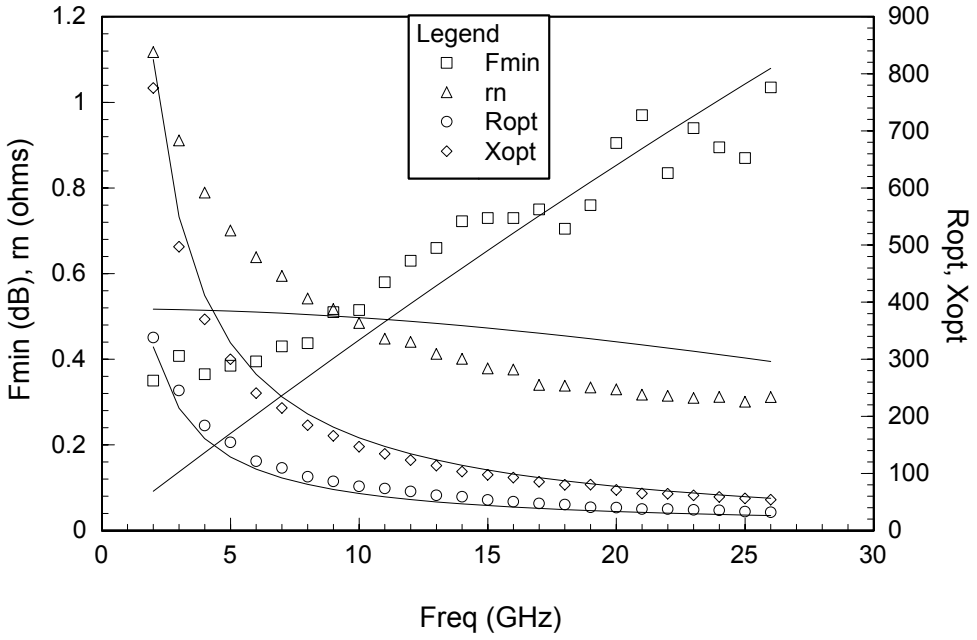

Figure 5.33 Noise Parameter Comparison of Measured versus Modeled at V_{ds}=1, I_{ds}=10ma and 55^{o}C. Measurements are indicated by markers, modeled data are shown as solid lines.

Based on the results of the graphs in Figures 5.32 and 5.33, the slope equations work favorably to match the measured data 55°C. Although the variations in the S-parameters are minimal with temperature, the noise figure change is more pronounced. From Figure 5.33, the match to Γ_{opt} and F_{min} is favorable along with the S-parameters in Figure 5.32. One consideration is noted though. The extraction of the noise parameters at several temperatures yields slightly different slopes between each set of temperatures. In this study the average of the two slopes between –55°C to 25°C and 25°C to 85°C were used to find the final slope using the 25°C parameters as the y-intercept for the slope.

5.4 Nonlinear Modeling Results

The initial result of the ICCAP extraction of the HEMT1 model yielded good results for small-signal s-parameters. With minimal manipulation, each extraction routine matched measured S-parameter data. Only the extrinsic elements needed to be adjusted to match the data. These extrinsic elements could simply be carried over from the small-signal model since they are bias and power independent. For low power levels, the S-parameter simulations of the large-signal model should match those of the bias dependent noise model. A comparison at V_{ds}=1 is shown in Figure 5.34.

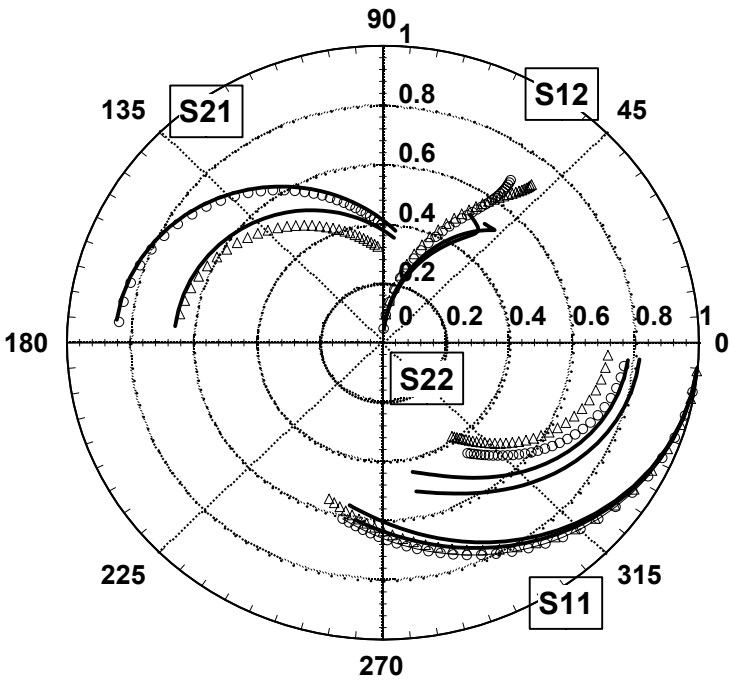

Figure 5.34 Comparison from 1 to 30 GHz of the Nonlinear Model versus the Table Model at a Drain Voltage of 1 volt. (Circles are 10 mA , triangles are 5 mA for the nonlinear model). S21 is divided by 6 and S12 is multiplied by 4.

From Figure 5.34, a good match is obtained at low frequency except for the discrepancy with S22. As the frequency is increased above 10 GHz, there is a noticeable difference between the model and data. This could be because the extraction of the model over bias may not fully reflect the proper output conductance due to a limitation in the DC model. The nonlinear model also contains a series RC dispersion component that affects the output match of the model. The dispersion model accounts for electron trapping and self-heating effects noted in static DC measurements. With some additional work on the small signal components of the model, a better fit could be achieved. Since the small-signal model is extracted at each bias, it will be more accurate at a given drain voltage and current rather than a quiescent bias in the nonlinear model case. This is

evident from the match between measured and modeled s-parameter comparisons in the section 5.1.

5.4.1 DC-IV Results

The DC modeling section of the EEHEMT model includes four different equations to map the drain current of a transistor, and provides an excellent match to the characteristics of the device under test. The mHEMT turns on relatively fast, which places the knee region approximately at a drain voltage of 0.3 volts. Because of the range of bias used for the DC-IV curves, the device was not subjected to significant self-heating. The reason for narrowing the drain voltage range was due to the impact ionization caused by drain voltages above 2.5 volts that results in oscillations in the current. Further analyses of the DC curves show that the output conductance, $g_{ds,}$ decreases at higher V_{gs} values and the transconductance, g_m, increases with V_{gs}.

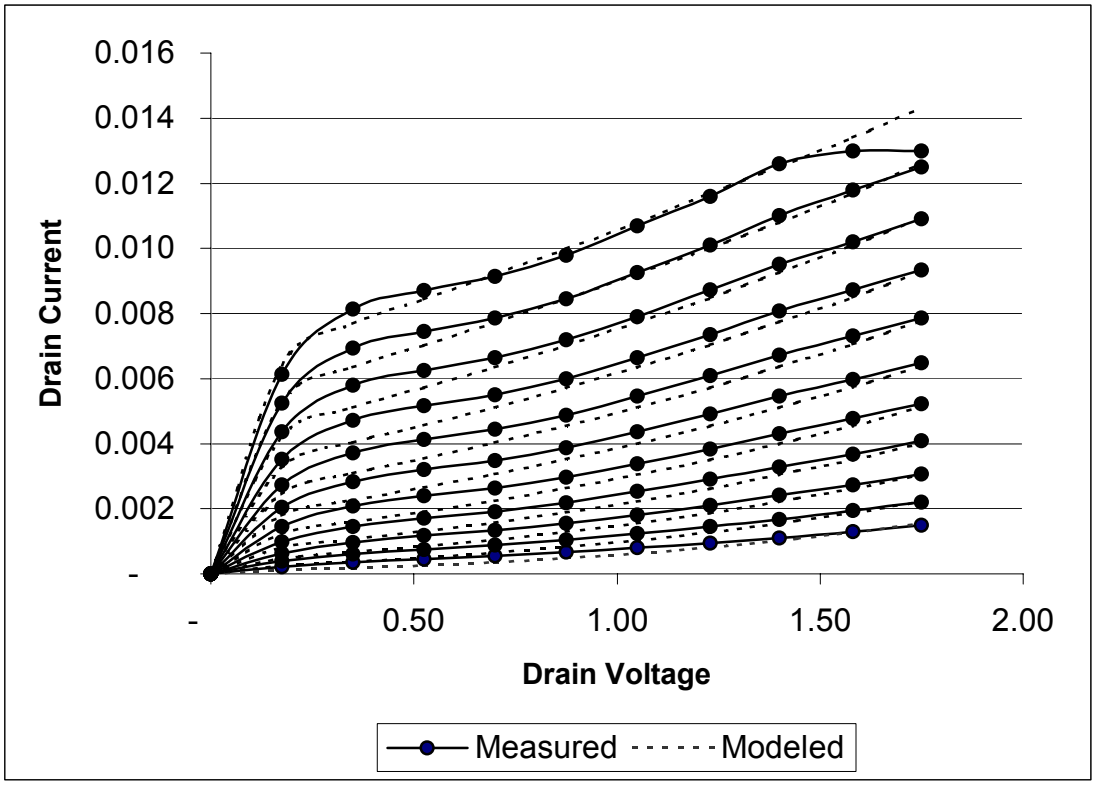

Figure 5.35 DC-IV Comparison of Measured versus Modeled of the 75 um mHEMT.

5.4.2 Compression and P.A.E. Results

Further verification of the model was achieved using the Maury Automated Tuner System, ATS, to measure gain, compression, P.A.E., TOI, and load-pull. The system comprises a desktop computer, Maury ATS controller, mechanical load tuner, Anritsu 2438 power meter, HP 36530 bias supply, and an HP 8510C VNA. The system uses tuners that are pre-characterized using a VNA at a given frequency to facilitate daily setup and calibration. Only the connectors and cables need to be measured for a particular setup for de-embedding purposes. The computer uses the tuner files and S-parameter files for the measured sections to rotate the reference plane from the tuner to the DUT. The power loss is also calculated from the fixture S-parameter files and taken into account during the power calibration.

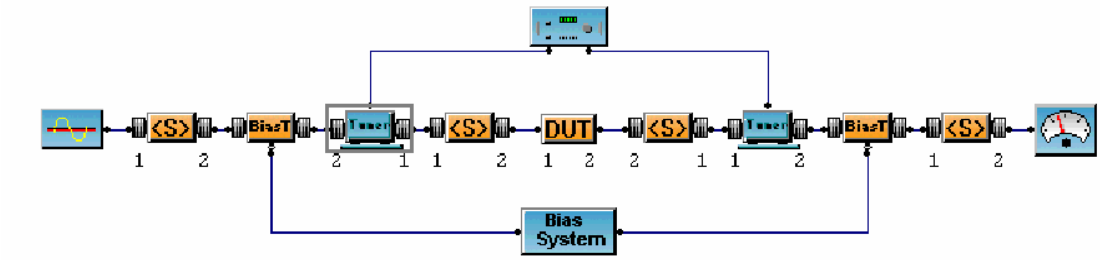

Figure 5.36 Maury ATS Software Setup of a Source and Load-Pull Power Measurement Setup.

In this section, the comparisons are made using a 50 ohm output condition with no tuning. A load-pull was also measured as well as a power sweep with the load-pull match. Since the gain compression is dependent on the output power, the unmatched condition will be adequate to show P1dB and the efficiency of the transistor at that point. To prevent the destruction of the limited number of samples available, the power compression was kept to a minimum of 2dB. This precaution kept the validation

measurements in Figures 5.37-39 from exploring the range of input powers necessary to completely verify the simulations.

In the initial results of the compression simulations, as compared to the Maury measurements, the simulated output power compression curve was not representative of the device. Since the model contains gain compression parameters as noted in Table 3.2, the user has the ability to adjust this portion of the model to fit the measured data. By tuning the parameter V_{co}, the gate voltage at which g_m begins to roll off from its maximum value can be adjusted to a particular drain current versus drain voltage. Two other parameters that greatly influenced the simulation results were Deltagm and Alpha (Δgm, α). By defining the slope of compression and the saturation to compression transition, the model matched the measured data with much improvement. Figure 5.37 illustrates this result by showing the difference between the initial extraction with ICCAP and the adjusted model by the user. The initial extraction parameter values and the final values are shown in Table 5.2.

Table 5.2 Initial and Final Values for the Extracted Compression Parameters.

Parameter	Initial Extraction	Final Model
V_{co}	-250.6 mV	-371.2 mV
μ	333.3 u	333.3 u
V_{BA}	1	1
V_{BC}	.4	.4
Δgm	175.9m	783.5m
Δgm_{ac}	175.9m	746.7m
α	100 mV	10 mV

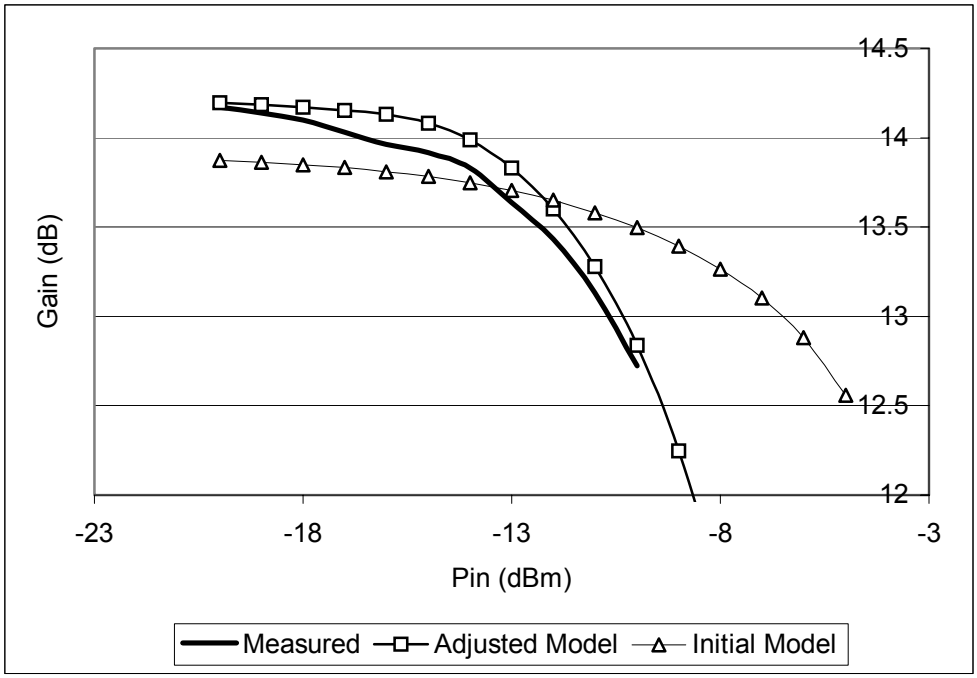

Figure 5.37 Comparison of Initial Model and the Adjusted Model versus the Measured Results from the Maury ATS System for Gain Compression.

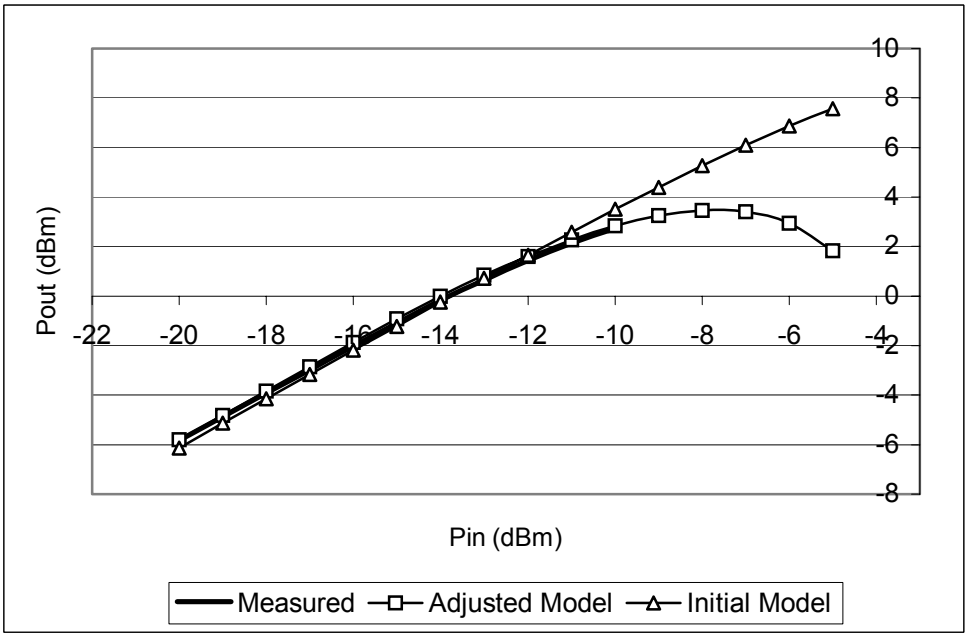

Figure 5.38 Comparison of Initial Model and the Adjusted Model versus the Measured Results from the Maury ATS System for Pout.

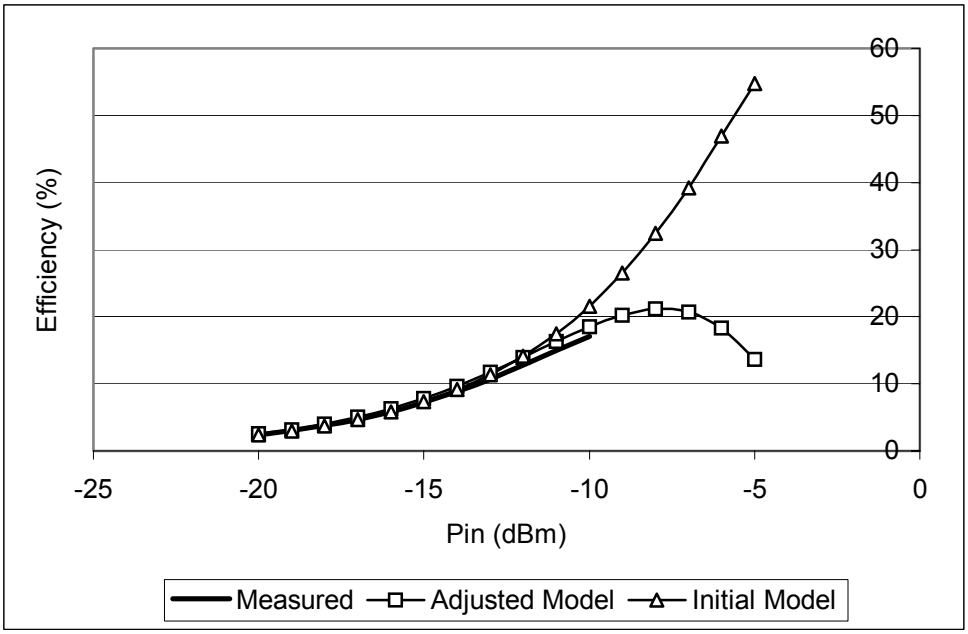

Figure 5.39 Comparison of Initial Model and the Adjusted Model versus the Measured Results from the Maury ATS System for P.A.E.

From Figure 5.39, the initial model seems to have unreasonable expectations for efficiency due to the slope of compression for Figure 5.37 and the slope of Pout in Figure 5.38. The final model seems to follow the predicted path of the measured results favorably. Since several devices did not survive repeated compression testing, the measurement limits were lowered.

5.4.3 Load-Pull Verification

Using the Maury ATS to change the load provided to the drain of the DUT, the optimum reflection coefficient can be found for maximum gain, Pout, and power-added-efficiency. The input power for these measurements are at a level that would put the device at P1dB output compression power. This input power level is calculated by performing a load-pull at a lower power to find the power gain, Gp. By performing a 50 ohm power sweep, the linear gain minus one is subtracted from the output power

measured at P1dB to find the appropriate input power needed. Since the Maury controls the bias supply also, the load-pull includes loads for maximum efficiency.

The load-pull simulations in ADS use a variable equation editor to define the positions that the output of the transistor model will see at port 2. By using the model's DC-IV data, large-signal S-parameters, and compression characteristics, the results of the simulation can predict optimum load conditions with relatively good accuracy as presented in the next set of figures.

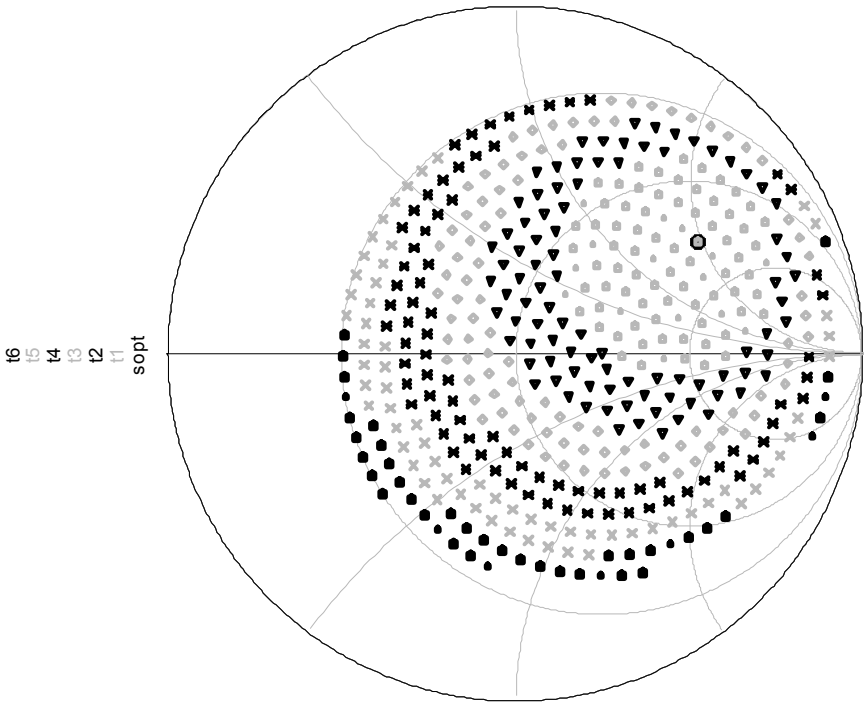

zmax	sopt
-1.412	0.617 / 31.308

Figure 5.40 Simulation of a Load-Pull in ADS of EEHEMT Model of 75 um mHEMT for Maximum Pout. Different shadings identify regions of 1dB steps.

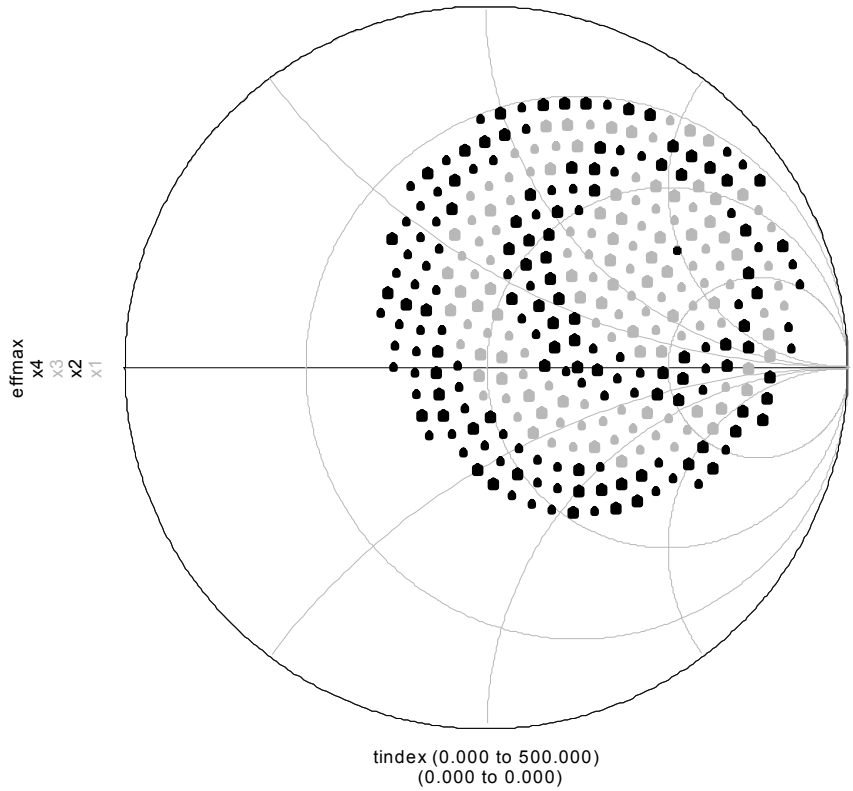

freq	DC.Id.i	effmax	ymax
0.0000 Hz	9.982mA	0.617 / 31.308	7.251

Figure 5.41 Simulation of a Load-Pull in ADS of EEHEMT Model of 75 um mHEMT for Efficiency. Different shadings identify regions of 1 % steps.

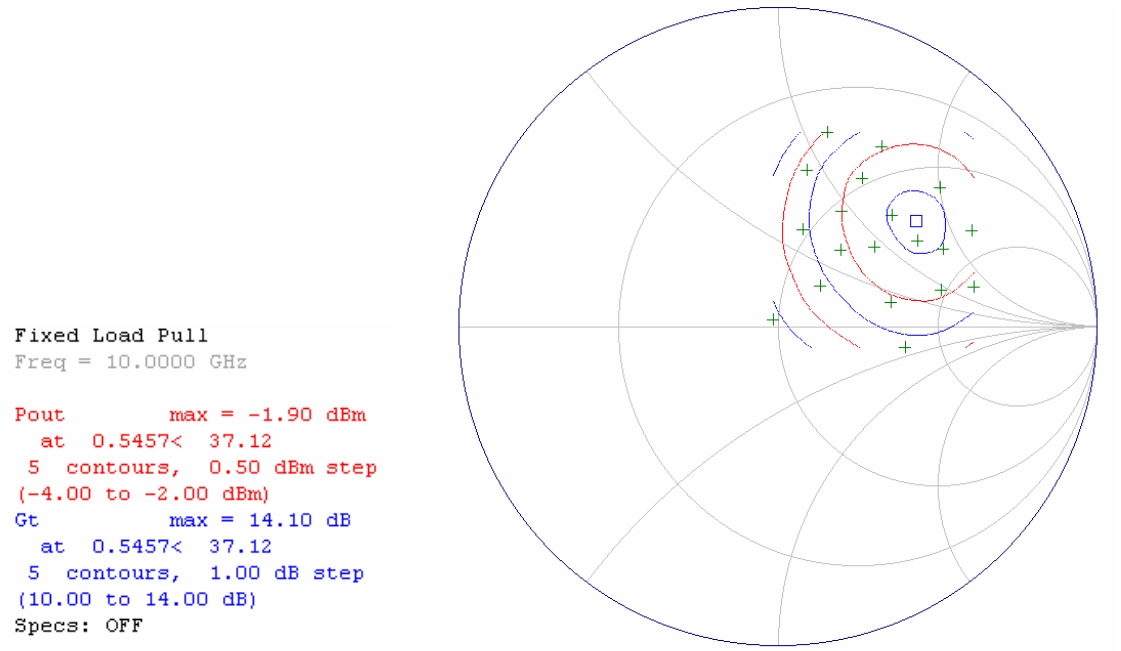

Figure 5.42 Maury Load-Pull Measurement of the 75 um mHEMT for Maximum Pout and Gain.

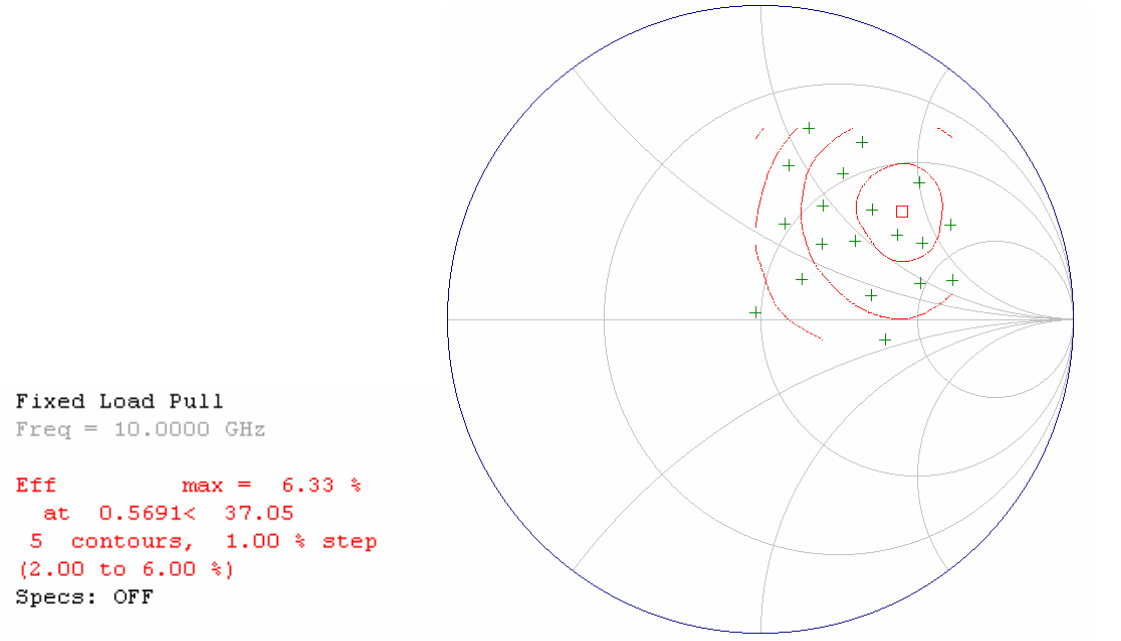

Figure 5.43 Maury Load-Pull Measurement of the 75 um mHEMT for Maximum Efficiency.

The input signal conditions for both the simulated and measured load-pull were at an input of −16 dBm and a frequency of 10 GHz. The bias was set at 1volt V_{ds} and 10mA I_{ds}. The measurement yielded a result of –1.9 dBm at 0.55< 37.12 and a gain of 14.1 dB. The simulation resulted in –1.41 dBm at 0.617< 31.7 and a gain of 14.59 dB. These products do not include any matching at the source that could raise the overall transducer gain much higher. For efficiency, the simulation resulted in 7.25 % at .617< 31.3 and the measurement was 6.33 % at .569< 37.1.

5.4.4 TOI Verification

Another test of the performance of the large-signal model is harmonic signal prediction and distortion. One measurement for this is the Third-Order-Intercept, TOI, point that is defined as the intercept between the slope of the first and third harmonic. Figure 5.44 displays the results of a measurement on the Anritsu Scorpion 3-port VNA and a simulation of TOI in ADS of the mHEMT large-signal model.

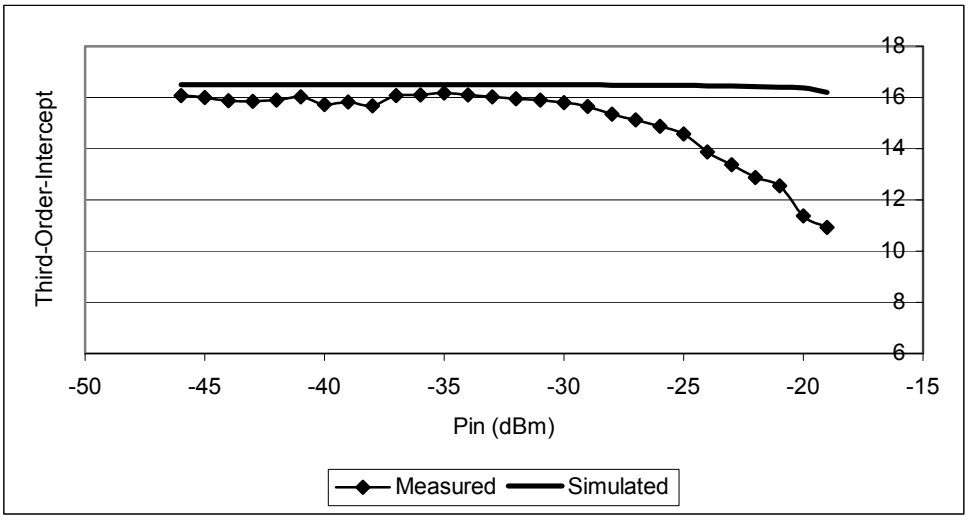

Figure 5.44 Comparison of Measured and Modeled TOI at V_{ds}=1 and I_{ds}=8mA for the EEHEMT Model.

The measurement and simulation show good correlation at low power levels but deviate as the device enters into compression. The difference can be attributed to a possible entrance of passive component harmonic content or equipment harmonic distortion. The model also seems to enter into compression at higher power levels than what was measured. With continued effort in this work, an evaluation of TOI with respect to nonlinear modeling could be further expanded.

5.5 Chapter Summary

This chapter is a compilation of validation performed on the small and large-signal models for the 75um mHEMT. For the noise model, the S-parameter fits were commonly within the allowed 3% difference as defined in Chapter 4. The noise modeling, however, proved to be the most difficult of all the efforts here. The extraction of the noise generators was not regulated to a standardized procedure but required several attempts to achieve a good fit. The values of T_g and T_d over frequency were varied and required the user to select the best range for fitting the measured noise parameters. This matter was also discussed further in reference to ECPs from the small-signal model and their effect on the extraction of the noise model. Nevertheless, the temperature dependent model proved to be successful for the bias and temperature range used for fitting both noise and S-parameters.

The initial large-signal model extraction using ICCAP produced proficient DC-IV and S-parameter prediction but the compression characteristics necessitated further modification to match power measurements from the Maury ATS. Given that the EEHEMT model includes parameters for this purpose, the tuning was relatively

straightforward once an understanding of how each model parameter affects the device simulation. The load-pull data also showed agreeable results to the model in terms of maximum Pout and power added efficiency. In the final chapter, conclusions will be made concerning what could be improved in this work and recommendations on continuing modeling work.

CHAPTER 6

CONCLUSIONS, LIMITATIONS, AND RECOMMENDATIONS

Two modeling approaches were utilized in this thesis, the first of which was the development of a bias and temperature dependent small-signal noise model for a 75um Raytheon mHEMT. This model used a linear S-parameter extraction procedure to create bias and temperature dependent capability. The noise modeling was executed using a routine created in ADS using standard techniques from several technical papers and previous research work. Some of the measurements were conducted at Raytheon over three different temperatures to facilitate a fitting algorithm for temperature dependence. Biases were interpolated using built-in ADS interpolation of a dataset file.

The other modeling method was to implement a large-signal model of the Raytheon mHEMT. The large-signal or nonlinear model used was the Agilent EEHEMT model. This model was available as both an extraction and measurement routine in IC-CAP and a supported model in ADS. This model was chosen based on the hypothesis that its complex DC model would best represent the characteristics of the mHEMT. In addition, the model's available dispersion parameters would characterize the self-heating and electron trapping effects evident in the DC-IV curves.

The device studied in this thesis is a 75um mHEMT provided by Raytheon RF Components in Andover, Mass. The technology behind this device, described in Chapter 1, is based on the ability to create a transistor with a high Indium content on a GaAs

wafer. This allows the benefit of low cost manufacturability with high performance. Previous modeling studies at USF range from GaAs to InP, but this is the first modeling project where both technologies are used together. The device used in this study was designed primarily for high frequency, up to 110 GHz, low noise and low distortion amplifier design. This transistor would later prove a challenge to the noise measurement and modeling.

The equipment used for the measurements needed for the small-signal and noise modeling consisted primarily of the ATN NP5 noise measurement system. Using the instruments in this system, the generated "s2p" files containing all the noise parameters and s-parameters contain all the required data needed for this model. The large-signal model was measured and extracted completely with the USF IC-CAP system (consisting of IC-CAP software, computer, an 8510C VNA, and a 4142 DC power supply). The UNIX based computer controls all equipment and records data to extract the model, which is then translated into ADS.

Completion of this work required that the noise model and the nonlinear model should operate entirely in ADS version 1.5. Any custom extraction routines developed were implemented in ADS. The noise model is able to predict noise and S-parameters over many biases and temperatures by interpolating between extracted ECPs. The nonlinear model goals were met by verifying prediction of DC, compression, efficiency, load-pull, and TOI. Although many of the comparisons for the noise model were against data measured to derive the small-signal model, the large-signal model was compared to additional measurements not included in the data set used for nonlinear model extraction.

6.1 Model Challenges

In this study, the device technology presented a number of challenges. Many of these challenges surfaced from measurement issues related from low noise figure at –55^{o}C to parasitic extraction. The parasitic resistances were found to be near 0.1 ohms while large source via structures introduced significant parasitic inductance. These components presented difficulties in determining an extrinsic model that best represent the parasitic components because the source inductance overwhelmed the effects of the gate and source resistance in forward biased measurements. Rather than use just S-parameters to determine these parasitic values, different biasing techniques were used such as the Yang-Long procedure that acquires resistances from the change in gate currents.

The gathering of noise data also represented challenges to the noise model. Since the noise figure measurement can have a degree of uncertainty of +/-0.2 dB, the mHEMT data proved to be problematic since the range of noise figure was between 0.05 and 0.6 dB at cold ambient temperatures from 2-26 GHz. The low temperature data had to correspond with room and hot temperature measurements by a linear fashion for the table-model to interpolate properly. The noise data needed to be evaluated at each bias so that measurement errors could be accounted for or eliminated in the interpolation.

The nonlinear model challenges of this thesis were the result of the Agilent EEHEMT model complexity. Unlike the Curtice-Cubic or Statz nonlinear models, the EEHEMT is an empirical model that is structured to fit measured data. Earlier nonlinear models were basically equivalent circuit models with bias dependent capacitances and a drain-to-source current equation that defined the transconductance and output

conductance. After reviewing earlier nonlinear models, the comprehension of the EEHEMT model is easier due to the similar traits of these models that include a drain-to-source current and voltage dependent capacitance models.

The model behavior was not necessarily accurate after the initial extraction in IC-CAP, which lead to optimization in ADS to correct S-parameter fit and gain compression data. These modifications of the model parameters lead to a better understanding of the purpose of each parameter and allowed the optimization to follow a practical path to better fitting. Much of the initial inconsistencies resulted form the inaccurate parasitic extraction. Using the values for extrinsic resistance and inductances determined from the small-signal model, the S-parameter fitting and capacitance models were improved.

Measuring the actual gain compression and power added efficiency were also problematic. Because of the nature of these mHEMTs, the input power needed to be carefully monitored as to not cause the transistor to fail during testing. Gain compression was kept at a minimum allowing only 2 dB and biasing was also reserved to lower drain voltage values. The model was able to predict the measured data well, but further testing would improve prediction of the nonlinear behavior, especially maximum output power and efficiency.

6.2 Improvements and Recommendations

At the end of this thesis project, many possibilities for improvements had developed that could be pursued further by future work. Because of the time constraint, these items could not be included in this work. The areas incorporated everything from different measurement solutions to diverse extraction methods and optimization.

Since the mHEMTs used in this work exhibit such low noise figure, measuring the noise parameters up to 40 GHz would provide a better overall trend of the data as compared to the 26 GHz data. Possible source tuning to lower frequencies could be done with the Maury Automated Tuner System configured for noise testing down to 800 MHz to further extend the range. Also, measurement of the 50 ohm noise figure could be taken down to 10 MHz. Further knowledge of the ATN noise measurement system also helped later in the project in determining the right test conditions to produce good results. Items that became useful during operation of the ATN system incorporated the auto-state deletion function, setting the number of tuner states, LO power, and RF attenuation. The auto-state deletion allows the software to determine bad data points and removing them before computing the noise parameters at the given frequency.

Test conditions at times produced poor measurement data. Because of the low noise figure, temperature changes in the room would cause the calibration to drift far enough as to warrant a new calibration. Proper stabilization of the temperature using some type of localized temperature control and monitoring system would have alleviated calibration drift. The S-parameter calibration used to establish the reference plane of the device would give incorrect noise match and noise resistance during the measurement. The reference calibration would also at times produce erroneous errors such as gammas located outside the Smith Chart.

The extraction of the extrinsic or parasitic parameters was complicated by the low values of the gate, source, and drain resistances. Using standard techniques of monitoring the real part of the S-parameters while changing the gate voltage gave values that were either too high or negative. Using the Yang-Long method, improvements were made for

both the gate and drain resistances. Enhanced optimization of these values before extracting the small-signal model allowed improved fitting across the bias range.

In the field of noise modeling, more research could be conducted on different device sizes and concentration of InP in the MHEMTs to study the effects of deriving good noise parameters given different small-signal model parameters. Ongoing work is being done at Raytheon RF Components on the percentage of InP in relation to efficiency, gain, and noise. The effects of the small-signal components themselves could be studied in correlation to their impact on improving noise parameter modeling. As discussed in Chapter 5, the effects of the intrinsic component R_i, had an impact on the modeling of the equivalent noise temperature, T_g.

Nonlinear modeling of the mHEMT had also presented many challenges to this project. Unlike small-signal modeling which is able to accurately predict S-parameter fits at a particular bias, nonlinear models are ever changing to allow more complex fitting methods allow fitting across the IV plane. More advanced DC-IV and nonlinear charge equations are being developed for Si and GaAs processes. Recent studies in the literature point to modeling not only for class A or AB amplifier design, but class E and F. Both class E and F involve operating the transistor in conditions which are not used for model extraction. Since the advent of high efficiency power amplifiers, the need for models that predict class E and F performance is ever increasing. The modeling difficulty lies in the IV and charge model predicting accurate S-parameters and harmonic power at the bias conditions required for high efficiency design.

Another area of study would be the effect of using pulsed or dynamic DC measurements in modeling a transistor. Static DC measurements don't account for the self-heating and

dispersion effects. The proper modeling of self-heating in the model requires careful attention since the procedure is not well defined or implemented in IC-CAP. This work could involve pulsed measurements over different ambient temperatures to define a thermal resistance.

In terms of nonlinear or harmonic analysis, large-signal models are still being improved to predict harmonic distortion. Load-pull of second and third harmonics directly influence the efficiency of transistor design as well as load-pull for TOI. Extraction of DC models including the fitting of the first and second derivatives of R_{ds} and g_m may possibly correct inconsistency in measured versus modeled comparisons of harmonic power and harmonic distortion.

REFERENCES

[1] Raytheon RF Components 263 Lowell Street, Andover MA., 01810.

[2] P. Winson, S. Lardizabal, and L. Dunleavy, "A Table Based Bias and Temperature Dependent Small-Signal and Noise Equivalent Circuit Model," *IEEE Trans. Microwave Theory Tech*., vol 45, no. 1, pp. , Jan. 1997.

[3] Agilent Technologies 395 Page Mill Rd. P.O. Box #10395 Palo Alto, CA 94303.

[4] P. Winson, An Investigation of Linear and Nonlinear Modeling of MESFET Characteristics as a Function of Temperature, Ph.D. Dissertation, University of South Florida, 1997.

[5] S. Lardizabal, Bias and Temperature Dependent Noise Modeling of Microwave and Millimemter-wave Field Effect Transistors, Ph.D. Dissertation, University of South Florida, 1997.

[6] H. Statz, P. Newman, I. Smith, R. Pucel, and H. Haus, "GaAs FET device and circuit simulation in SPICE," *IEEE Trans. Electron Devices*, vol. ED-34, pp. 160 – 169, February 1987.

[7] W. Curtice, "A MESFET model for use in the design of GaAs integrated circuits," *IEEE Trans. Microwave Theory Tech*., vol MTT-28, pp. 446 – 446, May 1980.

[8] P.C. Canfield, "Modeling of Frequency and Temperature Effects in GaAs MESFETs" IEEE Journel of Solid-State Circuits, Vol. 25, pp. 299-306, Feb. 1990.

[9] M. Golio, M. Miller, G. Maracus, D. Johnson, "Frequency Dependent Electrical Characterisitics of GaAs MESFETs," IEEE Trans. Elec. Dev., vol. ED-37, pp. 1217-1227, May 1990.

[10] Agilent Technologies 395 Page Mill Rd. P.O. Box #10395 Palo Alto, CA 94303. ATN NP5.

[11] Maury Microwave Corporation, 2900 Inland Empire Blvd., Ontario, Ca., 91764.

[12] Michael Golio, Ed. *The RF and Microwave Handbook.* Boca Raton, FL: CRC Press, 2001.

[13] J. Michael Golio, Ed. *Microwave MESFETs and HEMTs.* Norwood, MA: Artech House, 1991.

[14] C. Whelan et al," Metamorphic Transistor Technology for RF Applications", *Microwave Journal*, April 2001.

[15] Textract, USF C+ developed program for linearization of several data points.

[16] SPECIAL, Gateway Modeling, Inc. 1604 East River Terrace, Minneapolis, MN 55414.

[17] Liechti, Charles A., "Microwave Field-Effect Transistors-1976," *IEEE Trans. Microwave Theory Tech*., vol. MTT-24, pp. 279 – 300, June 1976.

[18] E. Arnold, M. Golio, M. Miller, and B. Beckwith, "Direct extraction of GaAs MESFET intrinsic element and parasitic inductance values," *IEEE Microwave Theory Tech. Symp. Digest*, pp. 359 – 362, May 1990.

[19] M. Berroth and R. Bosch, "High-frequency equivalent circuit of GaAs FET's for large-signal applications," *IEEE Trans. Microwave Theory Tech*., vol. 39, pp. 224 – 229, February 1991.

[20] G. Dambrine, A. Cappy, F. Heliodore, and E. Playez, "A new method for determining FET small-signal equivalent circuits," *IEEE Trans. Microwave Theory Tech*., vol. 36, pp 1151 – 1159, July 1988.

[21] H. Rothe and W. Dahlke, "Theory of Noisy Fourpoles," *Proc. IRE*, vol 44, pp. 811 – 818, June 1956.

[22] Pospieszalski, Marian W. "Modeling of Noise Parameters of MESFET's and MODFETS's and Their Frequency and Temperature Dependance," *IEEE Transactions Microwave Theory Tech.*, vol MTT-37, pp. 1340 – 1350, September 1989.

[23] A.Van der Ziel, "Thermal Noise in Field-effect Transistors," *Proc. IRE*, vol 50, pp. 1808 – 1812, August 1962.

[24] Ikalainen, Pertti K "Extraction of Device Noise Sources form Measured Data Using Circuit Simulator Software," *IEEE Transactions Microwave Theory Tech.*, vol MTT-41, pp. 340 – 343 , February 1993.

[25] IC-CAP High-Frequency Model Tutorials, Volume 2. IC-CAP Release 5.0, June 1997.

[26] W. Curtice and M. Ettenberg, "A non-linear GaAs FET model for use in the design of output circuits for power amplifiers," *IEEE Transactions Microwave Theory Tech.*, vol MTT-33, pp. 1383 – 1394 1394, December 1985.

[27] O. Grinbergs, "*A Nonlinear Model of a Multi-FET Integrated Circuit*", Master Thesis, University of South Florida, 2000.

[28] J. Carlavilla, "*Modeling a Microwave pHEMT Using the Curtice Cubic Large-Signal MESFET Model*" Master Thesis, University of South Florida, 1999.

[29] S. M. Sze, *Physics of Semiconductor Devices 2nd Edition*, New York: John Wiley and Sons, 1981.

[30] A. Materka, T. Kacprzak "Computer calculation of Large-Signal GaAs FET Amplifier Characteristics," *IEEE Trans. Microwave Theory Tech*., vol MTT-33, pp. 129 – 135, February 1985.

[31] I. Angelov, H. Zerath, N. Rorsman "A New Empirical Nonlinear Model for HEMT and MESFET Devices," *IEEE Trans. Microwave Theory Tech*., vol MTT-40, pp. 2258 – 2266, December 1992.

[32] S. Maas, and D. Neilson "Modeling of MESFET's for Intermodulation Analysis of Mixers and Amplifiers," *1990 IEEE MTT-S. Microwave Symp. Dig*., pp. 1291 – 1294.

[33] IC-CAP Reference. IC-CAP Release 5.0, June 1997.

[34] MULTICAL, National Institute of Standards and Technology, 100 Bureau Drive Gaithersburg, MD., 20899.

[35] G. Gonzalez, *Microwave Transistor Amplifiers: Analysis and Design*. Prentice Hall, Aug. 1996.

[36] L. Yang, S. Long, "New Method to Measure the Source and Drain Resistance of the GaAs MESFET," *IEEE Electron Devices Letters*, vol. EDL-7, February 1986.

[37] Conversation with Steve Lardizabal at Raytheon RF Components.

[38] HP 8970B, HP 8971B, HP8971C Operating manual, Hewlett Packard Company, 1987.

[39] M. Pospieszalski, "On the Measurement of Noise Parameters of Microwave Two-ports," *IEEE Trans. on Microwave Theory and Tech.*, pp 456-458, April 1986.

[40] B. Hughes, "A Linear Dependence of Fmin on Frequency for FET's," *IEEE Trans. on Microwave Theory and Tech.*, pp 979-982, June/July 1993.

[41] M. W. Pospieszalski, J. D.Gallego, and W. J. Lakatosh, "Broadband, Low-Noise, Cryogenically-Coolable Amplifiers in 1 to 40 GHz Range," 1990 *IEEE MTT-S Digest,* pp 1253-1256.

[42] M. Schlechtweg, W. Reinert, et al., "Design and Characterization of High Performance 60 GHz Psuedomorphic MODFET LNAs in CPW-Technology Based on Accurate S-parameter and Noise Models," *IEEE Trans. on Microwave Theory and Tech* .pp 2445-2451, December 1992.

[43] P. J. Tasker, W. Reinert, et. al., "Direct Extraction of All Four Transistor Noise Parameters from a Single Noise Figure Measurement," *Proc. 22nd Eur. Microwave Conf*., pp 157 - 162, August 1992.

[44] M. Garcia, J. Stenarson, K. Yhland, H. Zirath, and I. Angelov "A New Extraction Method for the Two-Parameter FET Temperature Noise Model," *IEEE Trans. on Microwave Theory and Tech*., pp1679-1685, November 1998.

[45] M. Pospieszalski, A.C. Niedzwiecki "FET Noise Model and On-wafer Measurement of Noise Parameters," 1991 *IEEE MTT-S Digest*, pp 1117-1120.

[46] A.Van der Ziel, "Gate Noise in Field-effect Transistors at Moderatly High Frequencies," *Proc. IEEE*, vol 51, pp. 461 – 467, March 1963.

[47] J. Staudinger, "Modeling GaAs MESFETs for RF power amplifiers," *Microwave Journal*, pp. 20 – 34, December 1995.

[48] K. Rousseau, "Equations provide accurate GaAs MESFET modeling," *Microwaves & RF*, pp. 94 – 102, November 1991.

[49] M. Sango, O. Pitzalis, L. Lerner, C. McGuire, P. Wang, and W. Childs, "A GaAs MESFET large-signal model for non-linear analysis," *1988 IEEE MTT-S Int. Microwave Symp. Dig*., pp. 1053 – 1056, May 1988.

[50] M. Golio, "Characterization, parameter extraction and modeling for high frequency applications," *European Microwave Conference 1993*, vol. 23, pp. 69 – 72, September 1993.

[51] H. Willing, C. Rauscher, and P. DeSantis, "A technique for predicting large-signal performance of a GaAs MESFET," *IEEE Trans. Microwave Theory Tech*., vol MTT-26, pp. 1017 – 1023, December 1978.

[52] A. Patterson, V. Fusco, J. McKeown, and J. Stewart, "A systematic optimization strategy for microwave device modeling," *IEEE Trans. Microwave Theory Tech*., vol. 41, pp. 395 – 405, March 1993.

[53] S.H. Wemple, M.L. Steinberger, and W.O. Schlosser, "Relationship between power added efficiency and gate-drain avalanche in GaAs MESFETs," *Electron. Lett.*, vol. 16, pp. 459 – 460, June 5, 1980.

[54] S.H. Wemple, W.C. Niehaus, H.M. Cox, J.V. DiLorenzo, and W.O. Schlosser, "Control of gate-drain avalanche in GaAs MESFET's," *IEEE Trans. Electron Devices*, vol. ED-27, pp. 1013 – 1018, June 1980.

[55] F. Diamand and M. Laviron, "Measurement of extrinsic series elements of a microwave MESFET under zero current conditions," in *Proc. 12th European Microwave Conf*., (Finland), pp. 451 – 465, September 1982.

[56] G. Leuzzi, K. Deiseroth, and F. Giannini, "An improved method of parasitic extraction for non-linear modeling of microwave power MESFETs," *Proc. 22nd European Microwave Conf*, pp. 1206 – 1210, August 1992.

[57] R. Anholt and S. Swirhun, “Equivalent-circuit parameter extraction for cold GaAs MESFET’s,” *IEEE Trans. Microwave Theory Trans*., vol. 39, pp. 1243 – 1247, July 1991.

[58] J. Costa, M. Miller, M. Golio, and G. Norris, “Fast, accurate, on-wafer extraction of parasitic resistances and inductances in GaAs MESFETs and HEMTs,” in *1992 MTT-S Int. Symposium Digest*, June 1992, pp. 1011 – 1014.

[59] R. Tayrani, J. Gerber, T. Daniel, R. Pengelly, and U. Rohde, “Reliably extract MESFET and HEMT parameters,” *Microwaves & RF*, pp. 131 – 135, June 1993.

[60] H. Fukui, “Determination of the basic device parameters of a GaAs MESFET,” *Bell System Technical Journal*, vol. 58, no. 3, pp. 771 – 797, March 1979.

[61] E. Heaney, T. O’Connell, and P. Murphy, “Efficient MESFET modeling in a MMIC environment,” *Microwave Journal*, pp. 81 – 88, April 1992.

[62] W. Curtice and R. Camisa, “Self-consistent GaAs FET models,” *IEEE Trans. Microwave Theory Tech*., vol. MTT-32, pp. 1573 – 1578, December 1984.

APPENDICES

APPENDIX A: PLOTS OF THE NOISE MODEL FITTING

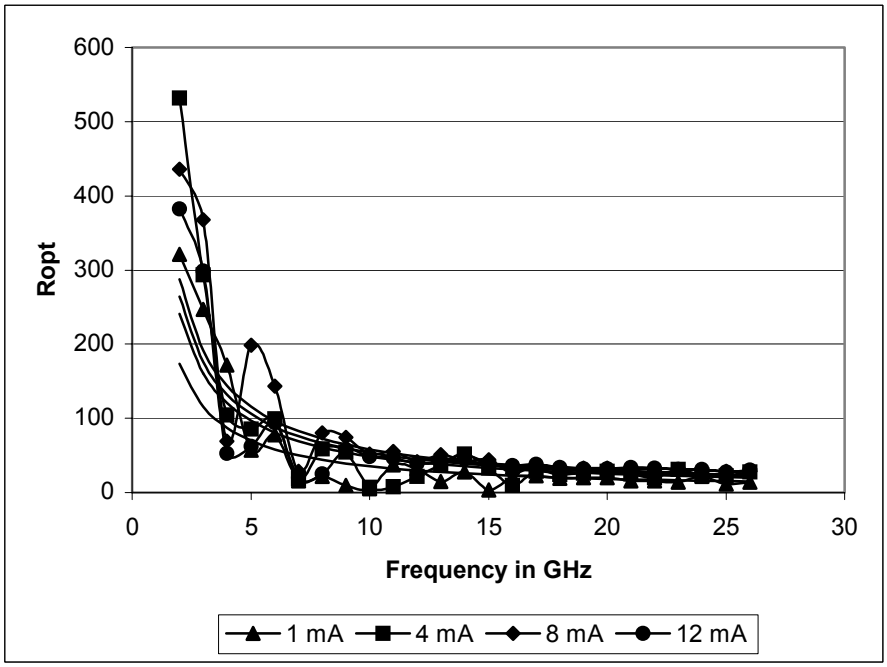

Figure A.1 Ropt at .5 volts Vd at a Temperature of 25C.

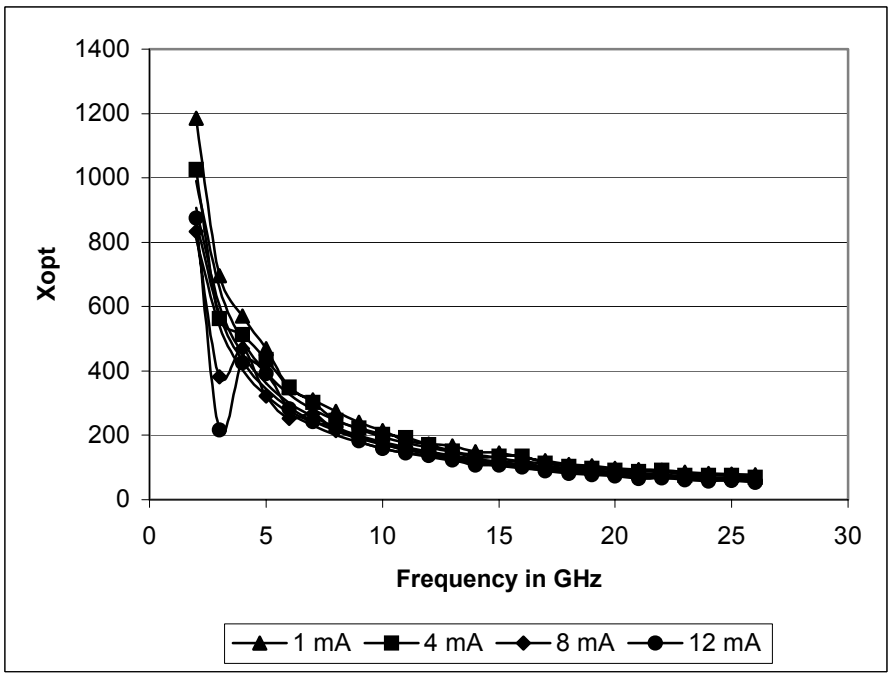

Figure A.2 Xopt at .5 volts Vd at a Temperature of 25C.

APPENDIX A: (Continued).

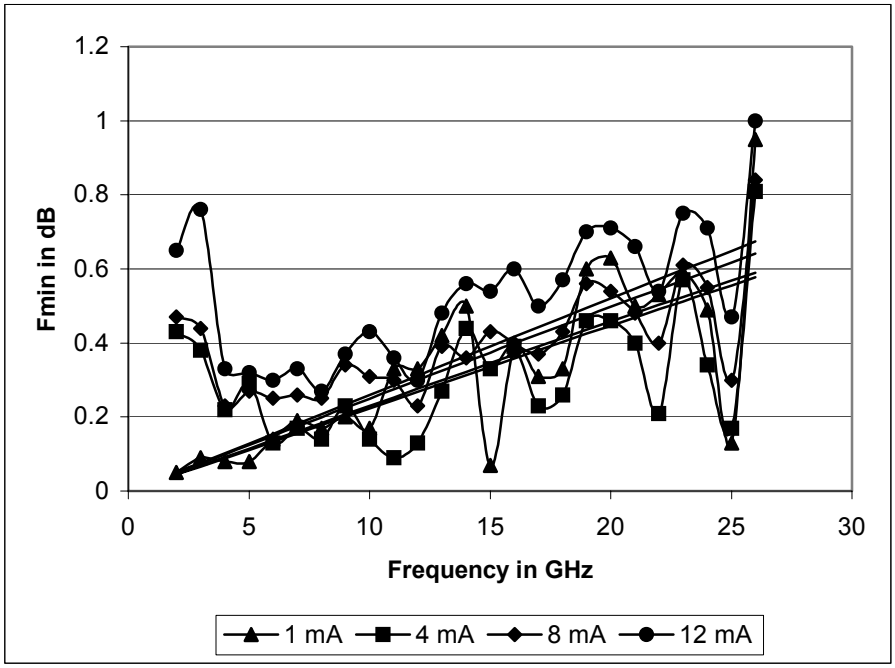

Figure A.3 Fmin at .5 volts Vd at a Temperature of 25C.

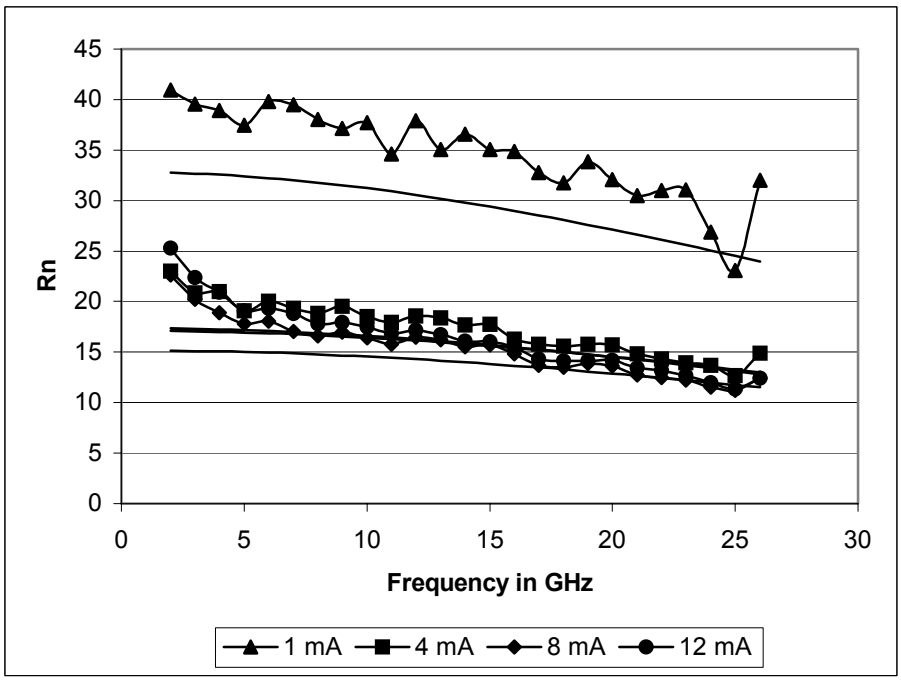

Figure A.4 Rn at .5 volts Vd at a Temperature of 25C.

APPENDIX A: (Continued).

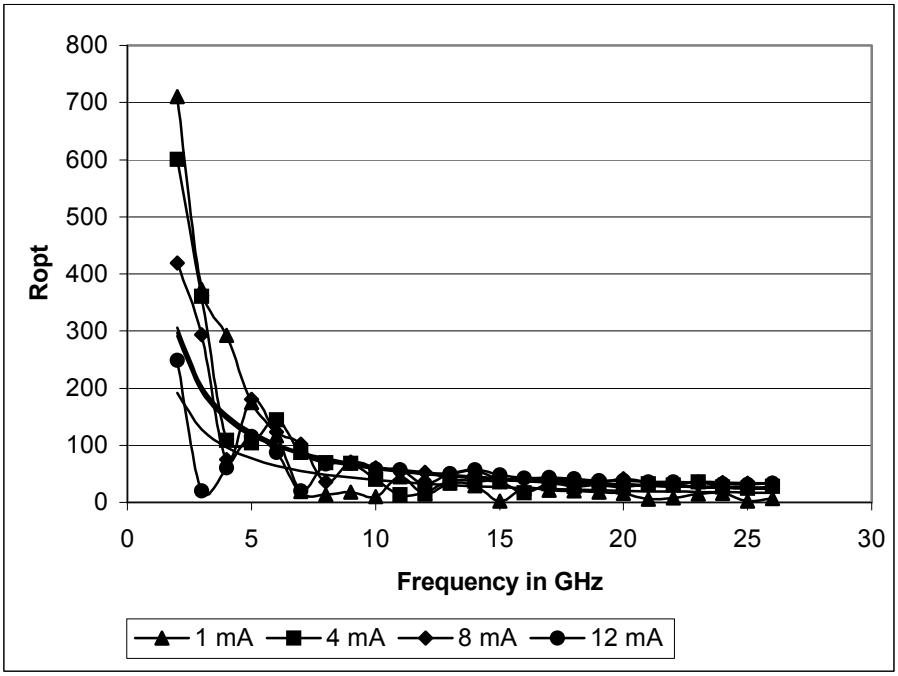

Figure A.5 Ropt at .75 volts Vd at a Temperature of 25C.

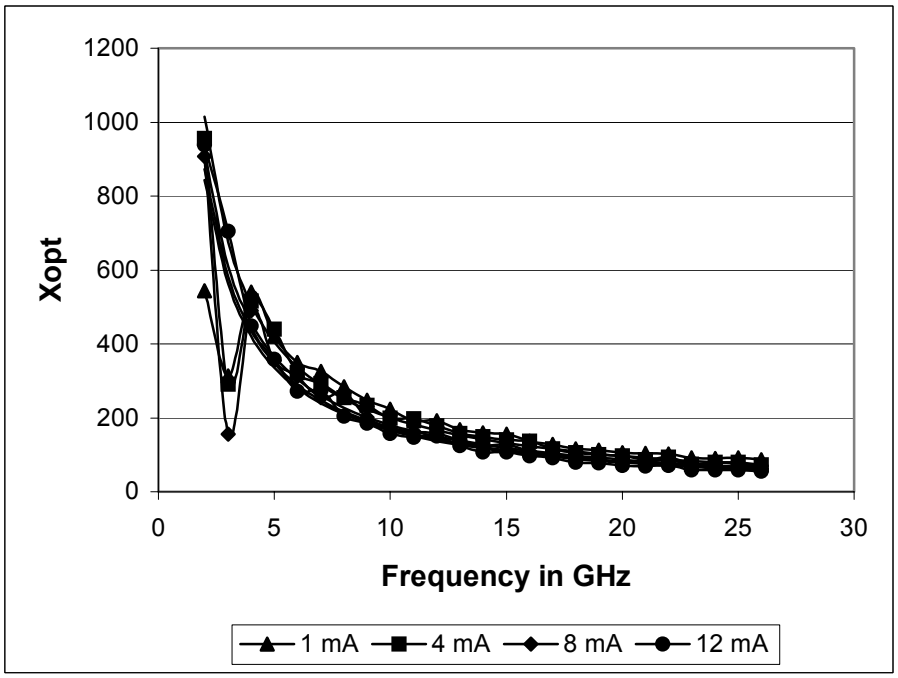

Figure A.6 Xopt at .75 volts Vd at a Temperature of 25C.

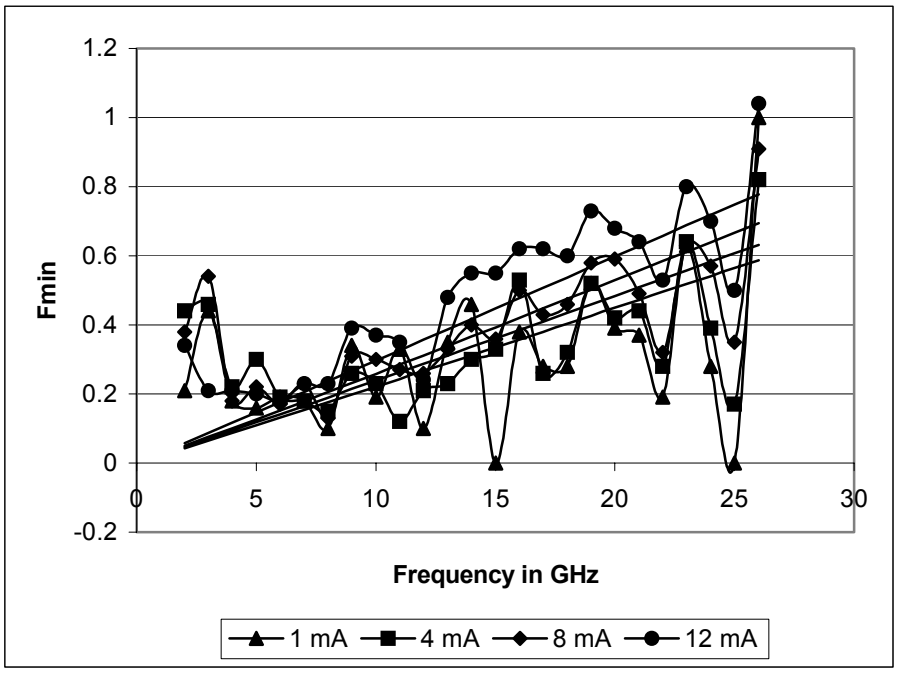

Figure A.7 Fmin at .75 volts Vd at a Temperature of 25C.

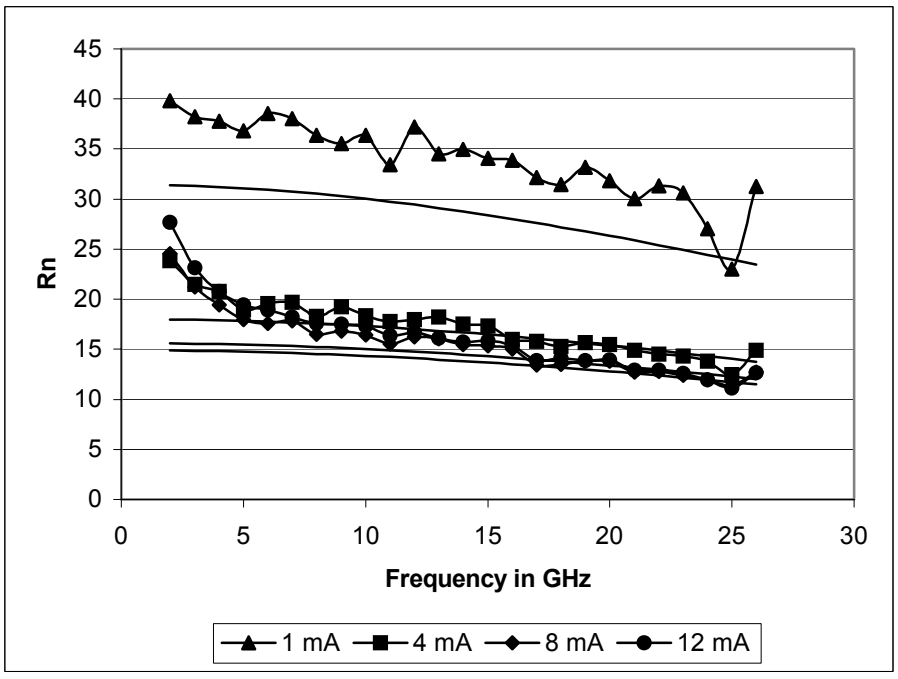

Figure A.8 Rn at .75 volts Vd at a Temperature of 25C.

APPENDIX A: (Continued).

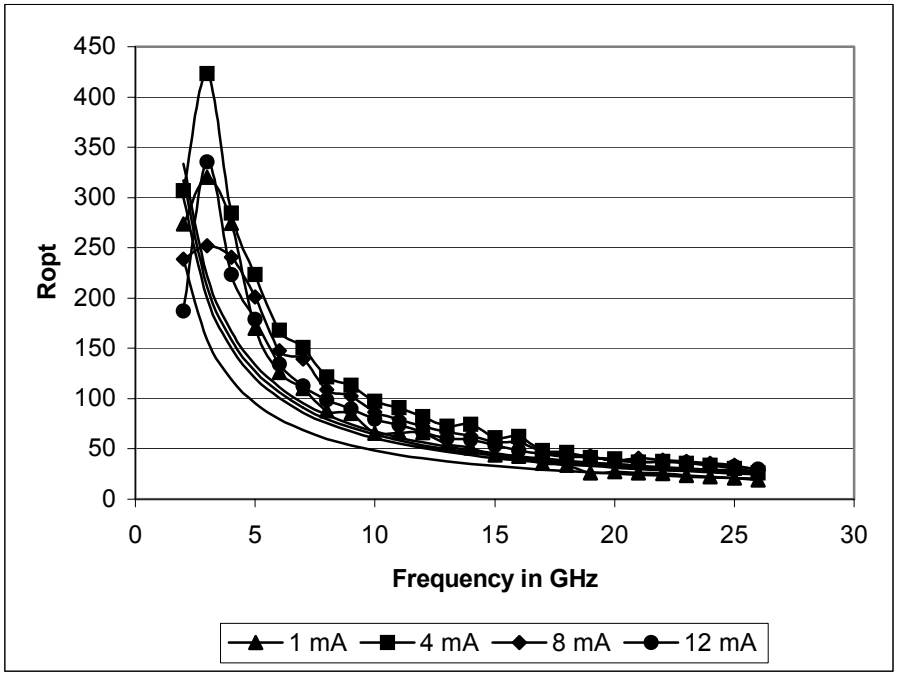

Figure A.9 Ropt at .5 volts Vd at a Temperature of 85C.

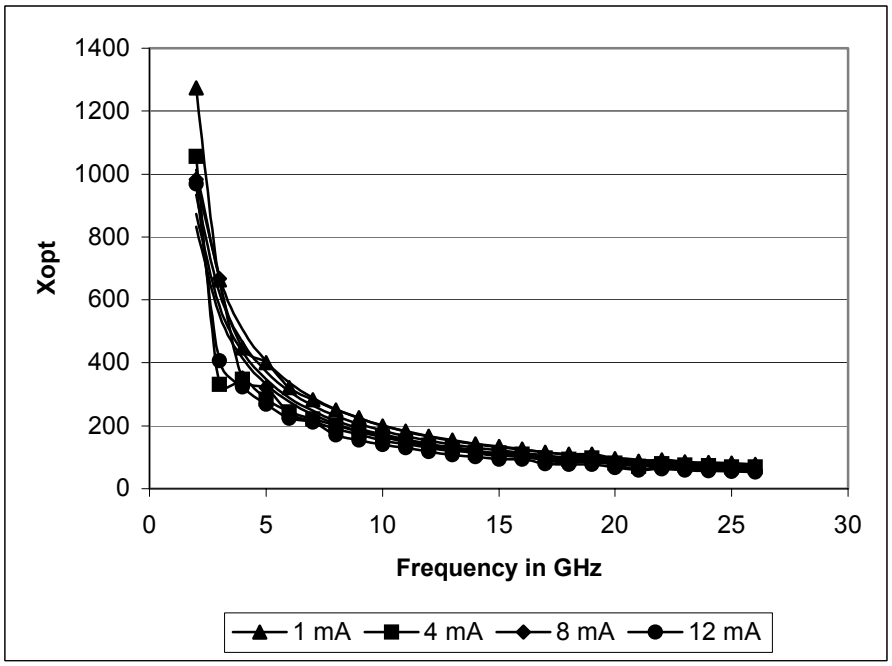

Figure A.10 Xopt at .5 volts Vd at a Temperature of 85C.

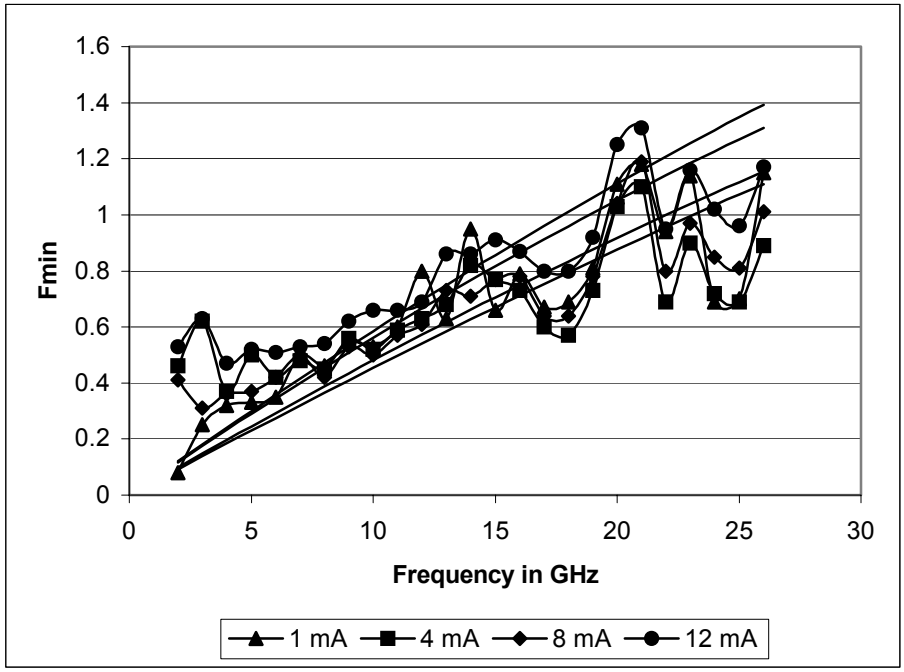

Figure A.11 Fmin at .5 volts Vd at a Temperature of 85C.

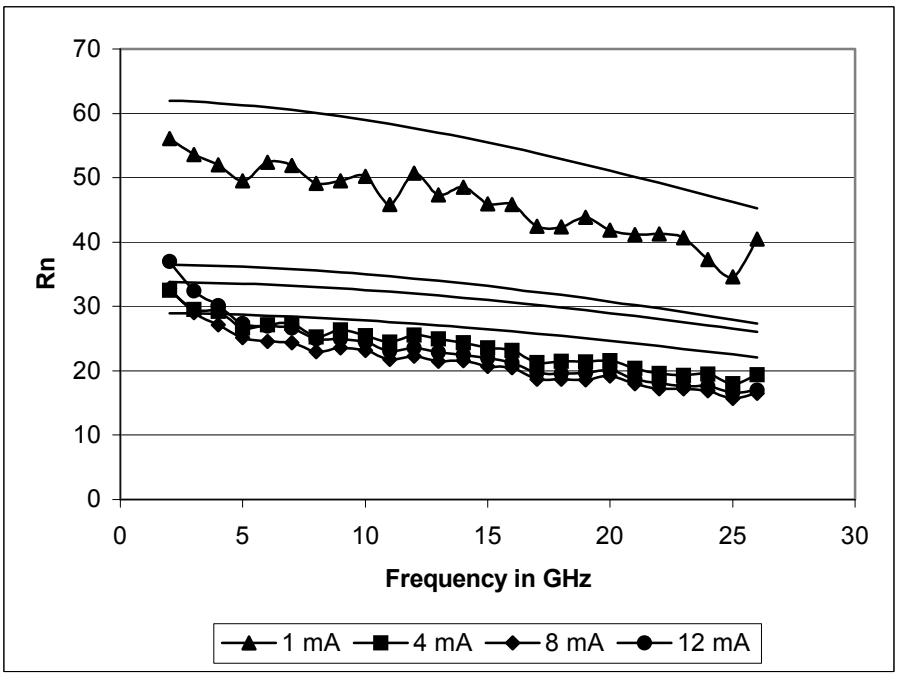

Figure A.12 Rn at .5 volts Vd at a Temperature of 85C.

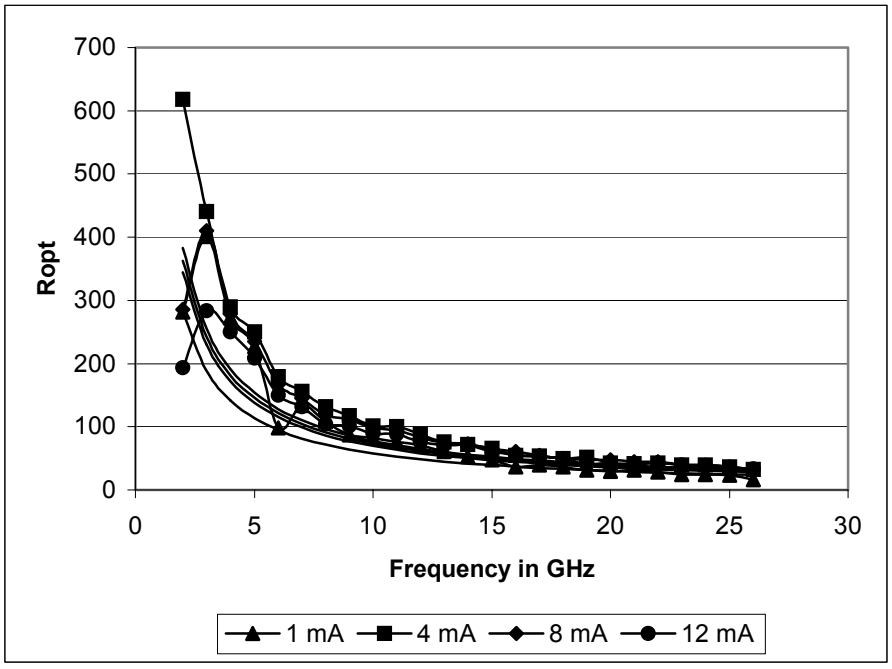

Figure A.13 Ropt at .75 volts Vd at a Temperature of 85C.

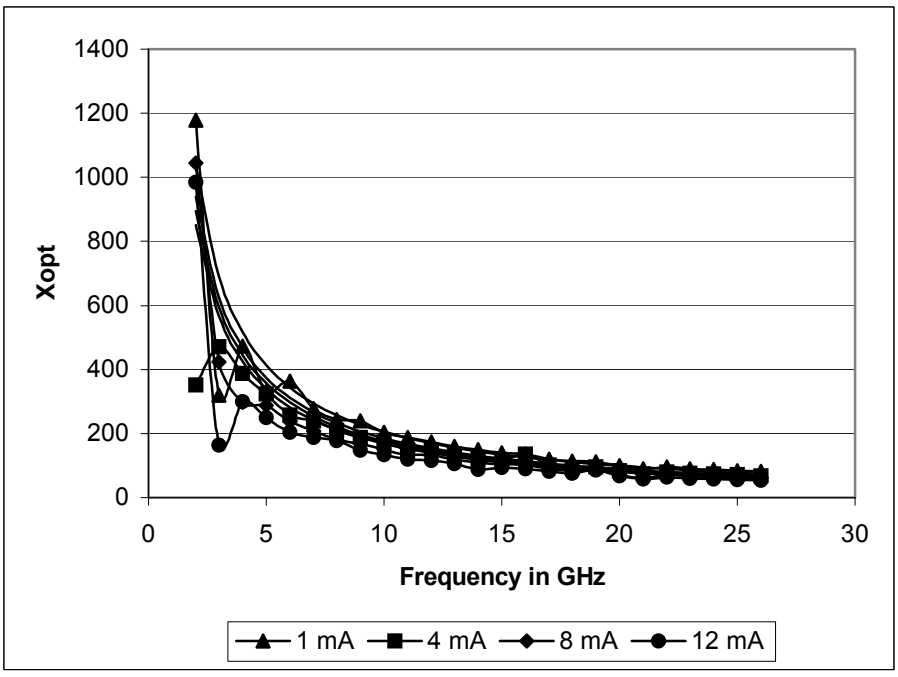

Figure A.14 Xopt at .75 volts Vd at a Temperature of 85C.

APPENDIX A: (Continued).

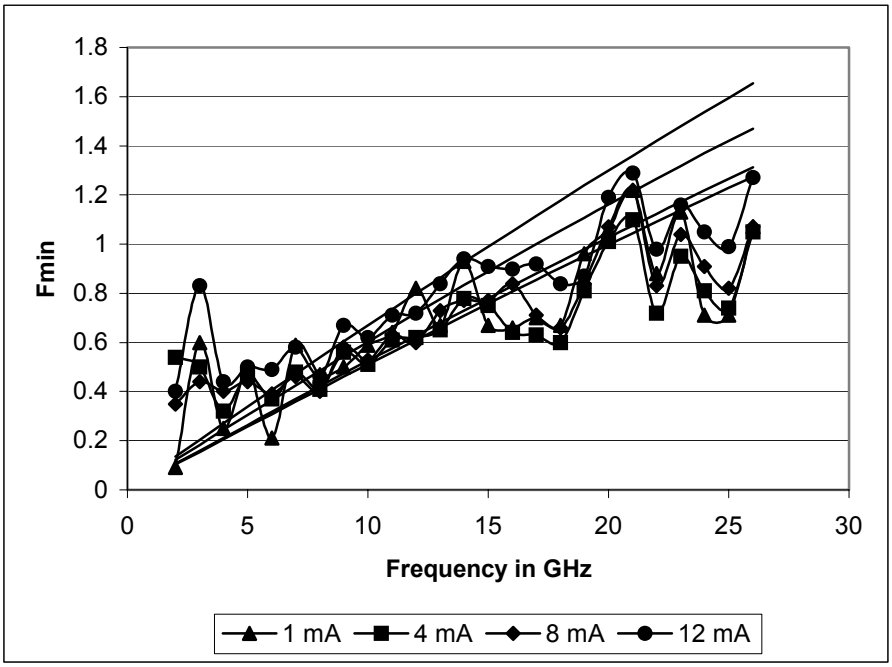

Figure A.15 Fmin at .75 volts Vd at a Temperature of 85C.

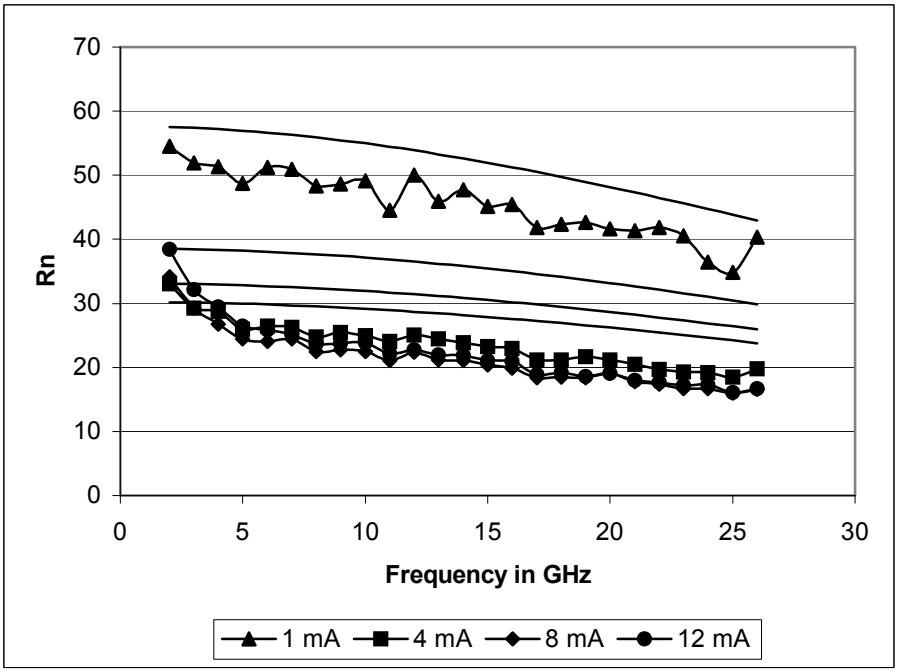

Figure A.16 Rn at .75 volts Vd at a Temperature of 85C.

APPENDIX B: GM AND GDS EQUATIONS FOR THE EEHEMT MODEL

Table B.1 Agilent HEMT Model Drain-Source Current Parameters [26].

Parameter	Description
V_{to}	Zero-bias threshold
γ	Vds-dependent threshold parameter
V_{go}	Gate-source voltage where gm is maximum
V_{delt}	Controls linearization point for gm characteristic
V_{ch}	Gate-source voltage where gamma no longer effects the IV curve.
gm_{max}	Peak transconductance
V_{dso}	Drain voltage where Vds dependency disappears from equations.
V_{sat}	Ids saturation parameter
κ	Output conductance
P_{eff}	Channel-to-backside self-heating for DC.
V_{tso}	Subthreshold onset voltage

For $V_{gs} \geq V_g$

$$gm = gm_{\max}\left\{1+\gamma\left(V_{dso}-V_{ds}\right)\right\}$$

$$g_{ds} = -gm_{\max}\gamma\left(V_{gs}-V_{ch}\right)$$

For $V_{gs} \leq V_t$

$$gm = 0$$

$$g_{ds} = 0$$

For all other conditions

$$gm = \frac{gm_{\max}}{2}\left[1+\gamma\left(V_{dso}-V_{ds}\right)\right]\left\{\cos\left[\pi\frac{V_x-\left(V_{go}-V_{ch}\right)}{V_{to}-V_{go}}\right]+1\right\}$$

$$g_{ds} = -\frac{gm_{\max}}{2}\gamma\left(V_{dso}-V_{ds}\right)\left\{\cos\left[\pi\frac{V_x-\left(V_{go}-V_{ch}\right)}{V_{to}-V_{go}}\right]+1\right\}$$

$$V_x = \left(V_{gs}-V_{ch}\right)\left(1+\gamma\left(V_{dso}-V_{ds}\right)\right)$$

APPENDIX B: (Continued).

Table B.2 Agilent HEMT Model Drain-Source Current Parameters [26].

V_{co}	Voltage where gm compression begins.
μ	Adds Vds dependence to gm compression onset.
V_{BA}	Gm compression "tail-off".
V_{BC}	Gm roll-off to tail-off transition voltage.
Δgm	Slope of gm compression.
α	Gm saturation to compression transition.

$$V_c = V_{co} + \mu\left(V_{dso} - V_{ds}\right)$$

$$V_b = V_{bc} + V_{co} + \mu\left(V_{dso} - V_{ds}\right)$$

$$V_a = \left(V_{bc} - V_{ba}\right) + V_{co} + \mu\left(V_{dso} - V_{ds}\right)$$

For $V_{gs} \le V_b$

$$gm^{comp} = gm - gm_v$$

$$gm_v = \Delta gm\left[Vy - \alpha\right]$$

$$g_{ds}{}^{comp} = g_{ds} - g_{dsv}$$

$$g_{dsv} = \Delta gm\mu\left(\frac{1}{2}\left(\frac{2\left(V_{gs} - V_c\right)^2 + \alpha}{Vy} + \frac{\alpha^2}{\left(V_{gs} - V_c\right) + Vy}\left[1 + \frac{\left(V_{gs} - V_c\right)}{Vy}\right]\right) - \alpha\right)$$

$$Vy = \sqrt{\alpha^2 + \left(V_{gs} - V_c\right)^2}$$

For $V_{gs} \ge V_b$

$$gm^{comp} = gm - \left[a\left(V_{gs} - V_a\right)^b + g_{mo}\right]$$

$$g_{ds}{}^{comp} = g_{ds} - \mu\left[a\left(V_{gs} - V_a\right)^b + g_{mo}\right] - g_{dsv}$$

$$a = \frac{\Delta gm\left[\sqrt{\alpha^2 + \left(V_b - V_c\right)^2} - \alpha\right] - g_{mo}}{V_{BA}{}^b}$$

APPENDIX B: (Continued).

$$b = \frac{S_{vb} \square V_{BA}}{\Delta gm\left[\sqrt{\alpha^2 + \left(V_b - V_c\right)^2} - \alpha\right] - g_{mo}}$$

$$S_{vb} = \Delta gm \frac{V_{BC}}{\left(\sqrt{\alpha^2 + {V_{BC}}^2}\right)}$$

The preceding formulas for compressed *gm* and *gds* can now be entered into a format that is the standard Curtice nonlinear model equation [].

$$gm = gm^{comp}\left(1 + \lambda V_{ds}\right)\tanh\left(\frac{3V_{ds}}{V_{sat}}\right)$$

$$g_{ds} = \left\{{g_{ds}}^{comp}\left(1 + \lambda V_{ds}\right) + {g_{ds}}^{comp}\lambda\right\}\tanh\left(\frac{3V_{ds}}{V_{sat}}\right) + {I_{ds}}^{comp}\frac{3\left(1 + \lambda V_{ds}\right)}{V_{sat}}\sec h^2\left(\frac{3V_{ds}}{V_{sat}}\right)$$

APPENDIX C: TABLE MODEL (DCSR FILE) AT ROOM TEMPERATURE

BEGIN DSCRDATA

%	gm	Cgs	Cgd	Cds	Rds	T	Ri	Tg	Td
0	18	52.3	24.3	27.9	860	0.376	6.34	76.4	2475
1	28.7	57	24.4	28.3	524	0.281	7.23	71.8	2337
2	36.1	59.7	24.5	28.6	412	0.262	6.74	90.2	2212
3	41.6	61.6	24.6	28.8	351	0.218	7.06	95	2518
4	45.8	63	24.5	27.9	315	0.19	6.74	99	2383
5	49.3	64.1	24.6	28.3	286	0.169	6.92	104	2675
6	52.1	65.4	24.7	28.6	264	0.178	6.59	109	2385
7	54.4	66.7	24.9	29	245	0.168	6.63	112.6	2539
8	56.2	67.4	25.1	29	228	0.143	6.84	106.8	2652
9	57.7	68.7	25.4	29.3	212	0.133	6.79	113.8	2642
10	58.8	69.5	25.8	29.7	196	0.128	6.89	84.7	2660
11	59.5	70.6	26.3	30	181	0.131	6.7	100.7	2700
12	18.4	53.3	21.4	28.9	1155	0.37	8.85	58.1	3309
13	28.8	58.8	21	29.5	751	0.278	8.77	84.4	3003
14	36	62.5	20.8	29.8	609	0.228	8.6	70.7	3133
15	41.6	64.7	20.6	30.3	534	0.201	8.62	74	3460
16	46	66.3	20.5	30.9	488	0.186	8.51	66.7	3494
17	49.5	67.9	20.5	31.1	454	0.183	8.22	78.5	3644
18	52.5	69	20.4	31.4	429	0.175	8.03	84.9	3957
19	55	69.9	20.4	31.8	409	0.165	8.07	89	4281
20	57.3	70.7	20.3	30.9	401	0.143	7.79	99	4534
21	59.1	71.5	20.3	31.1	386	0.146	7.5	97.6	4914
22	60.7	72.2	20.4	31.8	372	0.159	7.52	111.3	5413
23	62	73	20.5	31.7	356	0.141	7.46	119	5734
24	14.8	58.7	22.5	48.4	1200	0.461	7.66	119.4	1835
25	25.7	64.8	21.8	48.7	735	0.392	6.24	123.6	2966
26	33.4	68	21.3	49.1	596	0.381	5.34	110.6	3017
27	39.2	69.9	21	49.2	525	0.38	4.62	107.2	3173
28	43.9	71.4	20.9	49.4	484	0.387	4.09	200.4	3652
29	47.8	72.5	20.7	49.5	456	0.405	3.57	203.7	4035
30	51.1	73.4	20.6	49.3	434	0.399	3.32	230	4352
31	53.8	74	20.5	49.4	419	0.412	2.94	269.7	4818
32	56.2	74.7	20.4	49.2	405	0.405	2.79	257.4	5195
33	58.3	75.3	20.4	49.3	396	0.403	2.67	363.7	5822
34	60.1	75.7	20.3	49.3	386	0.396	2.66	312	6283
35	61.7	76.1	20.3	49.4	378	0.403	2.4	312	6585
36	14.3	54.8	22	48.2	1280	0.53	9.47	136	3359
37	24.9	61.8	21.4	48.2	778	0.403	8.18	88.5	3152
38	32.6	65.3	20.9	48.1	623	0.346	7.56	97	3249
39	38.4	67.3	20.6	48	552	0.34	6.72	82.4	3431
40	43.1	68.9	20.4	47.5	507	0.309	6.56	126.6	3924
41	46.9	69.8	20.2	47.3	480	0.312	6.08	160.3	4396
42	50.2	70.6	20	46.8	460	0.296	6.03	219.7	5259
43	52.9	71.2	19.9	46.5	446	0.277	6.1	189.6	5661
44	55.3	71.7	19.8	46.2	435	0.278	5.75	268.6	6579
45	57.4	72.1	19.8	45.9	426	0.257	5.9	228.6	7452
46	59.2	72.6	19.7	45.6	419	0.242	5.88	259.9	8538
47	60.7	72.9	19.7	45.3	413	0.239	5.54	258.2	9629

END DSCRDATA

APPENDIX D: NOISE EXTRACTION IN ADS

Eqn gm=.0538

Eqn Rds=270

Eqn Ri=2.94

Eqn Cgs=64.1

Eqn To=25

Eqn Zop=50*((1+Sopt)/(1-Sopt))

Eqn Qp=(NFmin/10)

Eqn Yop=1/Zop

Eqn N=pow(10,Qp)

Eqn Gop=real(Yop)

Eqn k=(4*real(Yop)*Rn)/(N-1)

Eqn yc=((N-1)/(2*Rn))-Yop

Eqn gn=(N-1)*(Gop-(N-1)/(4*Rn))

Eqn d=pow(2*3.1415*freq*Cgs*1E-15,2)

Eqn dd=1+(d*Ri*Ri)

Eqn y11d=Y(1,1)

Eqn y11dd=((d*Ri)/dd)+((sqrt(d))/dd)*j

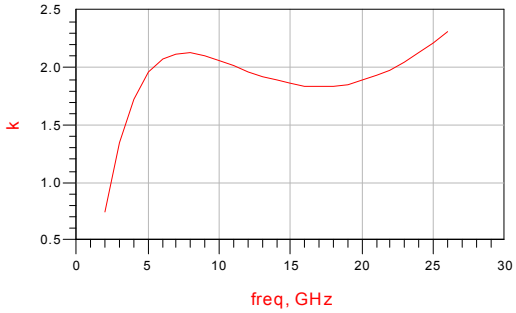

Eqn y21d=Y(2,1)

Eqn y21dd=(gm/dd)+((sqrt(d)*Ri*gm)/dd)*j

Eqn R=gm*(gn+Rn*sqr(mag(y11d-yc)))/sqr(mag(y11d))

Eqn r=gm*(gn+Rn*sqr(mag(y11dd-yc)))/sqr(mag(y11dd))

Eqn P=(1/gm)*(sqr(mag(y21d/y11d))*(gn+(Rn*sqr(mag(yc)))))

Eqn p=(1/gm)*(sqr(mag(y21dd/y11dd))*(gn+(Rn*sqr(mag(yc)))))

Eqn tg=r*(To+273.15)/(gm*Ri)

Eqn Tg=R*(To+273.15)/(gm*Ri)

Eqn td=p*(To+273.15)*(gm*Rds)

Eqn Td=P*(To+273.15)*(gm*Rds)

APPENDIX D: (Continued).

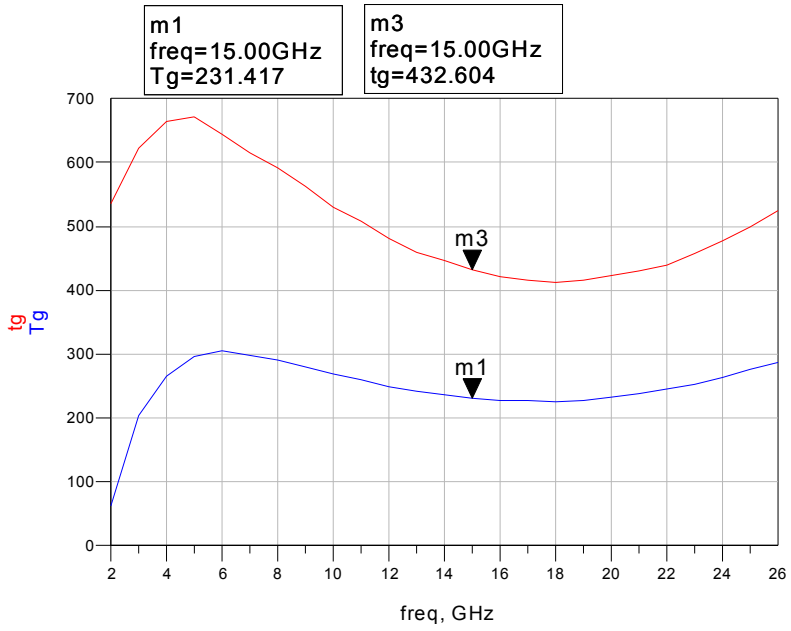

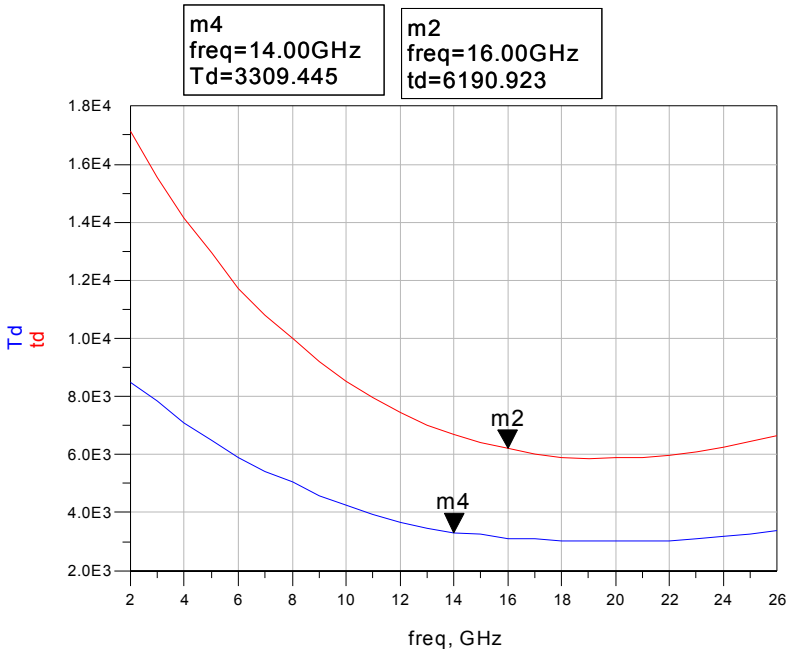

APPENDIX E: EEHEMT MODEL PARAMETERS

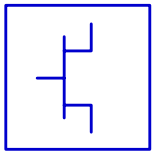

EE_HEMT1_Model
EEHEMTM3

Vto=-800.0 mV	Tau=780.2 fsec	C11th= 39.53f	Ngf=6.000	Vinfltc=
Gamma=37.18m	Cdso=24.06 fF	Vinfl=-608.4m	Vco=-371.2 mV	Vtoactc=
Vgo=-316.0 mV	Rdb= 1.000G	Deltgs= 1.600	Vba= 1.000	Gmmaxactc=
Vdelt= 0.000	Cbs= 160.0f	Deltds= 360.5m	Vbc= 400.0m	Gammaactc=
Vch= 935.0m	Vtoac=-844.9m	Lambda= 20.00m	Mu= 333.3u	Xti=
Gmmax=66.50 mH	Gammaac=33.28m	C12sat= 20.44f	Deltgm=783.5m	wVgfwd=
Vdso=.500 V	Vdeltac= 0.000	Cgdsat= 15.26f	Deltgmac=746.7m	wBvgs=
Vsat=335.3 mV	Gmmaxac=68.66m	Kbk= 30.00m	Alpha=10.0 mV	wBvgd=
Kapa=176.9 mS	Kapaac= 50.65m	Vbr= 25.00	Tnom=	wBvds=
Peff=500.0m	Peffac= 75.75	Nbr= 2.000	Rgtc=	wIdsmax=
Vtso=-100.0	Vtsoac=-100.0	Idsoc= 1.893	Rdtc=	wPmax=
Is=1.338 nA	Gdbm= 50.00u	Rd= 200.0m	Rstc=	AllParams=
N=1.763	Kdb= 100.0	Rs= 200.0m	Vtotc=	
Ris=10.00 mOhm	Vdsm= 100.0	Rg= 100.0m	Gmmaxtc=	
Rid=1.000 mOhm	C11o= 126.6f	Ugw=12.5 um	Gammatc=	

Figure E.1 Developed EEHEMT Model Parameters for the 75um Raytheon mHEMT.

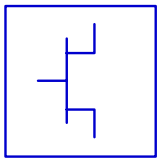

EE_HEMT1_Model
EEHEMTM6

Vto=-1.5	Tau=0	C11th=30 fF	Ngf=1	Vinfltc=
Gamma=.05	Cdso=80 fF	Vinfl=1	Vco=10	Vtoactc=
Vgo=0	Rdb=1 GOhm	Deltgs=.5	Vba=1	Gmmaxactc=
Vdelt=0	Cbs=160 fF	Deltds=1	Vbc=1	Gammaactc=
Vch=1	Vtoac=-1.5	Lambda=1	Mu=1	Xti=
Gmmax=70m	Gammaac=.05	C12sat=30 fF	Deltgm=0	wVgfwd=
Vdso=2	Vdeltac=0	Cgdsat=50 fF	Deltgmac=0	wBvgs=
Vsat=1	Gmmaxac=60m	Kbk=0	Alpha=1 mV	wBvgd=
Kapa=1	Kapaac=0	Vbr=15	Tnom=25	wBvds=
Peff=2	Peffac=10	Nbr=2	Rgtc=	wIdsmax=
Vtso=-10	Vtsoac=-10	Idsoc=100 mA	Rdtc=	wPmax=
Is=10 fA	Gdbm=0	Rd=1	Rstc=	AllParams=
N=1	Kdb=0	Rs=1	Vtotc=	
Ris=0	Vdsm=1	Rg=1	Gmmaxtc=	
Rid=0	C11o=300 fF	Ugw=0	Gammatc=	

Figure E.2 EEHEMT Model Default Parameter Values.

APPENDIX F: S2P FILE FORMAT

```
!MASK ID: LN110
!PROCESS: MHEMT          DEVICE:  LN110_06 6x12.5 PERIPHERY: 0.075mm
!LOT    : X99M90-3       CHIP  :  07-04          TEMP.(C) : ambient
!VD 1,1.25
!VD=  1.000 V  ID= 10.005mA  VG=  -.481 V  IG=   -3.780uA
!Rg =   .30Ohm   Rd =   .10Ohm   Rs =   .30Ohm   Ri  = 25.58Ohm
!Cgs =   .08pF    Cgd =   .02pF    Cds =   .04pF    Tau =   .39pSec
!Gm  = 59.87mS    Rds = 316.06Ohm   Rcgs=  10.00MOhm  Rcgd=  10.00MOhm
!Lg  =   .01pH    Ld  = 20.10pH    Ls  = 22.65pH    Ft  = 112.38GHz
!E11 =   2.67%     E12 =   6.22%     E21 =   1.24%     E22 =   3.50%
!Vg  =   -.48V     Ig  =  -3.78uA    Igs =  -3.79uA    Leff=   .07uM
!Vd  =   1.00V     Id  =  10.01mA    Ids =   9.99mA    Idss=   0.00mA
! GM/(2*PI*Cgs)=121.62 GHz  GM/(2*PI*(Cgs+Cgd))= 97.35 GHz
# GHZ S MA R 50
!Measurement Date: 21 Jun 2000     Time: 18:25:40
!    RAW S-PAR DATA
!           S11            S21           S12           S22
!Freq(GHz) Mag   Ang     Mag    Ang    Mag   Ang     Mag   Ang
  2.000   .9891  -10.43  5.0274  169.74  .0217  84.15  .7655  -8.14
  2.250   .9875  -11.77  5.0262  168.49  .0245  83.29  .7640  -9.32
  2.500   .9851  -13.04  4.9966  167.19  .0271  82.61  .7632  -10.51
....
....
 25.500   .5957  -92.22  2.6175  92.80  .1321  50.77  .4801  -72.11
 25.750   .5881  -92.58  2.5940  92.49  .1315  51.00  .4744  -72.23
 26.000   .5934  -93.09  2.5861  92.02  .1320  51.32  .4783  -72.87
!    RAW NOISE DATA
!FREQUENCY   FMIN   GAMMA OPT       Rn       Ga (Associated Gain)
! (Ghz)      (dB)  Mag   Ang   (NORMALIZED)       (dB)
  2.000      .35  .954    6.4   1.317    !      28.68
  4.000      .21  .988    12.9    .702    !      19.76
  5.000      .27  .901    15.7    .582    !      22.96
....
....
 24.000      .64  .616    70.3    .256    !      12.30
 24.500      .77  .622    72.0    .269    !      12.28
 25.000      .72  .633    74.5    .255    !      12.32
 26.000      .85  .607    76.4    .252    !      12.02
```

APPENDIX G: TEMPERATURE DEPENDENT MODEL

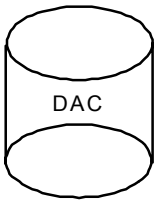


```
DataAccessComponent
ECP
File="temp_model.dscr"
Type=Discrete
InterpMode=Index Lookup
InterpDom=Rectangular
iVar1=1
iVal1=1-1
```

Var Eqn

```
VAR
VAR1
x=-55
Cgs=Cgsa+(Cgsb*y)
y=x-25
gm=gma+(gmb*y)
Cgd=Cgda+(Cgdb*y)
Cds=Cdsa+(Cdsb*y)
Rds=Rdsa+(Rdsb*y)
T=Ta+(Tb*y)
Ri=Ria+(Rib*y)
Tg=Tga+(Tgb*y)
Td=Tda+(Tdb*y)
```

Var Eqn

```
VAR
_VAR
gma=file{ECP,"gm"}
gmb=file{ECP,"gmx"}
Cgsb=file{ECP,"Cgsx"}
Cgsa=file{ECP,"Cgs"}
Cgda=file{ECP,"Cgd"}
Cgdb=file{ECP,"Cgdx"}
Cdsa=file{ECP,"Cds"}
Cdsb=file{ECP,"Cdsx"}
Rdsa=file{ECP,"Rds"}
Rdsb=file{ECP,"Rdsx"}
Ta=file{ECP,"T"}
Tb=file{ECP,"Tx"}
Ria=file{ECP,"Ri"}
Rib=file{ECP,"Rix"}
Tga=file{ECP,"Tg"}
Tgb=file{ECP,"Tgx"}
Tda=file{ECP,"Td"}
Tdb=file{ECP,"Tdx"}
```